

True-Amplitude Seismic Imaging Beneath Gas Clouds

True-Amplitude Seismic Imaging Beneath Gas Clouds

PROEFSCHRIFT

ter verkrijging van de graad van doctor
aan de Technische Universiteit Delft,
op gezag van de Rector Magnificus Prof.ir. K.C.A.M Luyben,
voorzitter van het College voor Promoties,
in het openbaar te verdedigen
op maandag 3 januari 2011 om 10:00 uur

door

Ahmad Riza GHAZALI

Bachelor of Science in Geophysics,
University of Leicester, United Kingdom
geboren te Penang, Maleisië

Dit proefschrift is goedgekeurd door de promotor:
Prof.dr.ir. A. Gisolf

Copromotor:
Dr.ir. D.J. Verschuur

Samenstelling promotiecommissie:

Rector Magnificus,	voorzitter
Prof.dr.ir. A. Gisolf,	Technische Universiteit Delft, promotor
Dr.ir. D.J. Verschuur,	Technische Universiteit Delft, copromotor
Prof.dr. H. Jakubowicz,	Imperial College London,
Prof.dr.ir. C.P.A Wapenaar,	Technische Universiteit Delft,
Prof.dr.ir. R.J. Arts,	Technische Universiteit Delft,
Dr. D.P. Ghosh,	PETRONAS Research (Maleisië),
Dr.ir. W.E.A. Rietveld,	BP Angola (UK),
Prof.dr.ir. P.M. van den Berg,	Technische Universiteit Delft, reservelid

ISBN 978-90-8570-711-0

Copyright ©2011, by A.R. Ghazali, Laboratory of Acoustical Imaging and Sound Control, Faculty of Applied Sciences, Delft University of Technology, Delft, The Netherlands.

All rights reserved. No part of this publication may be reproduced, stored in a retrieval system or transmitted in any form or by any means, electronic, mechanical, photocopying, recording or otherwise, without the prior written permission of the author A.R. Ghazali, Faculty of Applied Sciences, Delft University of Technology, P.O. Box 5046, 2600 GA, Delft, The Netherlands.

SUPPORT

The research for this thesis was financially supported by the Petroleum Nasional Berhad (PETRONAS) and DELPHI consortium.

Typesetting system: \LaTeX .

Printed in The Netherlands by Wöhrmann Print Service.

Dedicated to my love:
Cik Junidza Mat Nayan
& my beautiful family
and for my future genetics ...

Contents

1	Introduction	5
1.1	Wave physics: propagation through a gas cloud	5
1.2	Geology: uncertainties	8
1.3	Problem description: kinematics and dynamics	9
1.4	Current approaches to gas-cloud problems	12
1.4.1	Q-attenuation and compensation	13
1.4.2	Depth conversion	14
1.4.3	Tomography: Building an accurate velocity model	16
1.4.4	Multicomponent seismic methods	17
1.5	Limitations of current seismic imaging	19
1.6	Thesis objective	21
1.7	Thesis outline	22
2	Wavefield extrapolation in heterogeneous media	25
2.1	Wavefield extrapolation in homogeneous media	25
2.2	Seismic imaging in low-contrast inhomogeneous media	29
2.3	Seismic imaging in high-contrast heterogeneous media	31
2.3.1	Forward model	31
2.3.2	Backward extrapolation via a full-wavefield inversion	32
2.4	General representation of seismic data	33
2.4.1	Discrete matrix notation	33
2.4.2	WRW representation	33
3	Inversion strategy for gas clouds	37
3.1	Proposed inversion strategy	37
3.1.1	Forward model	37
3.1.2	Inversion strategy	41

3.1.3	Estimation of transmission operator \hat{W}_A and data application	41
3.1.4	1.5D Formulation	43
3.1.5	Energy-flux based approach	45
4	Nonlinear inversion for effective media	47
4.1	Genetic Algorithms	47
4.1.1	GA definitions	49
4.1.2	Initial parameters	50
4.1.3	Objective function	50
4.1.4	Mating	50
4.1.5	Mutation	51
4.1.6	Population crossover	51
4.2	1.5D implementation	52
4.2.1	1.5D Objective function	52
4.2.2	Frequency marching	53
4.3	2D implementation	54
4.3.1	Initial 2D GA parameter distribution	55
4.3.2	Adaptive objective function	55
4.3.3	Local objective function	57
4.3.4	Blended acquisition	59
4.3.5	Other enhancements	61
5	Synthetic data examples	63
5.1	Model description	63
5.2	1.5D Example	64
5.2.1	Deconvolution with true transmission operators	65
5.2.2	Nonlinear full-waveform inversion results	66
5.2.3	1.5D transmission deconvolution results	69
5.2.4	Statistical analysis of the inversion results	74
5.3	2D Example	77
5.3.1	2D transmission deconvolution using the correct model	77
5.3.2	2D nonlinear full-waveform inversion using a Genetic Algorithm	81
6	Application to field data	87
6.1	Geological background	88
6.2	Estimation of primaries by sparse inversion	90

6.3	Inversion strategy	92
6.4	Results	93
7	Discussions and recommendations	99
7.1	Discussions	99
7.1.1	Crosscorrelation versus deconvolution redatuming for high-contrast heterogeneous media	99
7.1.2	Layer-stripping redatuming	101
7.1.3	Land near-surface problem	102
7.2	Recommendations	102
7.2.1	3D implementation	102
7.2.2	Elastic solution	103
7.2.3	Anelastic solution - incorporating attenuation	103
7.2.4	Other full-waveform inversion methodologies	104
7.2.5	Including transmission compensation in Reverse Time Migration	106
7.2.6	Wavefield replacement operators	108
7.2.7	Application generalizations to other complex geological problems	108
8	Conclusions	109
A	Data-driven imaging for heterogenous media via automated nonhyperbolic focusing operator estimation	113
A.1	Summary	113
A.2	The Common Focus Point (<i>CFP</i>) Method	114
A.3	<i>CFP</i> implementation	115
A.4	Estimation of focusing operators by global inversion	116
A.5	Proposed <i>CFP</i> imaging workflow for gas clouds	121
A.6	Results for synthetic data	121
A.7	Results for field data	123
A.8	Conclusions and discussion	125
A.9	Acknowledgment	127
B	Recursive seismic modeling in the ray-parameter-frequency domain	129
	References	140
	Summary	145

Contents

Index	145
Samenvatting	147
Acknowledgment	149
List of papers presented and published	152
Curriculum vitae	156

1

Introduction

1.1 Wave physics: propagation through a gas cloud

In several areas around the world (e.g. offshore South-East Asia, North Sea, Black Sea) seismic exploration is complicated by the presence of so-called gas clouds. A gas cloud, as defined by Sheriff (2001), is an overburden region of low-concentration gas, escaping and migrating upward from a gas accumulation. Generally it shows as a region of severely deteriorated seismic data quality associated with low velocity and with velocity sags (push down) underneath the gas cloud overburden. The reflected events in this region appear with lower amplitude and frequency content, which is often referred to as ‘Q-attenuation or Q-absorption’ or anelastic or intrinsic loss. The effects are probably caused by incoherent scattering, absorption and poor stacking because of nonhyperbolic normal moveout. *S*-waves appear to be little affected by gas chimneys.

Seismic imaging below gas cloud is complex and current solutions that are based on a linear imaging do not yield satisfactory results. The simplified Greens functions used in these imaging algorithms do not properly describe both the kinematic and dynamic behavior of the actual wave propagation, even when the best possible velocity model is used. In addition, finding such a good velocity model itself is a major problem, due to the localized nature of the anomaly.

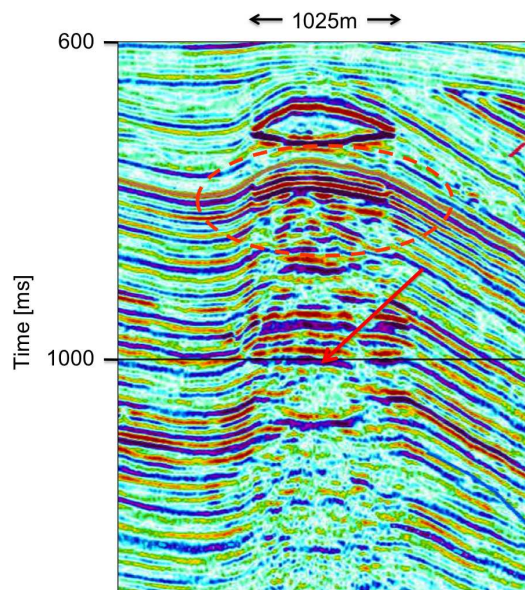


Figure 1.1 An extracted inline section from a 3D seismic field data (time-migrated cube) in the Malay basin over a gas cloud. The red ellipse shows reflected events underneath the gas cloud that appear with lower amplitude and frequency content, often refers to as ‘Q-attenuation or Q-absorption’ or anelastic or intrinsic loss. The red arrow shows the traveltime delays or time sag often apparent on reflections within and below the gas cloud due to low velocity overburden. (Data by permission from PETRONAS)

As an example, Figure 1.1 shows a strong imprint from transmission through a complex overburden containing a gas cloud.

In general, there are two major theories to explain how waves can lose their energy in complex media, such as gas clouds:

1. *Anelastic attenuation in terms of relaxation mechanism i.e. intrinsic attenuation.*

The usual explanation is squirt-flow which dissipates the wave energy into fluid turbulence and ultimately converts it into heat. Strong intrinsic attenuation is also widely observed in soft sediments and partially saturated rocks, from laboratory to seismic scales. Anelastic energy loss is due to friction between grains or fracture surfaces when the propagating wave passes through the sediments, such that part of the propagation energy is transferred into heat (White, 1975). Attenuation and dispersion effects have been modeled using a complex-valued velocity (Aki and Richards, 1980; Dvorkin and Mavko, 2006). Thomsen et al. (1997) proposed that the presence of anisotropy, implied by a shallow gas, can result in a mismatch between seismic depth and well data. Batzle et al. (2005) demonstrated via laboratory experiments on well cores that the seismic energy loss is frequency-dependent. Furthermore, they showed that bulk fluid

motion is the primary loss mechanism, which can be further affected by the interaction with the water bound in the shale. They also concluded that observations of $1/Q$ made at seismic frequencies will not normally agree with sonic-log measurements. Vogelaar and Smeulders (2007) found that a uniform porous medium with gas/water layering leads to strong attenuation and dispersion in the typical seismic frequency band.

2. Scattering attenuation in terms of physical causality.

Waves also attenuate due to internal scattering in strongly heterogeneous media. In finely-layered media this is due to intrabed multiples and mode conversions. O'Doherty and Anstey (1971) were amongst the first to discover that multiple-scattering of a wavefield due to cyclic bounces in finely-layered media produce a so-called coda (see Figure 1.2). It also produces dispersion-like effects. This phenomenon is also called 'stratigraphic filtering'. The effect of multiple-scattering in a finely-layered medium depends on both the ratio of wavelength to the layer thickness and the strength of the reflection coefficients. For the low frequencies, layered structures behave as effective medium and for higher frequencies whereby the medium can be described by the time average velocity (Stovas and Arntsen, 2006; Stovas and Ursin, 2007). Muller and Shapiro (2004) tried to quantify the combined effects of scattering attenuation due to thin layering, random diffractions and refractions, in a lossless medium in which no occurrence of an intrinsic wave attenuation.

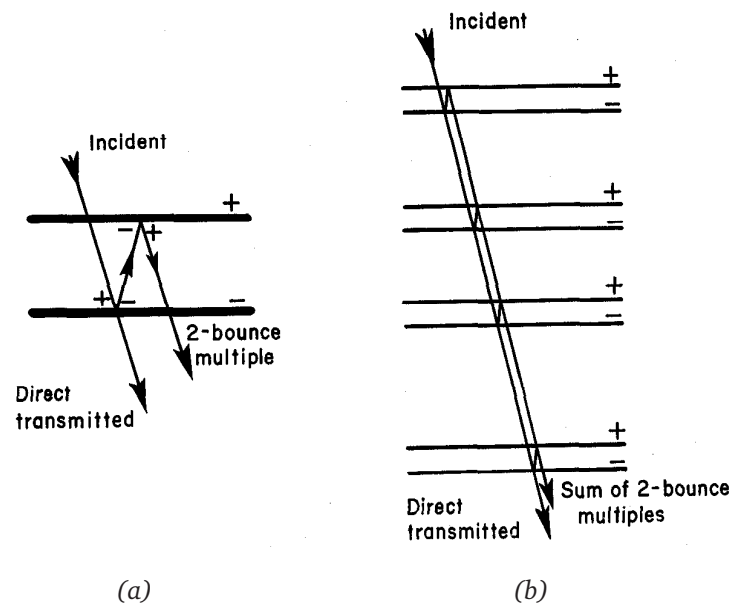


Figure 1.2 (a) The basic thin plate, defined between interfaces having reflection coefficients of opposite sign. (b) The cumulative effect of the multiple reflections from thin plates so called 'stratigraphic filtering' (from O'Doherty and Anstey, 1971; reproduced with permission from the EAGE).

In fine layering, multiple interference of the back-scattered wavefield is the main source of scattering attenuation. 3D effects such as focusing and defocusing due to diffractions and refractions can also significantly increase the transmission loss. Campman et al. (2005) have shown in laboratory experiments, that near-surface scattering due to heterogeneities can produce the same effect as Q-attenuation. Van der Baan et al. (2007) suggest that using a lower-frequency source wavelet will reduce the multiple-scattering problem in strongly heterogeneous media, at the cost of losing temporal resolution.

1.2 Geology: uncertainties

Today, there is still debate about what is the physical cause or nature of shallow gas, gas clouds and gas chimneys. They are usually described as a vertical disturbed zone, which is associated with poor image quality, caused by gas accumulations from leakage through sediments. It is generally believed that faults or fractures are the main pathway for the migration of gas towards shallower unconsolidated clastic sediments. Sometimes the gas is trapped in a shallower reservoir sand, which typically contains channels a few hundred metres below the seabottom, sealed by mud, clay, carbonate-cemented sediments or shale. Biogenic or thermogenic processes can also produce locally charged shallow gas (Schroot and Schuttenhelm, 2003). Heggland (1997) and Schroot and Schuttenhelm (2003) have also described the interpretation and the geological surface expression of shallow gas, together with its occurrence and origin.

The shallow gas accumulations commonly found in a channel complex, are recognized as strong reflection amplitude anomalies, phase variations along seismic reflections and areas of 'acoustic blanking' where no reflectors can be seen below the gas. Judd and Hovland (1992) described that the 'acoustic turbidity' which appears as chaotic reflections may result from the scattering of the acoustic energy though the presence of only 1%-5% of gas. The reflections underneath the gas exhibit a 'push-down' effect due to the decrease in the acoustic velocity (v_p) in the gas-bearing zone, and as in the example in Figure 1.1, are also weak.

The shallow gas itself shows strong reflected energy due to the large acoustic-impedance contrasts between the gas-filled finely-layered porous silt-sand-rich or clay-sand-rich clastic sediments. Typically, a high portion of the reflected acoustic energy is reflected to the surface, leaving a smaller amount of transmitted energy. An important observation here is that this reflection response contains information on the properties of the shallow gas body.

Below is a list of some of the physical geological interpretations of gas clouds (Schroot and Schuttenhelm, 2003; Judd and Hovland, 1992; Vogelaar and Smeulders, 2007; Arntsen et al., 2007):

- The geochemical signatures such as biogenic or thermogenic processes produce local gas e.g. methane, ethane, CO_2 and hydrogen sulphide. These are often associated with hydrocarbon-related diagenetic zones. They create features such as pockmarks

and mounding if gas escapes to the surface.

- From the geochemical process, escaping fluids (liquids and gasses including methane) produce macro-seepages/bubbles, which due to buoyancy, will migrate upwards through a leaking fault-system. These seepages are commonly large enough to be visible in seismic data, and are seen as vertical disturbances due to the upward movement of fluid or free-gas.
- The migrated gas travels to a shallower depth and saturates the shallow reservoirs e.g. high-porosity channel sands or finely-layered fluid-saturated porous sediments (poroelastic media), thus becoming a shallow gas-sand complex.
- Because of complicated faulting, the wavefields experience multiple-scattering and become very complex.

1.3 Problem description: kinematics and dynamics

Why are we interested in true-amplitude imaging beneath the gas clouds? The reason lies in the fact that there are many major hydrocarbon fields in the world e.g. Valhall field, Sleipner field, Haltenbanken field, Tommeliten field, Irong Barat field, Kikeh field and fields in Malaysia, Trinidad, Azerbaijan and Indonesia which are located underneath gas clouds (Heggland, 1997; O'Brien et al., 1999; MacLeod et al., 1999; Granli et al., 1999; Johnston et al., 2002; Khan and Klein-Helmkamp, 2005; Tanis et al., 2006a; Ghosh et al., 2010). A similar situation to the gas cloud problem is imaging underneath basalt, where often thin-basalt layers also produce complex wave propagation effects due to multiple-scattering. Note, however, that basalt has a high velocity as compared to the low velocity in gas (Li et al., 1998; Hanssen et al., 2003; Van der Baan et al., 2007). Due to poor seismic imaging, reservoir management becomes more difficult, as does quantifying the amount of hydrocarbons in the subsurface and confirming compartmentalization of the reservoirs.

The reflectors underneath the gas cloud, as shown in the seismic stack section in Figure 1.3, are characterized by time delays (sagging), frequency and amplitude loss, and phase distortion. Due to strong acoustic impedance contrasts and the low velocity of the gas layers, the prestack gathers show strong internal short-period multiples and nonhyperbolic moveout (see Figure 1.4). The heterogeneous nature of shallow gas-filled areas results in scattering, dispersion, internal multiples, mode conversion during wave propagation and, possibly, anelastic losses. Acoustic processing, including the use of prestack depth migration (*PreSDM*), under these circumstances, has been fraught with difficulties. Figure 1.5 shows a comparison of a Kirchhoff prestack Time Migration (*PreSTM*) image and a *PreSDM* image of the data from Figure 1.3. It demonstrates that by better honouring the propagation effects in *PreSDM* an improved image is obtained. However, very heterogeneous media, such as ones containing gas clouds, give problems in migration velocity analysis. The localized nature of the velocity anomaly also poses problems in the parameterization of the velocity model.

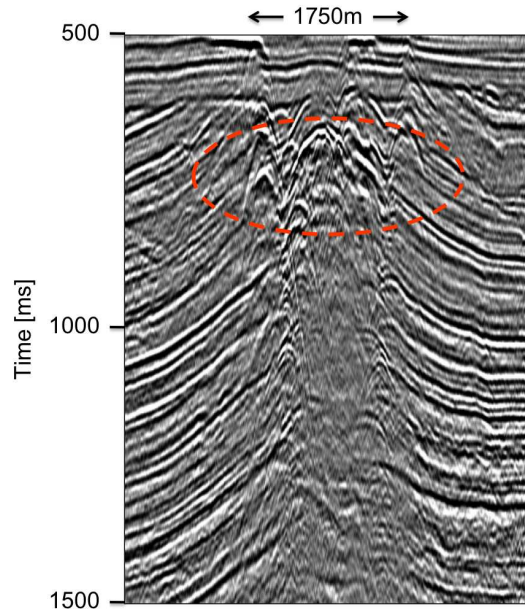


Figure 1.3 Stack section in time from one of the 3D data acquired from a field in Malaysia. The shallow gas accumulation (shallow overburden) is mainly located between 0.65 ~ 0.8s in the middle of the section, as indicated by the red ellipse. (Data by permission from PETRONAS)

Moreover, even if a proper velocity model is obtained, conventional imaging cannot correct for the complex transmission effects.

There have been several previous studies on complex wave propagation through gas clouds. O'Brien et al. (1999) built two finite-difference elastic models, which created similar gas clouds effects to those observed on the data obtained from the Valhall field. Youn et al. (2001) and Arntsen et al. (2007) have modeled, via finite-differences, gas cloud and gas chimney effects by introducing specific distributions of gas within the sediments, for example using fault networks to mimic gas chimneys. Due to poor seismic imaging and the fact that there are only a few available wells that have penetrated gas clouds, there is no in-depth knowledge as to the actual geology inside a gas cloud or chimney. Malme et al. (2003) and Swan (1991) also investigated the effects of overburden distortions for Amplitude-Variations-with-Offset (AVO) studies due to shallow diffractions, shallow lenses and fine layering. Brandsberg-Dahl et al. (2003) have shown that the common-offset Kirchhoff PreSDM fails to produce focused events due to multi-pathing and complex wave propagation caused by the shallow gas. Wagner et al. (2001), Tanis et al. (2006a) and Kabir et al. (2008) tried to estimate the velocity model using both reflection and wave-equation-based tomography. Their aim was to update the localized strong velocity contrast for imaging underneath the gas clouds, in order to correct the kinematics. Prieux et al. (2009) assessed the reliability of 2D acoustic frequency-domain full-waveform inversion to image shallow-water synthetic

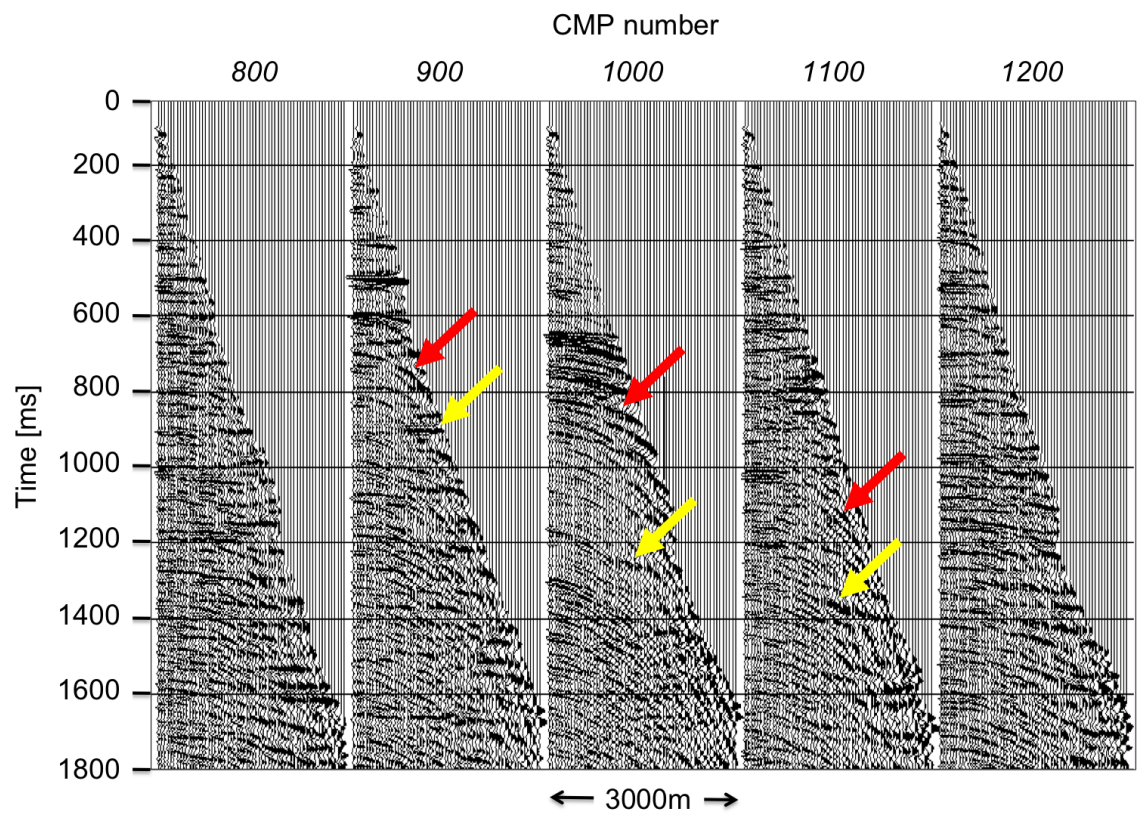


Figure 1.4 Common-Mid-Point (CMP) gathers related to the data shown in Figure 1.3. CMP numbers 900, 1000 and 1100 show strong internal multiples (at 0.6s and below as indicated by the red arrows) due to the unconformity and the gas layer. The yellow arrows indicate primary reflections below the gas cloud that are heavily obscured by the internal multiples. (Data by permission from PETRONAS)

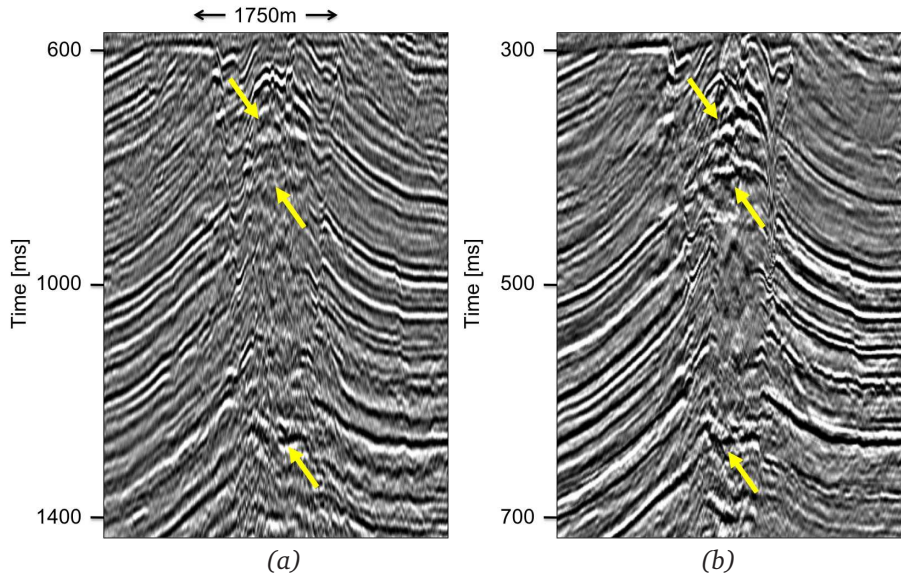


Figure 1.5 (a) The Kirchhoff prestack time migration (PreSTM) result and (b) the PreSDM image (displayed in oneway time) of the same data in Figure 1.3. The arrows in Figure 1.5b show the improvements inside and underneath the gas cloud where better focusing was achieved by improved traveltimes estimation honouring nonhyperbolic moveout, thus ensuring better amplitude focusing below the complex subsurface. (Data by permission from PETRONAS)

data with a gas cloud, using first arrival traveltimes tomography and reflection stereo tomography. This necessitates long-offset data acquisition.

We believe that a large part of the observed attenuation effects is primarily due to complex wave propagation, rather than anelastic losses. All attenuation effects together lead to a significant deterioration of the seismic image below a gas cloud. This is evident as amplitude attenuation and incorrect focusing due to the strong lateral variations of the overburden.

1.4 Current approaches to gas-cloud problems

Currently, there are several approaches to mitigating the problems encountered when imaging underneath gas clouds or gas chimneys. These solutions address either the kinematics, i.e. getting the accurate Green's functions via wavefield tomography, or the dynamics, i.e. Q-estimation and Q-compensation. There are also approaches to solve the kinematic and the dynamic problems simultaneously using Q-migration or inverting for the Q-model and then incorporating the Q-model in a migration solution. These approaches are not exactly true-amplitude because they assume that the target amplitude bandwidth below the gas cloud is the same as for the background sediments. As a result, any true-amplitude response from the reservoir will be scaled to the background amplitude.

1.4.1 Q-attenuation and compensation

Most current approaches to obtaining true amplitudes below gas clouds are rather indirect. For example, in so-called Q-compensation, correction factors are derived by measuring the surrounding frequency content and calculating the amplitude ratio of frequency losses below the gas and the surrounding area. The corresponding factors include corrections for the wavelet phase and amplitude.

Attenuation is defined as the relative loss of energy of a plane wave per unit cycle, $\frac{\Delta E}{E}$ and is characterized by the inverse Q-factor (see Johnston et al., 1979; Sheriff, 2001; Mavko et al., 2003; Sengupta and Dutta, 2005) :

$$Q^{-1} = \frac{\Delta E}{2\pi E}, \quad (1.1)$$

The inverse Q is related to attenuation constant α , the propagation velocity c and as well as frequency f :

$$Q^{-1}(\omega) = \frac{2\alpha(\omega)c}{\omega}. \quad (1.2)$$

Commonly, Q is estimated via logarithmic amplitude spectral ratios of the desired bandwidth of interest ($A(\omega)$) and the amplitude of the background bandwidth ($A_0(\omega)$) after traveling over a distance x , with phase velocity c and reflection coefficient corrected for spherical divergence R_c (see Dasgupta and Clark, 1998):

$$\ln \left[\frac{A(\omega)}{A_0(\omega)} \right] = \ln R_c + \left[\frac{x}{4\pi c} \ln \left(1 - \frac{2\pi}{Q} \right) \right] \omega. \quad (1.3)$$

By plotting the logarithmic spectral ratios of $A(\omega)$ and $A_0(\omega)$ as a function of frequency, a linear trend is obtained, where the slope, p_f , is a function of Q:

$$Q = \frac{2\pi}{1 - e^{4\pi p_f c/x}}. \quad (1.4)$$

Inverse-Q filtering can be applied during processing, to compensate for absorption effects. There are a number of Q-factor estimation techniques such as estimation from common-mid-point gathers (Dasgupta and Clark, 1998; Zhang and Ulrych, 2002) or estimation using a Gabor transform (Wang, 2004).

In general, elastic waves do not attenuate in a very dry rock (i.e. Q is very large). This means that the amplitude loss is linked to the pore fluid triggered by the passing wave. Typically a gas sand with 12% porosity has a Q-factor of 5 to 10, whereas it exceeds 100 for an oil- and water-saturated rock. Thus, attenuation is large in rock with partial gas and small in liquid-fill rock (Dvorkin and Mavko, 2006). This also means that the Q-factor is highly dependent on the parameters such as lithology, porosity and pore-fluid characteristics.

Solutions for solving the kinematics and dynamics that are based on Q-estimation and compensation (for example inverse Q-migration, inverting for Q-model or 3D PSDM that compensate amplitude and bandwidth along raypaths to every image point for frequency dependent absorption and dispersion), have proved can improve images underneath gas clouds (Bear et al., 2008; Traynin et al., 2008; Cavalca and Fletcher, 2008; Xie et al., 2009). During the migration-imaging, the calculated kinematics (either by ray-tracing or solving the eikonal equation) allow migration to compensate for amplitude loss and phase distortion on the basis of dispersion, for every raypath relative to the background with the estimated absorption model. Nevertheless, these techniques are not really true amplitude and getting the correct Green's functions is not easy when a very accurate velocity model is required.

1.4.2 Depth conversion

Overburden velocity anomalies create systematic errors for depth conversion (Al-Chalabi, 1976). When interpreted in time, reflected events below will have a false geological structure in depth. In the case of a gas cloud, the events underneath appear pushed-down due to low velocity anomalies as shown by the ellipse and arrow in Figure 1.1. Although it is geologically an anticline structure, most of the reflected events have time delays giving the structures either a flat or a 'sagging' appearance. At later times as the wavefield travels deeper, it is 'healed' and shows less overburden imprint (Al-Chalabi, 1976). Velocity picking for the maximum coherency semblance in stacking velocity analysis is hampered both by the poor signal-to-noise ratio and nonhyperbolic moveout of the reflected events. In most cases, the gas cloud contains strong acoustic impedance contrasts. These produce strong internal multiples, which obscure deeper primary reflection events and complicate the velocity analysis.

Armstrong et al. (2001) state in their case study that as shown in Figure 1.6, the presence of low-velocity overburden anomalies, introduces nonhyperbolic moveout on the reflections below the anomalies, which in turn produces faster velocity picks. This is because the velocity picks are based on the assumption of hyperbolic moveout. In contrast to the picked stacking velocities, the average velocity is actually slower underneath the low velocity overburden. To mitigate this, they suggested the usage of a time-correction method at the target horizons using the apparent width of the velocity anomaly and source-receiver offsets at the recording datum.

Figure 1.7b demonstrates schematically a migrated post-stack section with slow and fast velocity anomalies while Figure 1.7a shows the depth section containing these anomalies. The seismic time horizons show kinematic time delays as a result of 'push-down' or 'sagging' underneath low velocity anomalies and 'pull-up' underneath fast velocity anomalies.

1.4. Current approaches to gas-cloud problems

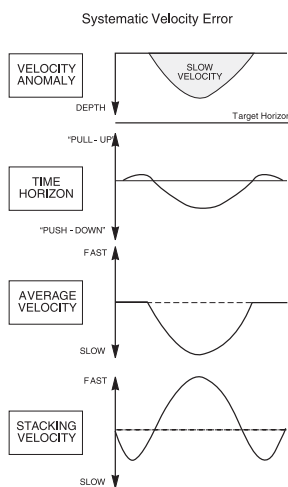


Figure 1.6 Stacking and average velocity response due to low velocity overburden anomaly (from Armstrong et al., 2001; reproduced with permission from the EAGE).

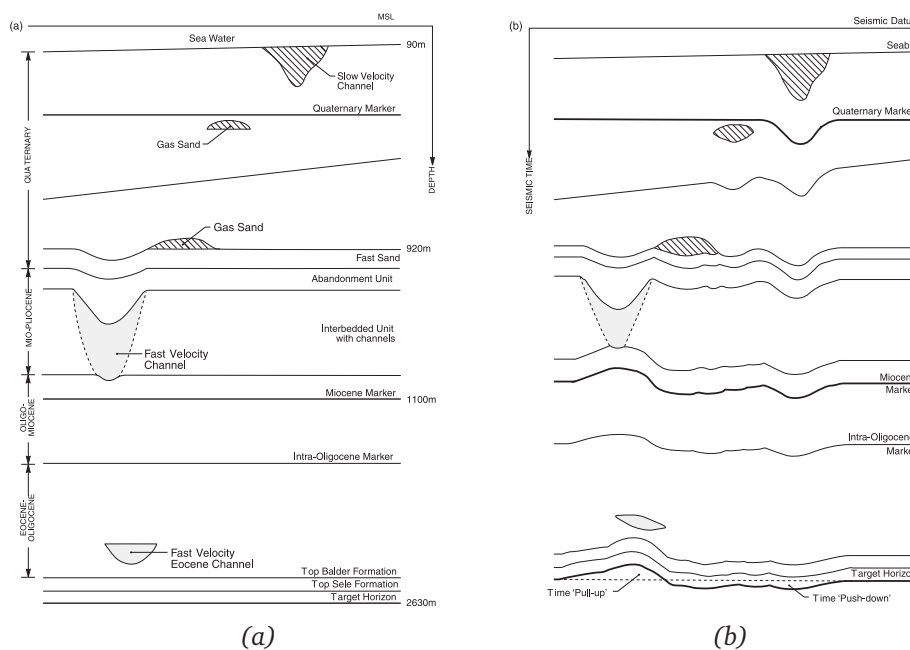


Figure 1.7 (a) Schematic depth section through an overburden containing velocity anomalies (b) Equivalent migrated post-stack section. Seismic time horizons show 'push-down' or 'sagging' underneath low velocity anomalies and 'pull-up' underneath fast velocity anomalies (from Armstrong et al., 2001; reproduced with permission from the EAGE).

1.4.3 Tomography: Building an accurate velocity model

A better way to image below gas is via depth migration, since this can potentially resolve the time-sagging problem. However, building an accurate velocity model for PreSDM, incorporating anomalies such as gas clouds, is not easy, particularly when we want to get the correct kinematics of the reflected events underneath the overburden. Since the anomaly is often shallow and has poor short-offset coverage, any shallow velocity estimation that is based on a moveout will be problematic. Figure 1.8 shows a crossline section from another 3D field dataset in the Malay basin, Malaysia (after Oezsen et al., 1999; see also Ghosh et al., 2010). After corrections for the kinematics using an accurate velocity model and proper PreSDM, scattered wavefields can be properly back-propagated to the image points, thus producing a better-focused depth image. In other words, the acoustic energy is apparently not totally lost due to absorption, but rather scatters in a 3D sense. Tanis et al. (2006a), Tanis et al. (2006b) and Kabir et al. (2008) devised a workflow utilizing diving-wave refraction tomography, reflection tomography and wave-equation tomography in order to produce a reliable and accurate velocity model that includes the near-surface velocity anomaly. Wave-equation based tomography is effective in updating the strong local velocity contrast created by the presence of shallow gas. Note, however, that a correct velocity model will not remove the effects of complex scattering inside the gas cloud, hence the coda-effect will remain after PreSDM.

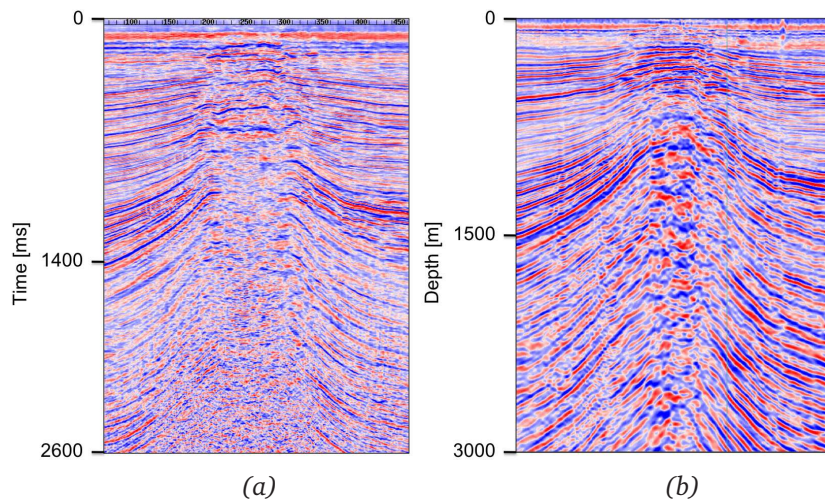


Figure 1.8 (a) Poststack migrated image of a crossline from a field in the Malay basin, Malaysia. (b) 3D Kirchhoff PreSDM result. Reflected events are clearly better focused inside and underneath the gas cloud after PreSDM. (after Oezsen et al., 1999; with the permission from PETRONAS)

1.4.4 Multicomponent seismic methods

One way of imaging through gas clouds is to use converted waves (MacLeod et al., 1999; Granli et al., 1999; Hornman, 2004). Not many anelastic wave propagation behaviour studies have been carried out for the situation of gas clouds and their transmission effects. Shear-wave propagation is hardly affected by gas pockets since shear waves (S -waves) travel via the rock matrix as opposed to within the fluid, they are therefore unaffected by the compressibility of the fluid. Similarly, shear-wave measurements have to be made on elastic boundaries, and for marine data, require multicomponent ($4C$) measurements. The effectiveness of $4C$ -Ocean Bottom Cable (OBC) technology to handle gas-related imaging distortions has been demonstrated in several examples worldwide (Li et al., 2001). However, imaging converted waves still requires P -waves model for the downgoing propagation, and for both P - P and P - S imaging, a good P -waves model and corresponding P -waves operators are still required. Granli et al. (1999) and Hornman (2004) showed that the most important aspect in a marine multicomponent seismic acquisition is the downgoing compressional waves before conversion to shear waves at the target. If the compressional wave gets attenuated, less energy is available for the upgoing shear waves.

Converted-wave imaging also requires a velocity model for the S -waves propagation, and this is difficult to estimate from the converted-wave data alone. In the case of large gas clouds, undershooting the gas cloud is no longer possible for either P - P or P - S imaging because the gas acts as a barrier to the downgoing P -waves.

There are also limitations to the multicomponent data approach, in particular, multicomponent acquisition is very expensive and there remains a lack of proper tools to process multicomponent data for complex media. It is also difficult to correlate geological events in time on P - P and P - S sections, since *Common Conversion Points (CCP)* are affected by the v_p/v_s ratio and errors in velocity estimation also affect the final seismic image. Another major drawback is that a correct decomposition of the seismic wavefield into a clean P - P and P - S data remains difficult due to acquisition problems such as the coupling of receivers to the seabottom.

Advantages of multicomponent measurements over conventional seismic acquisition:

- the S -waves are (almost) unaffected by shallow gas zones, gas clouds and hydrocarbon-bearing reservoirs;
- they may allow rock / fluid detection based on combined P and S data;
- they can provide data for AVO-based modeling studies leading to improved reservoir property models;
- the effectiveness of the multicomponent seismic $4C$ -Ocean Bottom Cable (OBC) technology to handle gas-related imaging distortions has been demonstrated in several cases worldwide.

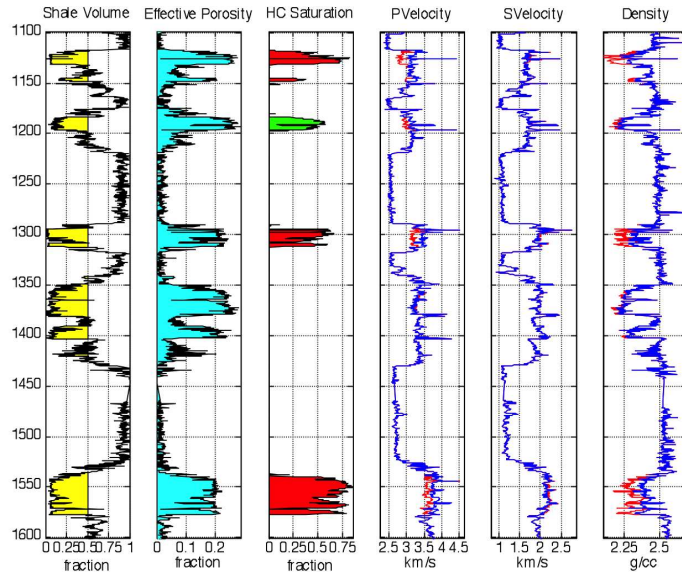


Figure 1.9 Well logs and their derived properties for one location in the Malaysian basin. Panels of P -velocity, S -velocity and density show fluid-replacement response where the brine (blue) curves were substituted for the oil and gas response at the reservoirs. The red curves represent the measured responses. The S -velocity is not affected by the fluid changes. (Data by permission from PETRONAS)

Limitations on multicomponent seismic are:

- acquisition, processing and imaging of multicomponent data is expensive;
- lack of proper tools in processing multicomponent data from complex media. For example, it is difficult to correlate geological events in time for the P - P section and the P - S section since Common Conversion Points are affected by the v_p/v_s ratio;
- errors in velocity estimation affect the final seismic image;
- few anelastic wave-propagation studies have been done for gas clouds and their transmission effects;
- an accurate P -waves model is required to describe downward propagation.

The log information in Figure 1.9 is taken from a well located in the Malaysian basin. The gas reservoirs were replaced by brine using fluid-replacement methods (in this case, Gassmann's fluid substitution; see Mavko et al., 2003). The P -waves and S -waves velocities were measured using sonic and dipole-sonic tools over the reservoirs. The figure shows that, after fluid replacement, the S -waves velocity was not affected by the fluid content whereas the P -waves velocity and density are. The red curves represent the restored gas and the blue

curves are the substituted brine. In the shale column, sand bodies are marked yellow. The maximum porosity is 20%. The hydrocarbon saturation column (*HC*) shows hydrocarbon content in the reservoirs. Therefore, if *S*-waves data can be measured successfully over a gas cloud or gas-related problem area, they should not be affected by the fluid, but only see the geology.

1.5 Limitations of current seismic imaging

All linear imaging methods require an accurate velocity depth background model because they assume the subsurface consists of small contrasts superimposed on a background model. Methods based on small contrasts does not take into account multiple-scattering (often called the coda). The simplified Green's functions used in these algorithms also do not properly describe the kinematics and dynamics of visco-elastic wave propagation in high-contrast, highly heterogeneous media (see e.g. Gisolf and Verschuur, 2010).

In general, the current prestack depth migration algorithms are limited by:

- the need for background velocity model that is smooth yet accurate;
- the absence of any compensation for transmission effects;

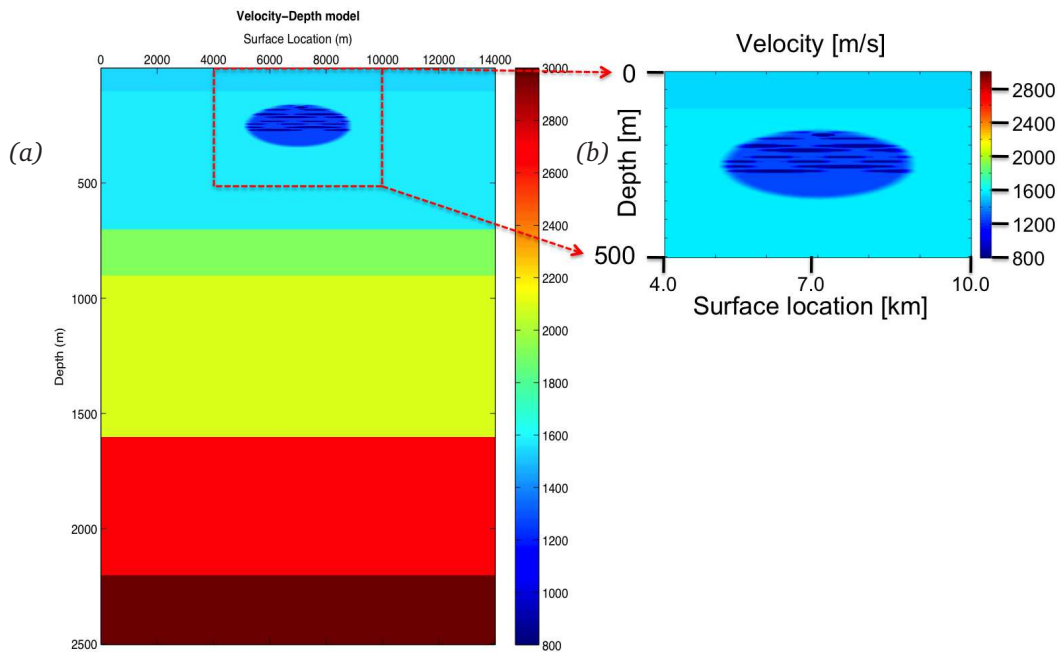


Figure 1.10 (a) The velocity model [m/s] for a numerical modeling used to study a gas cloud effects seen in the real data in Figure 1.1. (b) Zoom of the velocity model in the gas cloud area in (a).

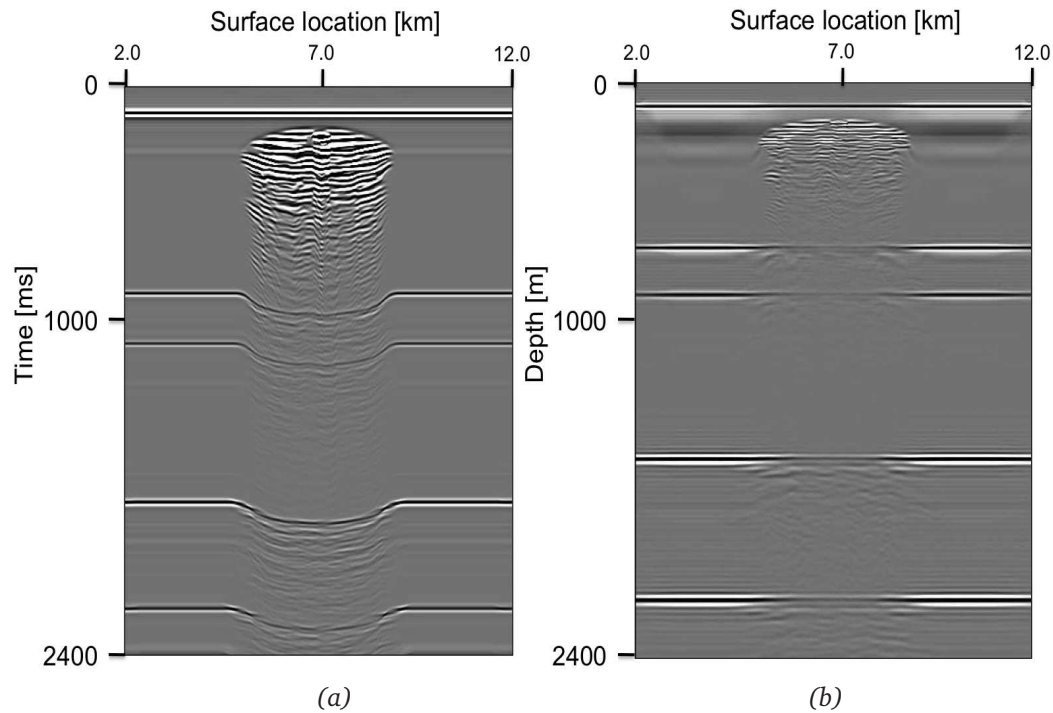


Figure 1.11 (a) Stack section of the synthetic data for the velocity model in Figure 1.10. (b) Prestack depth migration of the data in (a) using the exact velocity model and wave-equation migration.

- inability to compensate for multiple-scattering such as internal multiples;
- structural dip; some algorithms cannot image beyond ninety degrees angle;
- maximum migration frequency;
- computing power.

Numerical studies on gas cloud imaging problems can provide useful insights on these issues. The velocity model shown in Figure 1.10 was designed to mimic a gas cloud similar to that seen in the real data in Figure 1.1. The data is forward-modeled using an acoustic finite-difference algorithm and the resulting stacked section is shown in Figure 1.11a. Note that the influence of the low-velocity anomaly on this time section results in time delays and poor quality reflections underneath the gas cloud. Figure 1.11b shows a prestack depth migration result from a recursive wave-equation migration using the exact velocity model. It shows that the kinematics can be solved satisfactorily in the gas cloud area, but that the amplitude imprint and coda remain for all deeper reflectors below the gas cloud overburden.

1.6 Thesis objective

We have been working on a new approach to seismic imaging below anomalies, such as gas clouds. We believe this new full-waveform inversion-based approach can contribute to this currently largely-unsolved problem.

Whereas most traditional solutions aim at effective amplitude and phase corrections to the seismic reflections (removing the ‘absorption’ or the ‘attenuation’ effect), our approach describes the problem as a complex scattering phenomenon. Therefore, we aim to find an effective gas cloud property model which explains the gas cloud reflection response from which full-waveform deconvolution operators can be determined. We demonstrate this methodology for 1.5D and 2D media and finally on a 2D line with real data.

An important part of this method is estimating the full-waveform transmission operators for propagation through the gas cloud from the gas cloud reflection response and determin-

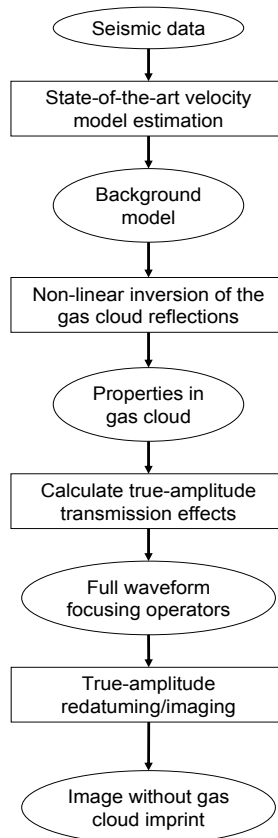


Figure 1.12 Proposed strategy for gas cloud imaging and inversion.

ing the inverse transmission-deconvolution strategy. The gas cloud reflection response itself provides vital information on the energy transmitted through the gas. By inverting this response to get the effective medium properties that describe the reflection response of the gas cloud, transmission operators can be derived. When using these transmission operators in a multidimensional, full-waveform deconvolution process, true-amplitude imaging of the reflections below this overburden can be achieved. The main idea in this thesis is to perform depth-redatuming of seismic data using full-waveform transmission operators that are estimated a priori from the result of full-waveform inversion of the gas cloud reflection. In essence, this is a more robust and more sophisticated form of ‘layer stripping’. The proposed strategy is summarized in Figure 1.12.

In the first stage, the kinematics required to focus the wavefields is addressed with the help of a state-of-the-art velocity modeling approach, in which imaging operators are derived from the seismic data in a hands-off manner. This corrects for kinematic aspects of the propagation effects. In the second stage, we aim at correcting the overall dynamics effects from gas inclusions, anelastic attenuation, complex geometrical spreading and internal multiples, for a better true-amplitude imaging. A nonlinear full-waveform inversion process will be employed to image the actual contrasts within the gas cloud. In the third stage, the transmission effects of the gas cloud area are described properly using the estimated properties model of stage two while in the fourth and final stage, compensation are applied for the transmission effects, so as to provide true-amplitude image below the anomaly.

1.7 Thesis outline

In Chapter 2, we discuss the Kirchhoff and Rayleigh II integrals and their features and limitations especially in heterogeneous media. For strongly inhomogeneous media, back propagation of a wavefield, even when using the perfect Green’s function, is theoretically incorrect. For true-amplitude inverse wavefield extrapolation below a complex area, multidimensional deconvolution with the Green’s function is required. In Chapter 3 we formulate an inversion strategy where we propose a full-waveform transmission deconvolution method and use the transmission operators for full-waveform redatuming. The proposed forward modeling formulation is already suited to 3D, but we only demonstrate the method using a 2D example. We believe that the gas cloud’s reflection response provides vital information on the gas cloud itself. Thus, by using the gas cloud reflection response, we invert for its effective-medium properties. Based on these properties we forward model the transmission operators and estimate the inverse transmission-operators by least-squares inversion. Due to the strong nonlinearity of the gas cloud problem, we opt for a Genetic Algorithm to invert for the effective-medium properties, as described in Chapter 4. We also develop a strategy for faster convergence in the 2D case, for example, by including ‘blended acquisition’.

Chapter 5 discusses the feasibility of this inversion strategy using numerical experiments for 1.5D and 2D situations. We show that the gas cloud reflection response is invertible for its medium properties. To demonstrate the theory, in Chapter 6 we implement the proposed

method on real data from the Malaysian basin. Finally, in Chapters 7 and 8 we present our conclusions, discussions and recommendations for future research.

2

Wavefield extrapolation in heterogeneous media

2.1 Wavefield extrapolation in homogeneous media

Forward and backward extrapolation of wavefields is central to seismic imaging. It can be performed in either the time or space domain via Kirchhoff or Rayleigh integral implementations using Green's Theorem. Berkhout (1982), Wapenaar and Berkhout (1989) and Gisolf and Verschuur (2010) explain in great detail the development of wave-equation theory for acoustic and elastic wavefield extrapolation from Gauss's Theorem to Green's Theorem. In this thesis we refer to the above literature for a description of the full theory. We use the convention of the superscripts '+' and '-' to denote downward and upward propagating wavefields respectively. The position is denoted with the Cartesian coordinate vector $\vec{r}=(x,y,z)$ where the direction of z is pointing downward unless stated otherwise. Wavefields indicated with a capital (P,G) are assumed to be in the frequency domain, whereas lower case (p,g) indicates the time domain.

We will start deriving the formulation of wavefield extrapolation in heterogeneous media by first looking at the Kirchhoff integral. For media fully contained inside a closed surface on which measurements can be taken, forward and backward extrapolation of the wavefields can be achieved by using the Kirchhoff integral for a homogeneous medium. When imaging the subsurface, most seismic imaging techniques use the Rayleigh II integral instead of the Kirchhoff integral because of the following limitations (Gisolf and Verschuur, 2010):

- application of the Kirchhoff integral requires seismic wavefield acquisition to measure both P and $\nabla P \cdot \underline{n}$, as in Equation 2.1 below;
- it is not possible to measure wavefields along a closed surface.

The Kirchhoff integral states that the wavefield measured on a closed surface S , can be extrapolated to any point inside the volume (V) using causal, or anticausal Green's functions, if the sources of the wavefield are outside the volume (Figure 2.1). As long as the pressure field P and the derivatives of the pressure field ∇P are measured, extrapolation of the wavefield both forward and backward in time, to a point (A) inside S , are equally valid:

$$P(\vec{r}_A) = - \oint_S (P \nabla G - G \nabla P) \cdot \underline{n} dS. \quad (2.1)$$

The Green's function (G) is the solution of the Helmholtz equation with a point-source (causal), or a point-sink (anticausal), at point A :

$$\nabla^2 G + \frac{\omega^2}{c^2} G = -\delta(\vec{r} - \vec{r}_A). \quad (2.2)$$

The wavefield P must obey the source-free Helmholtz equation:

$$\nabla^2 P + \frac{\omega^2}{c^2} P = 0. \quad (2.3)$$

The causal Green's function (G), in a homogeneous medium with velocity c , is expressed by:

$$G(\vec{r}_A, \vec{r}; \omega) = \frac{e^{-j\omega R/c}}{4\pi R}, \quad \vec{r}_A \in V, \quad (2.4)$$

and the gradient of G can be written as:

$$\nabla G = -\frac{1}{4\pi} \left[1 + \frac{j\omega R}{c} \right] \frac{e^{-j\omega R/c}}{R^2} \nabla R, \quad (2.5)$$

where R is the absolute distance between the point A inside the volume and the measurement location.

Forward extrapolation of the wavefield to a point A , which requires calculating the wavefield at later times than when it was measured on S , can be accomplished using the causal Green's function. Backward extrapolation in time or back propagation of the wavefield, where the wavefield in A is calculated at earlier times than it was measured on S is achieved using the anticausal Green's function, which is the complex conjugate of the causal Green's function (i.e. G^*). Figure 2.2 shows the causality arguments where the source location, with respect to the measurement location dictates the extrapolation solutions. Measurements of the source wavefield along the blue part of S in this case allows the forward prediction of

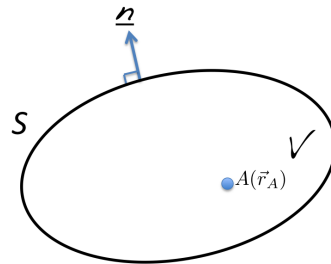


Figure 2.1 The Kirchhoff integral states that any wavefield can be extrapolated to any arbitrary point inside volume (V), if measurements were made along this closed surface (S). Measurements should consist of the wavefield and its derivative along normal vector \underline{n} .

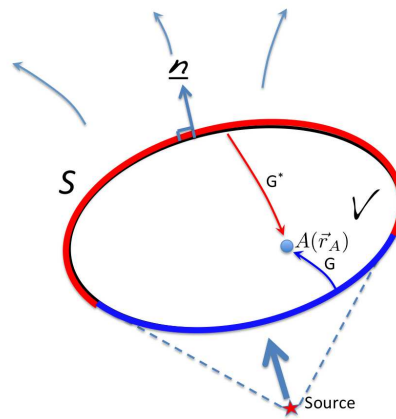


Figure 2.2 Forward and backward extrapolation using the Kirchhoff integral. G denotes the causal Green's function and G^* is the anticausal Green's function. Given the location of the source we can distinguish a blue part of the surface S where the energy is flowing into volume V , and a red part through which the energy is flowing out of V .

the wavefield in A . On the other hand, measurements along the red part of S can be used to back propagate the wavefield to point A .

In calculating the wavefield extrapolation for seismic exploration, we cannot measure around the earth as a closed volume, but only along part of the surface which is also assumed to be flat. We therefore use the Rayleigh integral since as opposed to the Kirchhoff integral, this uses only one term containing either P or ∇P measured along an infinite flat surface as shown in Figure 2.3. This is only valid if an infinite flat plane separates the sources of the wavefield P , from the extrapolation point A .

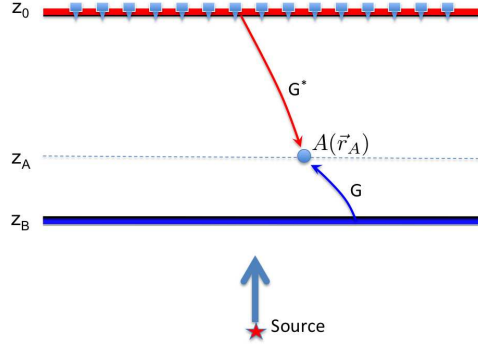


Figure 2.3 Forward and backward extrapolation using the Rayleigh integral. The Rayleigh integral only requires either P or $\nabla P \cdot \underline{n}$ measured along an infinite surface, thus reducing the requirement to have two measurements along a closed surface.

It can be shown for homogeneous media (see Gisolf and Verschuur, 2010) that Equation 2.1 now reduces to the Rayleigh integral:

$$P(\vec{r}_A) = -2 \int_S P \nabla G \cdot \underline{n} dS. \quad (2.6)$$

For the normal derivative of the causal Green's function we get:

$$\frac{\partial G}{\partial z_0} = \frac{z_A(1 + j\omega \Delta r/c)}{2\pi \Delta r^3} e^{-j\omega \Delta r/c} = -\frac{\partial}{\partial z_A} \frac{e^{-j\omega \Delta r/c}}{\Delta r}, \quad (2.7)$$

where $\Delta r = \sqrt{(x - x_A)^2 + (y - y_A)^2 + z_A^2}$.

For the forward-propagated wavefield P_A at point A we then get:

$$P(\vec{r}_A; \omega) = \frac{z_A}{2\pi} \iint_{-\infty}^{\infty} dx dy P(x, y, z_B; \omega) \left(1 + j\omega \frac{\Delta r}{c}\right) \frac{e^{-j\omega \Delta r/c}}{\Delta r^3}. \quad (2.8)$$

with $\Delta r = \sqrt{(x - x_A)^2 + (y - y_A)^2 + (z_B - z_A)^2}$.

For the backward-propagated wavefield at point A , we get:

$$P(\vec{r}_A; \omega) = \frac{z_A}{2\pi} \iint_{-\infty}^{\infty} dx dy P(x, y, z_0; \omega) \left(1 - j\omega \frac{\Delta r}{c}\right) \frac{e^{j\omega \Delta r/c}}{\Delta r^3}. \quad (2.9)$$

with $\Delta r = \sqrt{(x - x_A)^2 + (y - y_A)^2 + (z_0 - z_A)^2}$.

Note that in expression (2.9), evanescent waves are ignored (Wapenaar, 1992).

2.2 Seismic imaging in low-contrast inhomogeneous media

In the case of an inhomogeneous medium inside the volume V , the total wavefield P at an arbitrary point A can still be extrapolated accurately using the Kirchhoff integral. This can be achieved from the measurements at the closed surface S if we are able to calculate the Green's functions exactly in the inhomogeneous medium. However these Green's functions are no longer one-way but may contain two-way wave propagation and therefore the one-way assumption made for the derivation of the Rayleigh integral is no longer valid.

The Kirchhoff integral in an inhomogeneous medium, can easily be derived (see Gisolf and Verschuur, 2010) and written as:

$$P(\vec{r}_A; \omega) = \rho \oint_V \frac{1}{\rho} [G \nabla P - P \nabla G] \cdot \underline{n} dS, \quad (2.10)$$

where ρ is the density of the medium,

For imaging in a low-contrast inhomogeneous medium, we assume that the recorded wavefield P is scattered only once. The medium is considered to consist of low-amplitude variations (contrasts) with respect to a smoothly-varying background medium. The total wavefield is the sum of the incident wavefield in the background and a singly-scattered field that is also propagating in the background:

$$P_{tot} = P_{sct} + P_{inc}. \quad (2.11)$$

When the scattered field is assumed due to the contrasts, Equation 2.10 tells us that the Green's function should be interpreted at the contrasts and defined in the background medium only. The Green's function can be approximated by using the direct traveltime from point A to the receivers (t_G) in the smooth background medium. For the anticausal Green's function needed for back-propagation we get:

$$G(\vec{r}, \vec{r}_A; \omega) = \gamma e^{j\omega t_G}, \quad (2.12)$$

where γ is an amplitude factor that compensates for the geometrical spreading involved in the propagation.

For the derivation of the Green's function we get:

$$\frac{\partial G}{\partial z} = \left(\frac{\partial \gamma}{\partial z} + j\omega \gamma \frac{\partial t_G}{\partial z} \right) e^{j\omega t_G}, \quad (2.13)$$

and the backward-extrapolating Rayleigh integral becomes:

$$P(\vec{r}_A; \omega) = 2\rho \iint_{-\infty}^{\infty} dx dy \frac{P}{\rho}(x, y, z_0; \omega) \left(\frac{\partial \gamma}{\partial z} + j\omega \gamma \frac{\partial t_G}{\partial z} \right) e^{j\omega t_G}. \quad (2.14)$$

Since in seismic imaging we only consider far-field energy, i.e. the distance between the measurement locations and the locations of the heterogeneities are large in terms of seismic wavelengths, the term $\frac{\partial \gamma}{\partial z}$ can be neglected and Equation 2.14 simplifies to:

$$P(\vec{r}_A; \omega) = 2j\omega\rho \iint_{-\infty}^{\infty} dx dy P \left[\frac{\gamma}{\rho} \left(\frac{\partial t_G}{\partial z} \right) \right] e^{j\omega t_G}. \quad (2.15)$$

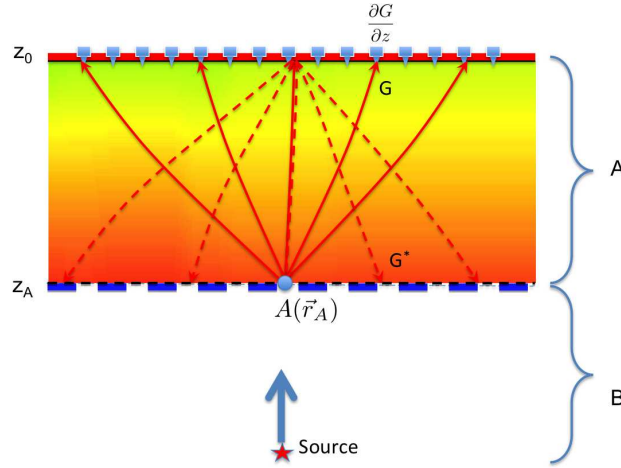


Figure 2.4 Rayleigh integral in a smooth inhomogeneous medium. Causal forward propagation from z_A to z_0 is carried out with the causal Green's function (G). Back propagation from z_0 to z_A is carried out with the anticausal Green's function (G^*).

For low-contrast inhomogeneous media, the Green's functions can be estimated using either ray tracing through the background medium or using an eikonal solver in the smooth varying background medium. However we would need to have a good background velocity model in order to generate accurate Green's functions. In low-contrast media backward extrapolation or back propagation of the wavefields can be achieved with the help of the complex conjugate of the causal Green's functions. Note that this is not applicable in very high-contrast heterogeneous media such as a gas cloud, where the Green's functions are far more complicated and complex.

Figure 2.4 shows the setup for the Rayleigh integral in a smooth inhomogeneous medium. The upgoing wavefield $P^-(z_0)$ recorded at the surface z_0 can be written as:

$$P^-(z_0) = \int_{z_A} dS P^-(z_A) \frac{\partial G}{\partial z}. \quad (2.16)$$

Similarly we can write:

$$P^-(z_A) = \int_{z_0} dS P^-(z_0) \frac{\partial G^*}{\partial z}. \quad (2.17)$$

which describes the upgoing wavefield in A in terms of the surface recordings at z_0 by back propagation.

2.3 Seismic imaging in high-contrast heterogeneous media

In the previous section we saw that forward and backward extrapolation can be achieved by interchanging the causal and anticausal Green's functions. For high-contrast heterogeneous media, this is no longer valid because the upgoing wavefield and Green's functions become more complicated. This is illustrated in Figure 2.5 which shows the configuration for the total upgoing wavefield P_0^- at the surface datum z_0 . P_B^+ is the wavefield that propagates downward into area B , after having been transmitted through area A . P_B^- is the wavefield that is reflected by the reflectors in area B . Wavefield P_{0B}^- is the upgoing wavefield that comes from area B after passing through area A again and finally arriving at the surface. $P_{B_{sct}}^+$ is the downgoing scattered wavefield in area B due to the scatterers in area A . This wavefield is not recorded at the surface. The datum z_A is an arbitrary datum that has no physical meaning, but which separates the area that contains the overburden such as the gas cloud from the target reflector area underneath (B). Wavefield P_B^- is the wavefield of interest that needs to be deconvolved for the transmission effects of the gas cloud.

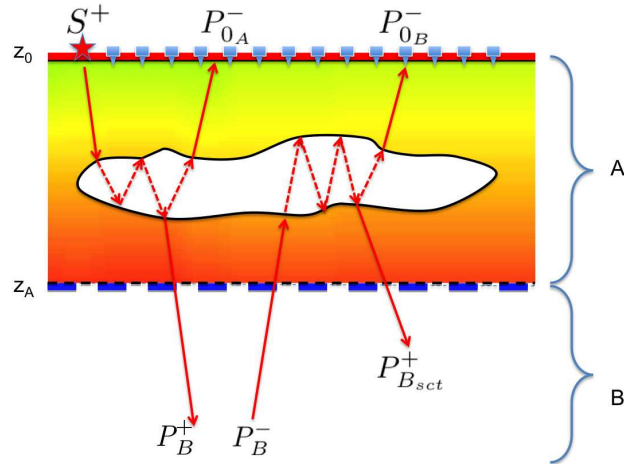


Figure 2.5 The total observed upgoing wavefield P_0^- consists of upgoing wavefield responses P_{0A}^- and P_{0B}^- from areas A and B respectively. S^+ is a bandlimited incident source wavefield. Wavefield P_B^- is the upgoing wavefield from area B and has propagated through A twice.

2.3.1 Forward model

In seismic measurements the source for all wavefields, downgoing and upgoing, is usually located at the surface. The total upgoing wavefield at the surface datum z_0 is the sum of wavefield responses from the areas A and B .

The recorded wavefield P_0^- can be expressed as:

$$P_0^-(z_0) = P_{0A}^- + P_{0B}^-, \quad (2.18)$$

where P_{0B}^- is given by Equation 2.19.

The forward model for the upgoing wavefield P_{0B}^- for high-contrast heterogeneous media can be written as:

$$P_{0B}^-(z_0) = \int_{z_A} dS P_B^- \frac{\partial G}{\partial z}, \quad (2.19)$$

where P_B^- is the upgoing wavefield from area B , but where G is the causal Green's function propagating from datum z_A to the datum surface z_0 , in the true medium, not the background medium.

From Equation 2.19, we argue that backward extrapolation of the wavefield P_{0B}^- to the level z_A is no longer valid, because the downgoing wavefield $P_{B_{sct}}^+$ is not taken into account. Therefore, in order to recover the upgoing wavefield of P_B^- at level z_A from the total upgoing wavefield P_0^- , we have to either invert or deconvolve Equation 2.19 for the full-waveform transmission operator, instead of switching to an anticausal (complex conjugate) Green's function.

2.3.2 Backward extrapolation via a full-wavefield inversion

Equation 2.18 shows that the upgoing wavefield P_{0A}^- contains reflection information from the complex area A . The upgoing wavefield P_B^- has experienced complex propagation through area A twice before it arrives at the surface as P_{0B}^- . The Green's functions in Equation 2.19 are no longer one-way but contain multiple-scattering, thus violating the condition under which the Rayleigh integral was derived in the previous sections. The only way to calculate P_B^- at the datum z_A from P_{0B}^- at z_0 is by inverting for the true-amplitude full-waveform transmission operator from z_A to z_0 . Once obtained, these transmission operators can then be inverted and applied for true-amplitude imaging to retrieve the wavefield P_B^- .

Figure 2.5 shows the total observed upgoing wavefield P_0^- that consists of upgoing wavefield P_{0A}^- and P_{0B}^- responses from area A and B respectively, where S^+ is a bandlimited incident source wavefield. Wavefield P_B^- is the upgoing wavefield resulting from illumination of area B by the incident source wavefield that has been propagating through the complex area A . Higher-order scattering between the areas A and B whereby area B is again illuminated by $P_{B_{sct}}^+$, is ignored.

2.4 General representation of seismic data

2.4.1 Discrete matrix notation

We use the discrete data matrix representation of reflection data (Berkhout, 1982), where the frequency dependency (ω) is suppressed for notational conveniences. Capital quantities in the equations represent vectors and **bold** quantities denote matrices in the frequency domain. The sampling of a wavefield $p(\vec{x}_r, \vec{x}_s; t, z_0)$ in 3D measurements consist of five discrete coordinate components:

1. shot location of $\vec{x}_s = (x_s, y_s; z_0)$;
2. receiver location of $\vec{x}_r = (x_r, y_r; z_0)$;
3. time t .

with z_0 is the vertical location of the acquisition surface. Applying a temporal Fourier transform $p(\vec{x}_r, \vec{x}_s; t, z_0)$ converts the data to the frequency domain $P(\vec{x}_r, \vec{x}_s; \omega, z_0)$. The wavefield P can then be arranged in a convenient matrix form such that a horizontal slice of the matrix contains all shot-receiver responses for a single frequency. The organization is such that the diagonal elements of each slice represent the zero-offset measurements for a single frequency component.

The matrix structure is illustrated in Figure 2.6a for a 2D case of three shot records measured at different surface locations; the blue box shows the locations of the three shots (x_s) and receiver locations (x_r). One column of the frequency slice shown in Figure 2.6d represents one shot gather, and one row represents one common-receiver gather. In general, we assumed that the data are recorded by N shot records with M receiver locations and to make the matrix square, empty trace locations are filled with zero-valued traces.

In both land and marine seismic acquisition, the zero and short-offset traces (near diagonal elements of the matrix) are not recorded and in marine seismic acquisition with a towed-spread, only the upper half of the diagonal matrix is filled. To fill the lower half of the matrix, we use the reciprocity theorem. This is done by interchanging sources and receivers as shown in Figure 2.7 so that the data are mirrored along the main diagonal. The near offsets can then be interpolated (Kabir and Verschuur, 1995). It should be noted that the reciprocity theorem can only be used after the source and the receiver directivity effects due to the source and the receiver patterns are removed.

2.4.2 WRW representation

We next describe the **WRW** representation. This representation of seismic experiments both makes the matrix notation convenient and makes the numerical implementation of wavefield propagation straightforward. The **WRW** notation also elegantly combines wave propagation

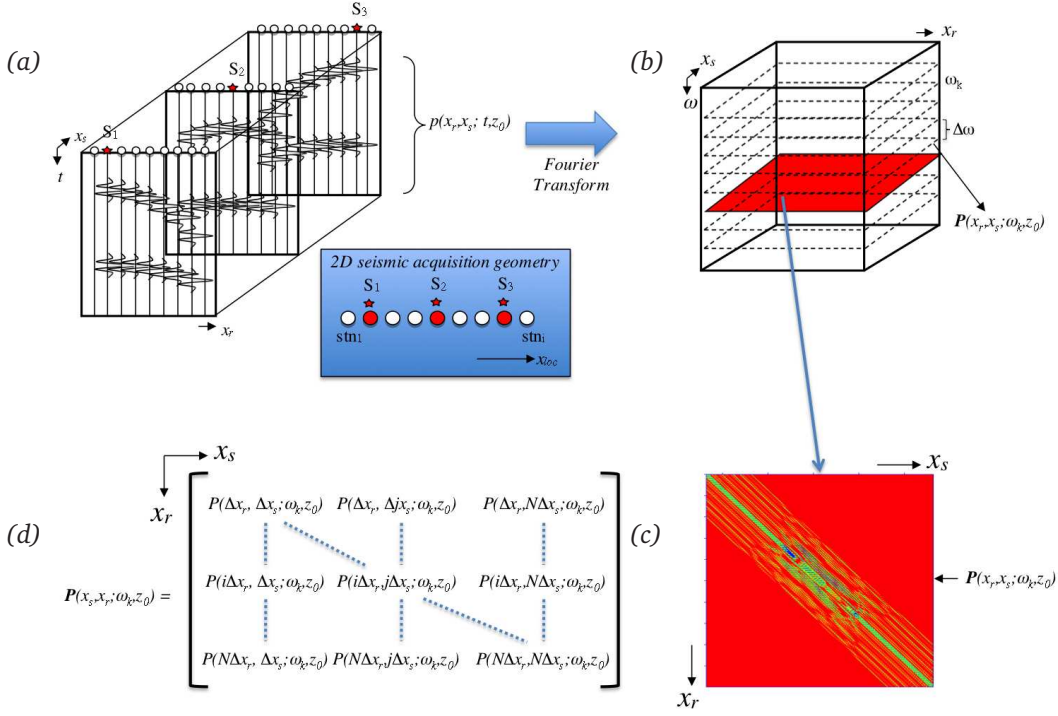


Figure 2.6 (a) Time-domain shot records of a 2D seismic acquisition is notated as $p(x_r, x_s; t, z_0)$. The blue box shows the source locations (x_s) together with the receiver locations (x_r). (b) Fourier transform of the data in (a). The red square represents one slice for a single frequency component. (c) Amplitudes corresponding to one frequency slice from the synthetic data. Distortion seen in the middle zone is due to a shallow gas cloud. (d) The prestack data in matrix form for one frequency component.

and the reflection response. The matrix-vector multiplications mean that the application of an operator to a wavefield is equivalent to a spatial convolution.

The representation of the scattered wavefield in 2D or 3D for seismic data from reflectors at all depth levels can be written in a discrete matrix notation representation as:

$$\mathbf{P}(z_0, z_0) = \mathbf{D}(z_0, z_0) \sum_{d=1, \dots, m} \mathbf{W}^-(z_0, z_d) \mathbf{R}(z_d, z_d) \mathbf{W}^+(z_d, z_0) \mathbf{S}(z_0, z_0), \quad (2.20)$$

where \mathbf{P} is the recorded wavefield at the surface, \mathbf{S} is the source matrix, \mathbf{W}^+ and \mathbf{W}^- are the propagation matrices, $\mathbf{R}(z_d, z_d)$ is the angle dependent reflectivity matrix at depth z_d and \mathbf{D} is the detector matrix. Equation 2.20 describes the seismic experiment where the observed wavefield at the acquisition surface is the result of four spatial convolutions per frequency component, for each depth level z_d .

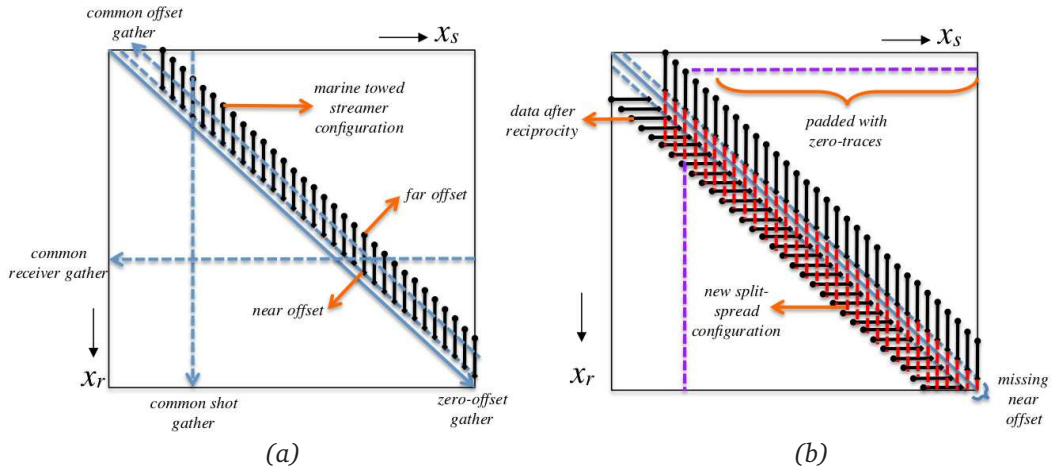


Figure 2.7 (a) Schematic diagram of the acquired marine towed-streamer configuration where the solid blue line is the zero-offset location and the blue dashed line is the offset location of the first receiver. (b) New split-spread configuration set-up obtained by manipulating acquisition geometry coordinates from the towed-streamer configuration in (a) combined with the data from reciprocity.

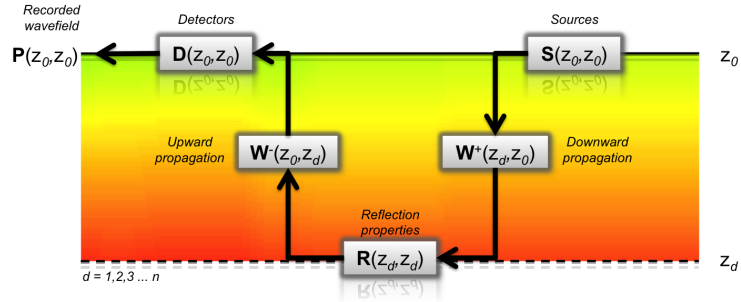


Figure 2.8 A schematic diagram representing seismic acquisition using WRW notation.

We can also write:

$$\mathbf{P}(z_0, z_0) = \mathbf{D}(z_0, z_0)\mathbf{X}(z_0, z_0)\mathbf{S}(z_0, z_0), \quad (2.21)$$

where

$$\mathbf{X}(z_0, z_0) = \sum_d \mathbf{W}^-(z_0, z_d)\mathbf{R}(z_d, z_d)\mathbf{W}^+(z_d, z_0) + \mathbf{M}_{int}(z_0, z_0), \quad (2.22)$$

where $\mathbf{M}_{int}(z_0, z_0)$ means the internal multiples as recorded at the acquisition surface.

In theory, \mathbf{M}_{int} can be expressed in terms of \mathbf{W} 's and \mathbf{R} 's via feedback systems (see Berkhout, 1982) but we will not explicitly use this in our method.

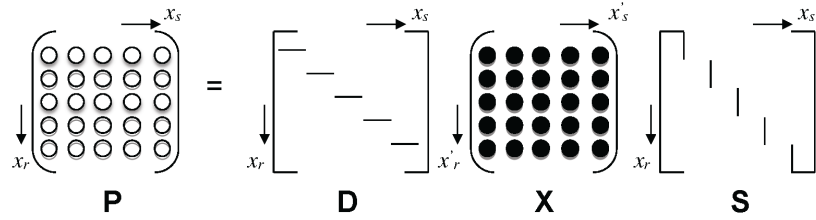


Figure 2.9 Representation of a seismic experiment in matrix notation where \mathbf{P} is the recorded wavefield at the surface, \mathbf{S} is the source matrix, \mathbf{X} is the response or the transfer function of the subsurface and \mathbf{D} is the detector matrix.

We generalized the expression Equation 2.20 to Equation 2.21, such that \mathbf{WRW} in Equation 2.20 becomes \mathbf{X} (Equation 2.22), corresponding to the reflection impulse response of the subsurface. \mathbf{W}^+ can represent all downgoing energy, including short period multiple scattering in the complex area. Similarly, \mathbf{W}^- could include multiple scattering during upward propagation. It is assumed that the total data \mathbf{P} measured at the surface $z = z_0$ is free from surface-related multiples, and that they have been removed in an earlier preprocessing stage (see e.g. Verschuur et al., 1992). This means that the transfer function \mathbf{X} is also free of surface-related multiples but still includes internal multiples. Note that what is usually referred to as the ‘coda’ is included in the \mathbf{W}^+ and \mathbf{W}^- , whereas the long period multiples are contained in \mathbf{M}_{int} .

3

Inversion strategy for gas clouds

Conventional seismic imaging processes do not offer satisfactory solutions for the case of a gas cloud overlaying a target area. Due to the complex wave propagation through the anomaly and the resulting transmission imprint on the reflections from below this area, the image below the gas cloud is usually not properly recovered. The proposed inversion method aims at a solution beyond traditional imaging approaches. The main idea is that the reflection response of the complex area, (i.e. the response of the gas cloud including its coda), carries detailed information on the gas cloud properties that can be obtained and translated into a transmission-correction operator. We aim at constructing full-waveform transmission operators (including the codas) from the gas cloud reflection response via an effective-medium representation, obtained via full-waveform inversion. Next, true-amplitude imaging of reflections below the gas cloud is achieved via multidimensional deconvolution for these full-waveform transmission operators.

3.1 Proposed inversion strategy

3.1.1 Forward model

The forward model for 2D or 3D seismic measurements can be written as (see Chapter 2.4):

$$\mathbf{P}(z_0, z_0) = \mathbf{D}(z_0, z_0)\mathbf{X}(z_0, z_0)\mathbf{S}(z_0, z_0). \quad (3.1)$$

The multidimensional total reflection response \mathbf{P} can be described by a spatial convolution of the subsurface impulse responses, expressed in matrix \mathbf{X} , with the source properties described by \mathbf{S} and the detector properties in \mathbf{D} .

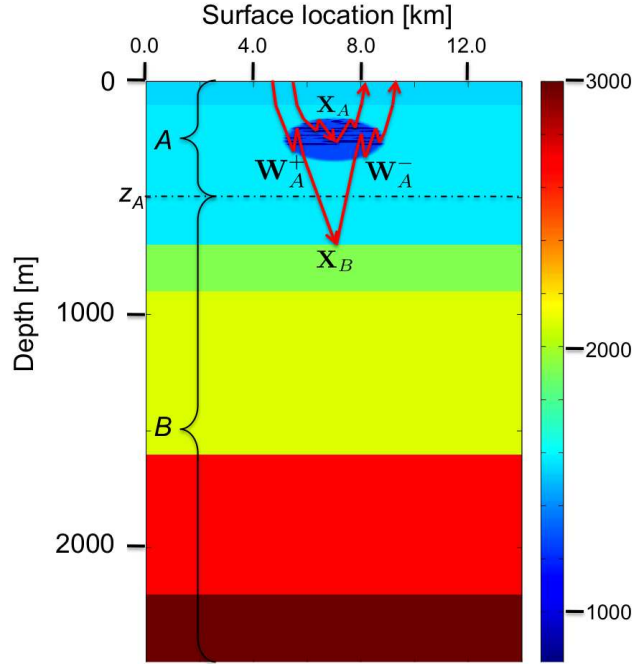


Figure 3.1 Subdivision of the subsurface into a zone A that contains the gas cloud and a zone B with the target horizons. Zone A and B are connected at an arbitrary depth level z_A .

Next, we refine the forward model by subdividing the subsurface into two areas, A and B , as shown in Figure 3.1. The overburden with the gas cloud is called area A and area B denotes the area underneath area A containing the target reflectors. Our aim is to have a true-amplitude image of the reflectors in area B . The choice of the exact location of level z_A between the two areas is somewhat arbitrary. With this modification, the forward model of seismic data can be formulated as:

$$\begin{aligned} \mathbf{P}(z_0, z_0) &= \mathbf{D}(z_0, z_0) [\mathbf{X}_A(z_0, z_0) \\ &+ \mathbf{W}_A^-(z_0, z_A) \mathbf{X}_B(z_A, z_A) \mathbf{W}_A^+(z_A, z_0) + \mathbf{N}(z_0, z_0)] \mathbf{S}(z_0, z_0). \end{aligned} \quad (3.2)$$

The multidimensional total reflection response \mathbf{P} now contains the impulse responses from areas A and B , expressed in matrices \mathbf{X}_A and \mathbf{X}_B respectively. Note that response \mathbf{X}_B is defined as an experiment with unit sources and unit receivers located at depth level z_A . \mathbf{W}_A^+

and \mathbf{W}_A^- represent the one-way propagation through the overburden (zone A in Figure 3.1), i.e. the full-waveform transmission operators. The superscripts '+' and '-' denote downward- and upward-propagating wavefields, respectively, with the z-axis pointing downward. We assume that there are no anelastic losses due to the conversion of the seismic energy into heat. Note that fine-layering propagation and transmission effects are incorporated in operators \mathbf{X}_A , \mathbf{W}_A^+ and \mathbf{W}_A^- including all internal multiple scattering within area A. Finally, \mathbf{N} , the noise, represents elements in the recording that are not described by this model, such as the direct wave and the multiple reflections between zones A and zone B. For the following, we will assume that the receiver properties and the source directivity effects have been removed in advance from the data, hence:

$$\mathbf{D} = \mathbf{I}, \quad \mathbf{S}^+(z_0) = \mathbf{I}S(\omega), \quad (3.3)$$

where \mathbf{I} is the identity matrix and $S(\omega)$ is the source spectrum of the assume dipole sources. Finally, we assume that there are no surface-related multiples in the data. With these simplifications, and neglecting the noise, the forward model becomes:

$$\mathbf{P}(z_0, z_0) - \mathbf{P}_A(z_0, z_0) = \mathbf{W}_A^-(z_0, z_A)\mathbf{X}_B(z_A, z_A)\mathbf{W}_A^+(z_A, z_0)S(\omega). \quad (3.4)$$

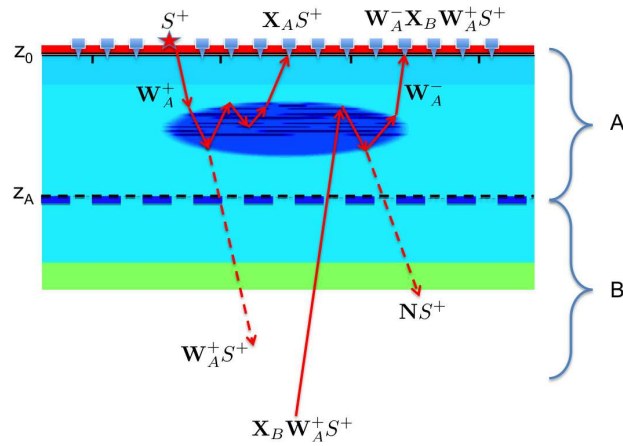


Figure 3.2 The total observed upgoing wavefield \mathbf{P} consists of the upgoing wavefields $\mathbf{X}_A \mathbf{S}^+$ and $\mathbf{W}_A^- \mathbf{X}_B \mathbf{W}_A^+ \mathbf{S}^+$, which are respectively the response from area A and B, \mathbf{S}^+ is a bandlimited source wavelet. Wavefield $\mathbf{W}_A^+ \mathbf{S}^+$ is the downgoing wavefield acting as a secondary source illuminating the subsurface in area B.

with $\mathbf{P}_A(z_0, z_0)$ the reflection response of area A :

$$\mathbf{P}_A(z_0, z_0) = \mathbf{X}_A(z_0, z_0)S(\omega). \quad (3.5)$$

As discussed in Chapter 2.3, in particular in Figure 2.5, the total observed upgoing wavefield \mathbf{P} consists of upgoing wavefield $\mathbf{X}_A S^+$ and $\mathbf{W}_A^- \mathbf{X}_B \mathbf{W}_A^+ S^+$, which are the responses from area A and B respectively, and S^+ is a bandlimited source wavelet, as depicted in Figure 3.2. Wavefield $\mathbf{W}_A^+ S^+$ is the downgoing wavefield illuminating the subsurface in area B . Here the reflection response from area B (\mathbf{X}_B) experienced twice the complex propagation through overburden in area A . Higher order scattering wavefields between area A and B as denoted by $\mathbf{N}S^+$, such as the internal multiples between the base of the gas body with reflections from area B will not be considered in our inversion approach. They can be removed from the data in a separate preprocessing steps (Berkhout and Verschuur, 2005).

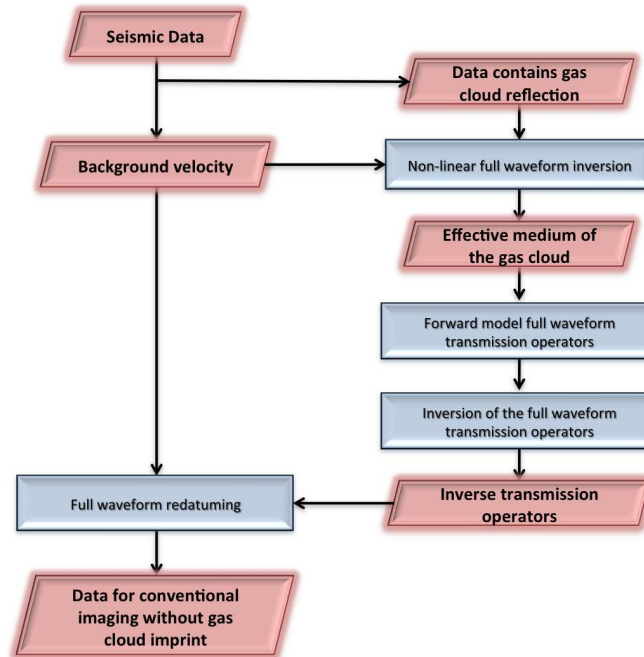


Figure 3.3 Proposed gas cloud imaging, inversion and redatuming strategy.

3.1.2 Inversion strategy

Equations 3.4 and 3.5 form the basis of our true-amplitude imaging strategy. The major issue is the estimation of the transmission operators $\hat{\mathbf{W}}_A^+$ and $\hat{\mathbf{W}}_A^-$, to be applied in a deconvolution process to the data. The total strategy, shown in Figure 3.3, contains the following steps:

- i. Obtain the optimum background velocity model using state-of-the art migration-velocity-analysis (MVA). One way to obtain such a model is by estimating the one-way focusing operators from the seismic data for a reflection event from above and below the gas cloud (Ghazali et al., 2008; see also Appendix A);
- ii. Perform a local nonlinear full-waveform inversion of the reflection response from the gas cloud to obtain an effective property model of the gas cloud area;
- iii. Use this effective model to calculate the true-amplitude, full-waveform transmission operators for propagation through the gas cloud;
- iv. Use these transmission operators in a multidimensional deconvolution process to obtain the true-amplitude response for the reflections below the gas cloud. This in fact is a true-amplitude redatuming process.
- v. Apply conventional imaging to this fully redatumed dataset, from which the overburden imprint has been removed.

3.1.3 Estimation of transmission operator $\hat{\mathbf{W}}_A$ and data application

The most crucial parts of this proposed strategy are in step (ii) to obtain an effective property model of the gas cloud from the reflection response \mathbf{P}_A and step (iii) to obtain $\hat{\mathbf{W}}_A$ from this effective model. For this we first need to isolate the reflection response from the top part, \mathbf{P}_A , from the total response \mathbf{P} . Then, the reflection response of the gas cloud area together with its background velocity model is used as an input for a nonlinear full-waveform inversion in order to estimate equivalent-medium parameters. Nonlinear inversion processes, such as described by Abubakar et al. (2005) and Lam et al. (2007), will image contrasts with respect to the background velocity model, obtained in step (i). In Chapter 4 we discuss in detail our nonlinear full-waveform inversion method which uses a Genetic Algorithm strategy to estimate these effective properties.

Once equivalent-medium parameters have been estimated that adequately describe the reflection response of the gas cloud area, we forward model the transmission operators, and these can then be used as a multidimensional deconvolution operators for the total reflection data. Each matrix inversion is performed using a stabilized least-squares method:

$$\hat{\mathbf{W}}_A^{-1} = [\mathbf{W}_A^H \mathbf{W}_A + \epsilon^2 \mathbf{I}]^{-1} \mathbf{W}_A^H, \quad (3.6)$$

where the superscript H is the Hermitian operator and denotes transposition and complex conjugation, and ϵ^2 is the signal-to-noise ratio for each temporal frequency component, and acts as the prewhitening stabilization. Note again that all calculations are performed in the frequency domain.

Note that Frijlink (2007) also applied a similar deconvolution type of redatuming, although the calculation of the inverse propagation operators was done using a series expansion.

Before deconvolution, \mathbf{P}_A needs to be muted from the input data, since it will be mapped at negative times. After the transmission operators are inverted, the relative true-amplitude response $\hat{\mathbf{X}}_B S(\omega)$ of zone B underneath the gas cloud can be recovered via application of the inverted transmission operators:

$$\hat{\mathbf{X}}_B S(\omega) = [\hat{\mathbf{W}}_A^-]^{-1} [\mathbf{P} - \mathbf{X}_A S(\omega)] [\hat{\mathbf{W}}_A^+]^{-1}. \quad (3.7)$$

After this true-amplitude full-waveform redatuming process, the redatumed response $\hat{\mathbf{X}}_B S(\omega)$ is corrected for both the kinematic and dynamic imprint from the overburden. Conventional imaging can then easily be applied to the redatumed data.

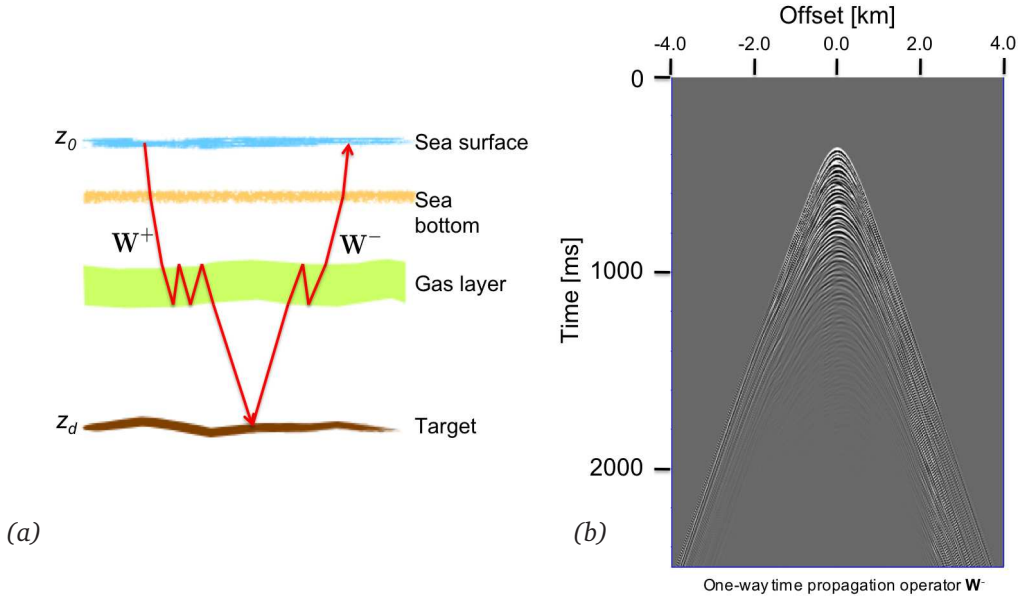


Figure 3.4 (a) Full-waveform transmission operator \mathbf{W} consisting (i) the multiple-reflection impulse response between the seabottom and gas layers; (ii) multiple reflections in the gas layers and (iii) multiples between the target and gas layers and later recorded at the surface (b) Example of a one-way time propagation operator \mathbf{W}^- where the source is placed at the surface and the receivers are at a certain datum depth level z_d .

Figure 3.4 shows the full-waveform transmission operator for one source location and a horizontal reflector below the gas layer in Figure 3.4a. Note the strong coda effect.

3.1.4 1.5D Formulation

To investigate the feasibility of the deconvolution approach, we will first restrict ourselves to the 1.5D case, meaning that we will assume that the earth has properties that only vary as a function of depth, i.e. lateral homogeneity. This means that all columns of the data matrices described above will be shifted versions of each other, hence the matrices have a Toeplitz structure. For this situation, all expressions can be reformulated in the plane-wave domain because, from Snell's law, all propagation and reflection effects happen in a horizontal ray-parameter-consistent manner .

Thus Equation (3.4) can be rewritten as:

$$P(\omega, p_x; z_0) - P_A(\omega, p_x; z_0) = W_A^-(\omega, p_x; z_0, z_A) X_B(\omega, p_x; z_A, z_A) W_A^+(\omega, p_x; z_A, z_0) S(\omega), \quad (3.8)$$

where all quantities are now only a function of frequency (ω) and horizontal slowness (p_x). After estimating the transmission operators for propagation down and up through area A , $\hat{W}_A^+(\omega, p_x; z_A, z_0)$ and $\hat{W}_A^-(\omega, p_x; z_0, z_A)$, the recovered response of area B is obtained via:

$$\hat{X}_B(\omega, p_x; z_A, z_A) S(\omega) = [\hat{W}_A^-(\omega, p_x; z_0, z_A)]^{-1} [P(\omega, p_x; z_0) - P_A(\omega, p_x; z_0)] [\hat{W}_A^+(\omega, p_x; z_A, z_0)]^{-1}, \quad (3.9)$$

where each inverse transmission-operator is obtained via a damped scalar least-squares inversion in the ray-parameter-frequency domain, similar to Equation (3.6).

To show the impact of a complex overburden on a target response, we carry out a forward modeling exercise in the horizontal plane-wave domain (i.e. a 2D wavefield in a 1D medium). Figure 3.5a shows the velocity and density log of the complete model in Figure 3.1, and Figure 3.5b displays the total reflection response as a result of a full-waveform modeling. The arrows in Figure 3.5b indicate the four target reflections below the gas cloud. Note the strong imprint of the gas cloud on this response. Although the arrows in Figure 3.5a show a high acoustic-impedance contrast on the logs, the corresponding reflection amplitudes are low, due to multiple scattering in the gas cloud. The first part of this response is related to the overburden and can be used as input for an inversion process to estimate the effective medium (see Chapter 5). Figure 3.5c shows the reflection response from area X_B without the overburden anomaly similar to the data acquired at the datum z_A . If we compare Figure 3.5b and Figure 3.5c, we can see that the amplitudes of the actual reflections are lower in Figure 3.5b since the gas cloud acts as a stratigraphic filter.

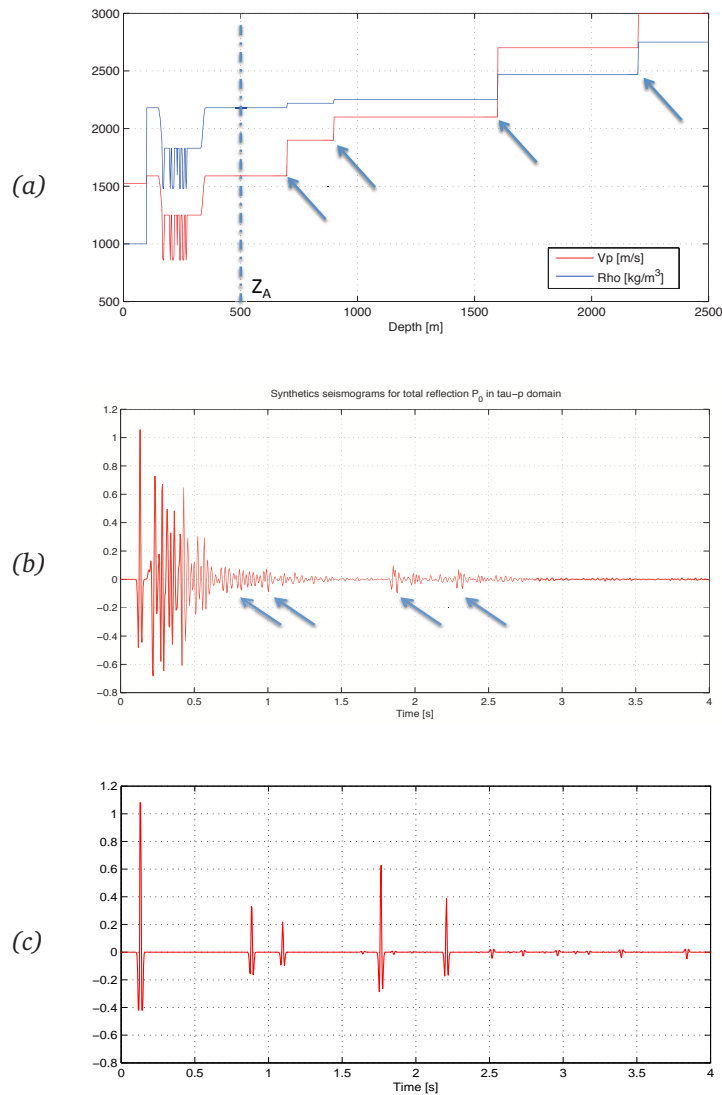


Figure 3.5 (a) 1D Model velocity and density logs. This correspond to values in the middle vertical cross-section of the model in Figure 3.1. (b) The resulting total full-waveform response. The arrows point at the four target reflections below the gas cloud. Note the strong imprint of the gas cloud on this response. Though it has a high acoustic-impedance contrast as shown in Figure 3.5a, the reflection amplitudes for these reflectors are small (indicated by the arrows in Figure 3.5b). (c) Reflection response for the situation without the gas cloud anomaly in the model.

3.1.5 Energy-flux based approach

For the 1.5D case the transmission operators can also be directly obtained from the reflection response, based on the energy-flux conservation (Wapenaar et al., 2004).

This is expressed in our notation where both reflection and transmission responses X_A and W_A are as without the free surface multiples and the symbol (*) denotes complex conjugation:

$$[W_A(\omega, p_x; z_A, z_0)]^* W_A(\omega, p_x; z_A, z_0) = 1 - [X_A(\omega, p_x; z_A, z_0)]^* X_A(\omega, p_x; z_A, z_0), \quad (3.10)$$

For the 2D case, using the matrix notation expression, this reads:

$$[\mathbf{W}_A]^H \mathbf{W}_A = \mathbf{I} - [\mathbf{X}_A]^H \mathbf{X}_A, \quad (3.11)$$

where \mathbf{I} is the identity matrix and H is the adjoint operator or Hermitian. \mathbf{W}_A denotes the transmitted data through the medium A and \mathbf{X}_A describes the reflected data.

Although Equation 3.11 is exact (except that the evanescent waves are ignored), from this expression propagation operators \mathbf{W}_A cannot be uniquely derived for the case of laterally varying media (Thorbecke and Wapenaar, 2006). However, the inversion approach presented in this thesis allows a generalization to both 2D and 3D.

4

Nonlinear inversion for effective media

The next major task is to invert the gas cloud reflection response from area A (see Figure 3.1) for its effective-medium parameters using a nonlinear full-waveform inversion method. For low-contrast inhomogeneous media, we can use a linear inversion method that only considers primary reflections. In the case of heterogeneous media, this results in strong nonlinearities (multiple-scattering) when inverting the observed reflection data containing the gas-cloud reflection response including its internal multiples (coda). We therefore choose to perform the inversion using a Genetic Algorithm (*GA*). This nonlinear inversion process can determine the model parameters velocity and density. Incorporating a frequency-marching strategy (see Chapter 4.2.2) and the best possible starting velocity and density models for the inversion reduces the possibility of being trapped in a local minimum. Major modifications were done on the conventional *GA* especially to obtain a faster convergence. These modifications will be explained later. In this chapter, we encompass the nonlinear inversion theory using a *GA* and describe the implementation for both the 1.5D and 2D cases.

4.1 Genetic Algorithms

A genetic algorithm is a nonlinear global optimization scheme (see e.g. Gallagher et al., 1991; Sen and Stoffa, 1991b; Sambridge and Drijkoningen, 1992; Gallagher and Sambridge, 1994; Mallick, 1995; McCormack et al., 1999). It uses ensemble of ‘chromosomes’ or parameter vectors, each representing a model, called realization; and an ensemble of realizations is called population. By encoding the model parameters into chromosomes, a *GA* manipulates

the chromosomes by several sub-processes for a guided search to obtain a new chromosome that has the ‘fittest’ optimal solution. This guided search is controlled by a random process that tries to mimic a natural selection process in order to search for a global minimum or maximum for an objective function.

The terms populations, realizations and parameters used in this thesis are defined as follows: the parameters (velocity and density values) are the components of one realization whereas a realization is one of the possible solutions within a population. To keep a healthy diversity of a genetic race and to ensure that we sample almost all possible solutions in a solution space, the *GA* must have one or more populations that typically consist of several hundreds of realizations that contain multiparameter elements.

The common *GA* process is based on the evolution of one or more populations of possible solutions to the posed inversion problem and can be described by a repeated application of subprocesses, namely:

1. calculating the value of the objective function for each realization;
2. the mating process between realizations within the population;
3. mutation of some parameters;
4. crossover between populations (in the case where more than one population is used) and;
5. update of the population.

One advantage of a *GA* is that it allows the straightforward implementation without the need to differentiate the objective function in order to find a gradient. Another advantage of a *GA* is its ability to sample a larger solution space without the need for accurate initial models. In addition, the mutation process helps avoid convergence to local minima, thus increasing the chance of finding a global minimum. Major disadvantages of *GA* are its slower convergence and difficulty in finding the exact minimum. The proposed 2D inversion may also become inefficient especially because of the cost of forward-modelling each realization using a finite-difference algorithm. The *GA* software is written in parallel computing to ensure that the sampling in the solution space required by the *GA* is adequate and fast.

Other nonlinear inversion techniques that might be used to estimate the effective medium include the contrast-source inversion method based on the scattering integral (see Abubakar et al., 2005; Lam et al., 2007), gradient methods (Pratt, 1999; Shipp and Singh, 2002; Sirgue and Pratt, 2004; Sears et al., 2008) or simulated annealing (see Sen and Stoffa, 1991a; Sen and Stoffa, 1991b). Sirgue et al. (2010) showed that the velocity model produced by full-waveform inversion can provide a better geologic model and superior one-way wave-equation migrated images.

4.1.1 GA definitions

A single parameter set consists of a total of N velocity (v) and N density (ρ) parameters arranged in vector form for a 1D situation and in matrix form for a 2D case. Although each parameter set is arranged in a matrix, the velocity and density parameters are independent of each other in the sense that they are not related genetically to each other. Each parameter is allowed to have offspring, mutate and crossover independently across the realizations and populations.

For a 2D situation, the matrix elements can be expressed as follows:

- $2N$ parameters per realization;
- M number of realizations per population;
- K number of populations.

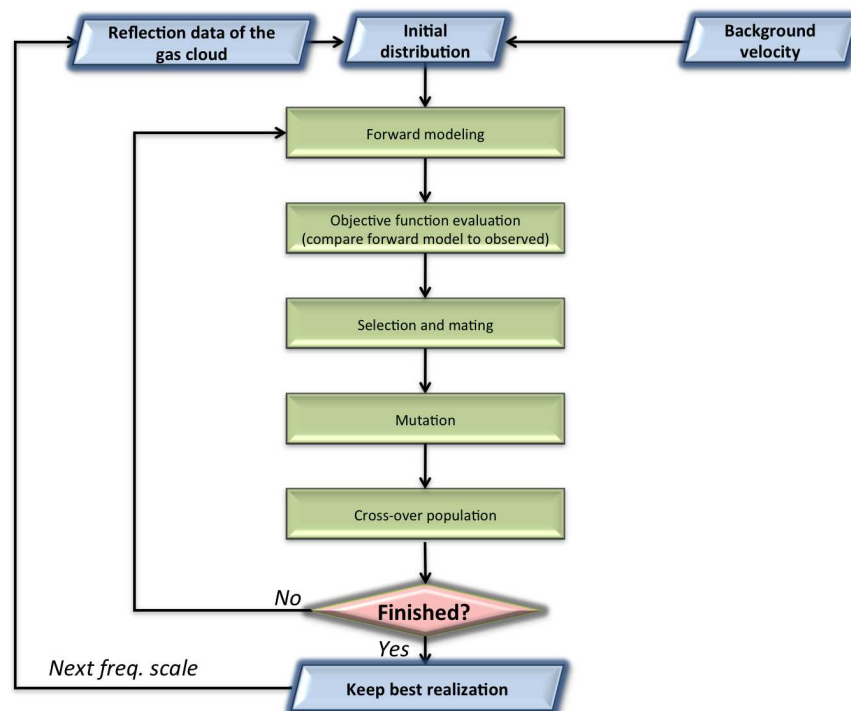


Figure 4.1 The basic Genetic Algorithm workflow for gas-cloud inversion problem.

The total number of parameter samples is therefore $2 \times N \times M \times K$ elements for each iteration for both independent velocity and density parameters. The basic Genetic Algorithm work flow is shown in Figure 4.1. The details of this scheme will be described in the following sections.

4.1.2 Initial parameters

The first step of *GA* inversion is to produce one or more populations that are based on random-selection. A uniform probability distribution function is used for the gas cloud properties including the possible fluid and the background rock matrix properties. A number of initial realizations are constructed by adding a random variation around the background model for both velocity and density. Note that for our numerical experiments we assumed the background model outside the gas cloud is known.

4.1.3 Objective function

One of the biggest advantages of a *GA* is its ability to implement any objective function and penalties without having to differentiate the objective function to get a gradient. Once the different realizations within each population have been obtained, the next step is to forward-model synthetic seismic data for each realization and match them to the observed data. For each realization the objective function value is calculated and then used as the driving force for subsequent *GA* iterations.

The objective function for the *GA* used here is expressed as:

$$\mathcal{J} = \sqrt{\left\{ \frac{\sum_{x,t} [p_A(x,t) - \hat{p}_A(x,t)]^2}{\sum_{x,t} p_A^2(x,t)} \right\}}, \quad (4.1)$$

and is equal to the normalized root-mean-square (RMS) difference of the forward-modeled reflection response $\hat{p}_A(x,t)$ and the observed reflection response $p_A(x,t)$. During the *GA*, this objective function is minimized. Note that for the 1.5D case, the reflection response is a function of ray-parameter (p_x) rather than lateral location x .

4.1.4 Mating

The so-called ‘mating’ process is carried out independently within each population. Random realizations are selected two-by-two and from each selected pair of realizations so that two new realizations are constructed via a crossover process at a random crossover point. This crossover point defines which part of the two selected parameter sets will be mutually exchanged.

In order to ensure that the new generation of parameter sets always has a better objective function value than the previous one, the chance of being selected for the mating process is dependent on this value: the better the objective function value, the higher the chance of being selected. Thus, certain realizations with a good objective function value will be selected several times for a crossover process, whereas some realizations with a poor value will never be selected (‘survival of the fittest’). However, some randomness in this selection

process is still included. For a selected realization, first the relative objective-function fitness value ξ is determined:

$$\xi = \frac{\mathcal{J}_{rel} - \min(\mathcal{J}_{pop})}{\max(\mathcal{J}_{pop}) - \min(\mathcal{J}_{pop})}, \quad (4.2)$$

where \mathcal{J}_{rel} represents the fitness value of the selected realization and in which the $\min(\mathcal{J}_{pop})$ and $\max(\mathcal{J}_{pop})$ represent the best and worst objective function value in the population. Realizations with a small ξ have a higher chance of being selected this is because the selection criterion is that $\xi \cdot rand < \epsilon$, where $rand$ is a random number between 0 and 1 and ϵ is a selected threshold.

Note that the mating process is performed in such a way that the total number of realizations within the populations remains constant.

4.1.5 Mutation

After the mating process, some of the new realizations are mutated for one or more parameters with a specified probability of mutation. Both the selection of the realizations to be mutated as well as the selection of the parameter values are performed via a random processes. This mutation process allows fresh parameter values to enter the population and prevents the *GA* from being trapped in a local minimum. However, excessive mutation rates cause rapid and drastic changes of the population members and give a smaller chance of converging to the correct solution.

4.1.6 Population crossover

The final subprocess is the crossover between populations and update of the overall populations for the next generation. Based on a specified probability of crossover, the best parameter set from a randomly chosen population is selected to be transferred to another, randomly-selected population.

Once all four subprocesses are complete, a new generation of model parameters is generated, for each parameter set in this new model space, and forward modeling is carried out to produce synthetic seismic data and the associated objective function values. Next, the mating, the mutation and the population crossover processes are carried out to yield a next generation. These processes continue iteratively until either the best parameter set has an objective function value within a specified acceptance threshold, or a predefined number of iterations is exceeded.

4.2 1.5D implementation

In this section, we describe the *GA* that will be used for inverting the gas cloud response for the 1.5D situation (see Chapter 5.2). For this, the measured response is transformed to the ray-parameter domain $p(\tau, p_x)$, where it is matched with the estimated response. Forward modeling required by the *GA* is performed using the full-waveform Kennett method (Kennett, 1983) in the ray-parameter-frequency ($p_x - \omega$) domain. The data are calculated in the $p_x - \omega$ domain, but are assessed and displayed in the intercept time (τ) and ray-parameter (p_x) domain via an inverse temporal Fourier transform. For our example, the gas cloud is modeled by velocity and density parameters at each vertical step of $2m$. In the *GA* process we use a set of realizations of the velocity and density model which have been subdivided into a few populations. During the *GA* inversion the parameters for each of these realizations is altered continuously to improve the fitness value of the realizations.

4.2.1 1.5D Objective function

The objective function is described by the normalized RMS difference of the forward-modeled and observed reflection responses, both of which are in the τ - p_x domain. The *GA* objective function is augmented with a Cauchy penalty function enforcing blockiness of the velocity and density profiles. The *GA* is stopped either when a predefined number of iterations has been carried out, or when the objective function value of the best parameter set does not improve anymore.

The objective function for the *GA* is expressed as:

$$\mathcal{J} = \sqrt{\left\{ \frac{\left(\sum_{\tau, p_x} [p_A(\tau, p_x) - \hat{p}_A(\tau + \Delta t_m(p_x), p_x)]^2 \right)}{\sum_{\tau, p_x} p_A^2(\tau, p_x)} \right\} + \left(\sum_i \Gamma_i + \sum_i \Psi_i \right)}, \quad (4.3)$$

where $\Delta t_m(p_x)$ is the location of the maximum of the weighted crosscorrelation function Φ between the forward-modeled reflection response $\hat{p}_A = \hat{X}_A * s(t)$ and the observed reflection response p_A :

$$\Phi(\Delta t, p_x) = e^{-\frac{\Delta t^2}{2c^2}} \sum_{\tau} [p_A(\tau + \Delta t, p_x) \cdot \hat{p}_A(\tau, p_x)], \quad (4.4)$$

where c is a suitable constant. Note that the exponential weight function in Equation (4.4) forces Δt_m to be close to zero. The parameter Δt_m is included to relax the objective function in such a way that realizations that have a good match except for an overall time shift are still accepted in the solution space.

The Cauchy penalty functions which enforce sparseness in the model parameter are given by:

$$\Gamma_i = \mu \ln \left[1 + \left(\frac{dc_i/dz}{\beta_c} \right)^2 \right], \quad (4.5)$$

$$\Psi_i = \mu \ln \left[1 + \left(\frac{d\rho_i/dz}{\beta_\rho} \right)^2 \right], \quad (4.6)$$

where c_i and ρ_i are respectively the propagation velocity and density at the i^{th} depth sample. The scalar parameters μ , β_c and β_ρ in Equations (4.5) and (4.6) provide a blockiness constraint on the solution. The optimum values of these constants depend on the range of the differential values of velocity and density. β_c and β_ρ are chosen such that it provides the desired blockiness and is adjusted such that the total penalty function is about 10% of the expected RMS. Note that currently there is a restriction on both terms being weighted by the same μ . For future research, this restriction can be removed. In our example, $\beta_c = \beta_\rho = 10$ and $\mu = 0.001$. Note that, μ is unitless, unit of β_c is $[1/s]$ and β_ρ is in $[kg/m^4]$.

4.2.2 Frequency marching

We have implemented a multiscale frequency marching inversion strategy for faster convergence of the GA. We start by inverting with the lowest frequency and then extend the bandwidth to higher frequencies. The lower-frequency wavelet is less sensitive to small changes within the overall parameter sets as compared to the higher-frequency wavelet response.

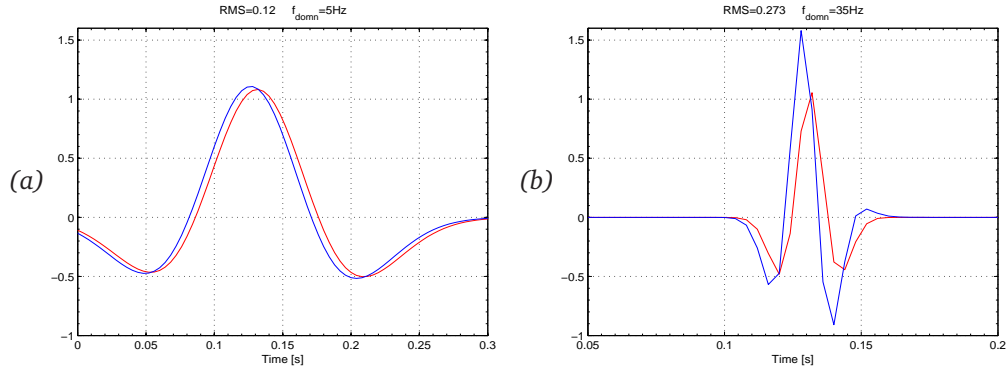


Figure 4.2 Full-waveform reflection modeling with different dominant frequencies. The red line is the full-waveform result for a given model and the blue line is the result after changing two parameter values in this model. Figure 4.2a illustrates that the low-frequency result is less affected by the parameter changes as compared to the higher-frequency result in Figure 4.2b. This relative difference is quantified by the RMS values, which are respectively 0.12 and 0.27.

This is illustrated in Figure 4.2 where only two out of a hundred parameter values are changed for a certain velocity and density realization. Figure 4.2a illustrates that the low-frequency result is less affected by the parameter change compared to the higher-frequency result in Figure 4.2b. This relative difference is quantified by the given RMS values of 0.12 and 0.27, respectively. This demonstrates that the *GA* inversion may have more difficulties resolving errors at high frequencies. By contrast, lower-frequency inversion produces a better background parameter model but lacks resolution. By marching to higher frequencies the algorithm will converge to a more detailed parameter solution.

On the other hand, a higher-frequency wavelet is required to generate the same codas as observed on the seismic data. The parameter model resulting from the lower-frequency inversion serves as an initial model for the next frequency band. Without this frequency-marching strategy, inverting the higher frequencies directly, the *GA* will have difficulties to find the global minimum because it has to search a bigger solution space with many more degrees of freedom.

4.3 2D implementation

In this thesis, we present a multidimensional nonlinear full-waveform inversion approach using an optimized Genetic Algorithm (*GA*) to invert the highly nonlinear gas cloud reflection response for its effective-medium parameters. This nonlinear inversion process is essential for obtaining full-waveform transmission operators (including the codas) from the gas cloud reflection response via an effective-medium representation. However, extending this approach to a 2D nonlinear full-waveform inversion is not simple or straightforward. Furthermore, to simulate the actual seismic wavefield in the subsurface we use the finite-difference method as forward-modeling process; this aggravates the expense of the *GA* inversion procedure.

We demonstrate that multidimensional nonlinear full-waveform inversion using a *GA* is a viable method obtaining effective gas-cloud medium parameters from the gas reflection response. We have optimized the conventional *GA* by implementing several methods in achieving faster convergence. These include blended-acquisition (see Krebs et al., 2009; Blacquièrè et al., 2009), frequency marching, amplitude matching and crosscorrelation in the time domain. We also implemented the evaluation of a local objective function for every shot record. This has the advantage that every shot record illuminates a different part of the subsurface and therefore provides somewhat independent information on the subsurface. The general 2D Genetic Algorithm work flow is shown in Figure 4.3.

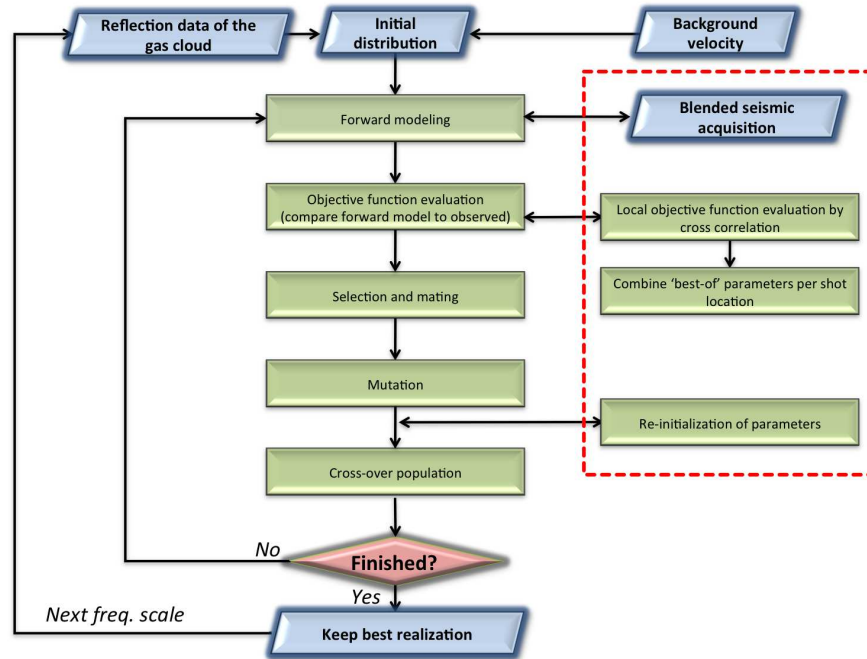


Figure 4.3 General 2D Genetic Algorithm workflow. The red dotted box and the frequency marching indicate enhancements made to optimize the conventional Genetic Algorithm for faster convergence.

4.3.1 Initial 2D GA parameter distribution

In order to perform the 2D Genetic Algorithm in a fast and efficient manner we arrange the parameter sets into a 2D matrix grid structure. Each element described by the indices i and j corresponds respectively to a surface-location x_j [m] and depth z_i [m].

This is depicted in Figure 4.4 which shows the initial models of velocity (v_{ij}) and density (ρ_{ij}) that are input to the GA. Also shown in the figure are examples of surface shot locations with respect to the parameter location. For each parameter element location x_j and z_i , the initial parameter models are perturbed randomly with a certain probability distribution function; the range of values for the distribution is taken from well information.

4.3.2 Adaptive objective function

For the objective function, we use the root-mean-square difference between the modeled data $\hat{p}_A(x,t)$ and observed response $p_A(x,t)$ including an overall scale factor α and time shift Δt . The objective function for the multidimensional nonlinear full-waveform inversion is

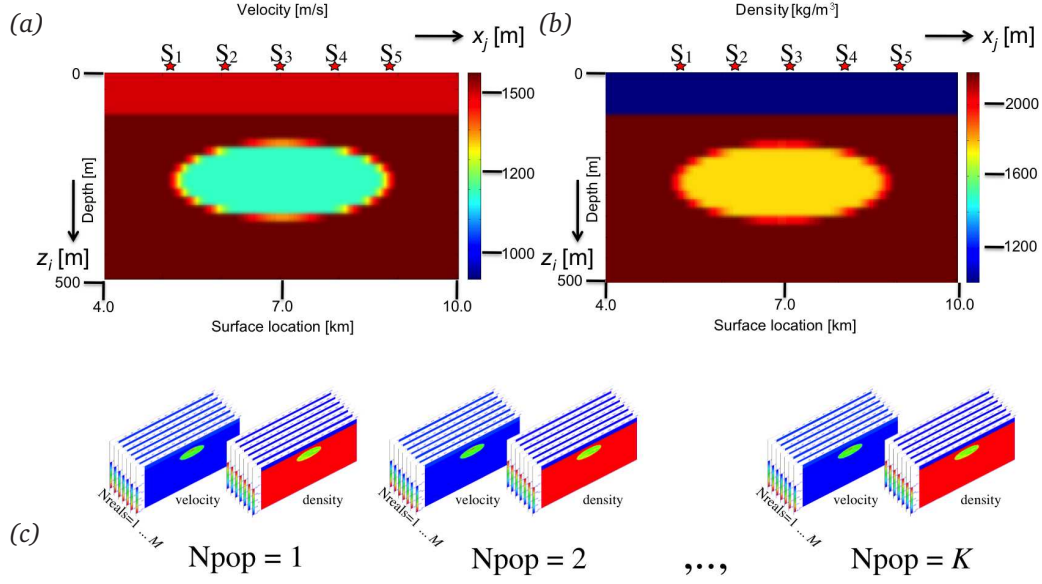


Figure 4.4 (a) Initial distribution of the velocity model [m/s]. S_n are the source locations for five shots. (b) Initial distribution of density model [kg/m³]. (c) Each genetic population contains several hundreds of realizations of velocity and density distribution.

expressed in Equation 4.7 as the minimization of:

$$\mathcal{J} = \sqrt{\left\{ \frac{\sum_{n=1}^{Nshot} \sum_{x,t} (p_{A_n}(x,t) - \alpha_n \hat{p}_{A_n}(x,t + \Delta t_n))^2}{\sum_{n=1}^{Nshot} \sum_{x,t} (p_{A_n}(x,t))^2} \right\}}, \quad (4.7)$$

where \mathcal{J} is the normalized difference between the forward-modeled reflection response $\hat{p}_A(x,t) = \hat{X}_A * s(t)$ and the observed reflection response p_A .

The overall time shift is obtained by searching for the location of corresponding to the Δt_n maximum in the crosscorrelation function of the two datasets for every shot record:

$$\Phi_n(\Delta t) = \sum_{x,t} [p_{A_n}(x,t) \cdot \hat{p}_{A_n}(x,t + \Delta t)], \quad (4.8)$$

The overall amplitude scale factor α_n between the observed and the forward-modeled data for every realization, is given by:

$$\alpha_n = \left[\frac{\sum_{x,t} (p_{A_n}(x,t) \cdot \hat{p}_{A_n}(x,t + \Delta t_n))}{\sum_{x,t} (\hat{p}_{A_n}(x,t + \Delta t_n) \cdot \hat{p}_{A_n}(x,t + \Delta t_n))} \right]. \quad (4.9)$$

4.3.3 Local objective function

Besides the global objective function, we also calculate a local objective function value for each shot. This exploits the fact that each shot illuminates a different part of the subsurface, as illustrated in Figure 4.5a. By selecting the best parameter realizations belonging to the lowest value of the local objective function for each shot, these parameter realizations are then combined in a weighted average manner.

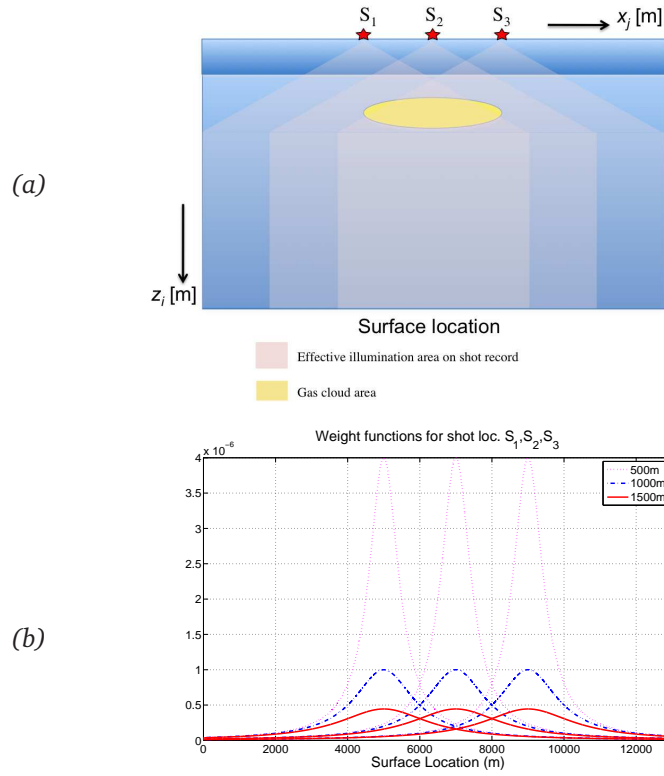


Figure 4.5 Schematic illustration the local GA objective function approach. (a) Part of the illumination area of the subsurface from each shot location. (b) Black, blue and red curves are the weight functions at the j th depth sample for each shot location.

The weighted-average velocities and densities are described by:

$$\bar{v}_{ij} = \frac{\sum_{n=1}^{Nshot} W_{ij}^n v_{ij}^{m_{bp}(n)}}{\sum_{n=1}^{Nshot} W_{ij}^n}, \quad (4.10)$$

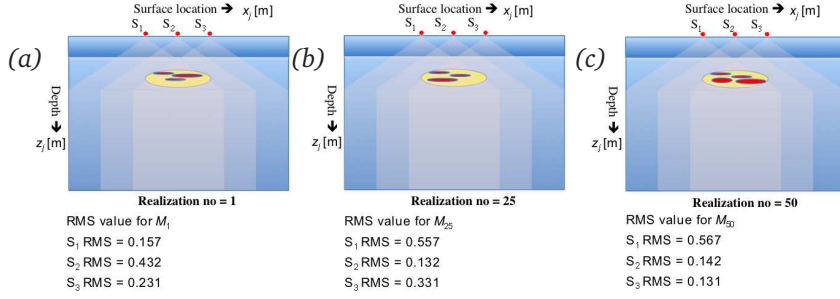


Figure 4.6 Example of using the local objective function values. The realizations (a-c) have the lowest local objective function value for each shot position S_1 , S_2 and S_3 for a certain GA generation. Each parameter from each selected realization is combined in a weighted average manner based on their distance to the shot location.

$$\bar{\rho}_{ij} = \frac{\sum_{n=1}^{Nshot} W_{ij}^n \rho_{ij}^{m_{bp}(n)}}{\sum_{n=1}^{Nshot} W_{ij}^n}. \quad (4.11)$$

with v_{ij} and ρ_{ij} being the velocity and density at the grid point i, j , and n is the shot number where $m_{bp}(n)$ is the best realization with the lowest objective function value as a function of the shot number. The weight function (W) is given by:

$$W_{ij}^n = \frac{\cos\phi_{ij,n}}{r_{ij,n}^2}, \quad (4.12)$$

where r is the distance from grid point i, j to source location n .

Figure 4.5b depicts the weight functions for depth levels at $500m$, $1000m$ and $1500m$, for three shot locations - S_1 , S_2 and S_3 . These weights are a function of the distance between the parameter position, in terms of the lateral position and depth of the parameter (x_j, z_i), with respect to the shot location (S_n). A shot close to the parameter location gets a larger weight than one that is far away.

A numerical example illustrating this approach is shown in Figure 4.6. During each GA generation, the local objective function values are used to create a ‘best-of’ solution, i.e. combining the parameter realizations with the lowest value of the local objective function. This ‘best-of’ parameter set is then copied to the next generation.

Finally, note that our choice of weight function is rather simplistic and can be improved e.g. by incorporating a beam-steering ray tracing weight function process.

4.3.4 Blended acquisition

Blended acquisition is a strategy that was originally introduced to move from the relatively poorly sampled source domain obtained in conventional data acquisition to densely-sampled wide-azimuth source distributions with relatively small time intervals between shots (Berkhout et al., 2008; Berkhout, 2008; Blacquière et al., 2009). It worth noting that in blended acquisition the sources and wavefields overlap in time. In our case, we use blended acquisition in the inversion process for two reasons. The first reason is to reduce turn-around time in forward modeling the shots using the acoustic finite-difference algorithm. Instead of modeling every shot independently, we model the shots simultaneously as a single blended shot record. The other reason is the implicit advantage that using more shots increase the illumination of the subsurface.

We encode the blending operators randomly at each generation of the GA (in similar way to the method proposed by Krebs et al., 2009). This introduces incoherent interference noise during the inversion, but retains a consistent wavefield response from the subsurface. The blending operator consists of encoded time-delays ranging from 0 – 400ms which is controlled by a random process.

Figure 4.7b illustrates the time delays applied to each source wavelet for the finite-difference modeling during each GA iteration.

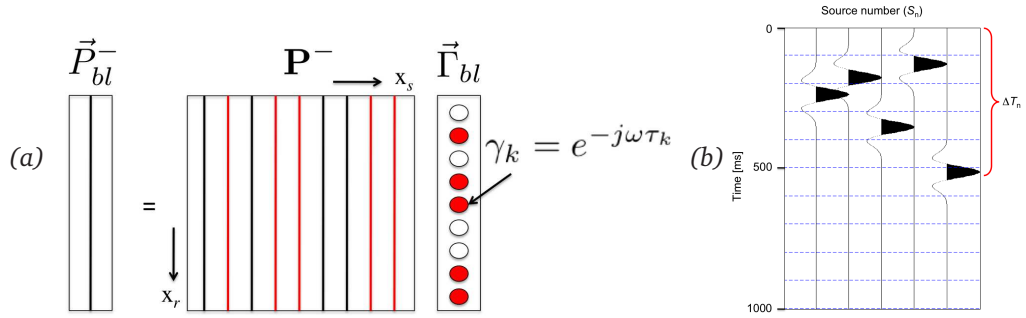


Figure 4.7 (a) \vec{P}_{bl}^- is a vector containing blended shot records. x_s are the surface positions for all the shots and x_r are the receivers positions for the recorded wavefield \mathbf{P}^- . Vector Γ_{bl} contains the randomly-encoded amplitude and time delays γ_k that are generated in the GA inversion. The red colour indicates the shot locations blended with the specific time delays. (b) Blended bandlimited source wavelets S^+ for finite-difference forward modeling in the GA inversion. ΔT_n is a random time delay encoded by GA inversion where subscript ‘n’ denotes the shot number.

Figure 4.7a shows a schematic diagram for the blended acquisition strategy. In this example, one blended shot record \vec{P}_{bl}^- consists of several conventional shot records from the data matrix \mathbf{P}^- . Red lines in the recorded wavefield matrix \mathbf{P}^- show the selected shots, multiplied

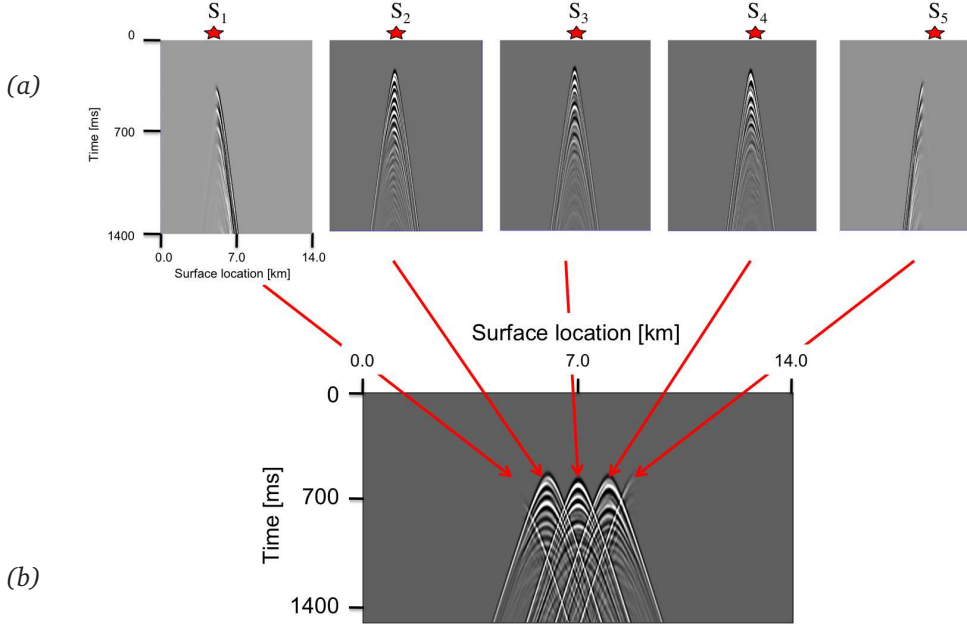


Figure 4.8 (a) Example of individual shot records (\mathbf{P}_n^-) prior to blending. (b) Blended shot record (\vec{P}_{bl}^-).

by the corresponding blending factor γ_k (shown by the red circles). The blended shot record \vec{P}_{bl}^- is the sum of the individual shot records \mathbf{P}_n^- and can be expressed as:

$$\vec{P}_{bl}^- = \mathbf{P}^- \vec{\Gamma}_{bl}, \quad (4.13)$$

where each k^{th} element in the blending operator $\vec{\Gamma}_{bl}$ is the k^{th} shot number location that contains amplitude of 1 and time-delay τ_k . This is encoded by the GA, and it can be expressed as:

$$\gamma_k = e^{-j\omega\tau_k}. \quad (4.14)$$

To calculate the value of the objective function, we blend the observed shot records $p_{A_n}(x, t)$ with the same blending operator γ_k .

It is important to change the blending code with each GA iteration, so that crosstalk does not produce artefacts in the estimated model.

Figure 4.8a shows an example of individual shot records prior to blending, while Figure 4.8b shows the resulting blended shot record encoded by a particular blending operator $\vec{\Gamma}_{bl}$.

It should be noted that the quality of inversion of one blended shot record is not better than inversion of individual shot records. This is because crosstalk produced by the blending process may affect the quality of the inversion result. However, blending helps to make the GA more efficient. Note again that implementation of this blended approach can only

be performed in a fixed-spread acquisition geometry configuration. Encoding the blending operator $\vec{\Gamma}_{bl}$ can also be executed with other encoding methods such as random phase encoding, phase reversal, phase shifting, time shifting, and convolution with random sequences (see Krebs et al., 2009 and Romero et al., 2000).

4.3.5 Other enhancements

Other enhancements that were made to the *GA* to improve the convergence of the process are as follows:

1. Mutating simultaneous blocks of parameters instead of mutating a single value per parameter location. The choice of block length is controlled by a random process.
2. Population reinitialization. In order to introduce fresh genetic information into the system, the best realization is sometimes selected based on the lowest objective function value and a new population is built by adding random variations to this realization. The objective functions of the new population realizations are then evaluated and if a new minimum is found, then corresponding realization replaces the one with the maximum RMS in the original population. This is useful for finding the global minimum in a bigger solution space.
3. A geometrical mask is used to impose certain preassumed stratigraphic shape on the solution space. In our numerical experiment (see Chapter 5.3) we imposed an oval area, within which the gas cloud is assumed to be located.
4. The best parameter realizations for every population K are average to give a new parameter realization which is then inserted as a new realization in one of the populations.

5

Synthetic data examples

In this chapter we conduct feasibility experiments on the gas cloud inversion strategy proposed in Chapter 3, using full-wavefield synthetic data. We start with an experiment for a 1.5D inhomogeneous medium and then continue with a 2D heterogeneous medium. In order to evaluate the viability of the gas cloud inversion strategy, we forward model the transmission operators in the actual medium and apply them as deconvolution operators. This test is carried out before we test the inversion of the effective-medium parameters for both synthetic datasets. For the nonlinear inversion, we use the Genetic Algorithm approach as discussed in Chapter 4. Finally, we perform full-waveform transmission deconvolution with transmission operators modeled in the estimated gas cloud models to achieve true-amplitude redatuming. A statistical analysis is done for the 1.5D example to assess the accuracy needed for the transmission operator estimation to achieve a good full-waveform redatuming result.

5.1 Model description

The 2D heterogeneous model for the 2D experiment was designed to mimic common Malay basin and North Sea characteristics (see e.g. Figure 1.1). Fine layering with shallow fluid-filled high-porosity channel sands are common in both areas, including layering at scales smaller than the seismic wavelength, which produce internal multiples and scattering.

The velocity (v) and density (ρ) of the medium are based on real field values (Table 5.1). Figure 3.5b shows the resulting total 1.5D full-waveform response obtained using Kennett's

Table 5.1 Medium variables in the gas cloud numerical model that are based on Malaysian basins.

n	Layer	v_p [m/s]	ρ [kg/m ³]
1	Water	1500	1000
2	Sediment 1	1590	2180
3	Gas Body	1250	1830
4	Gas Inclusions	860	1830
5	Sediment 2	1900	2220
6	Sediment 3	2100	2253
7	Sediment 4	2700	2470
8	Sediment 5	3000	2750

method. The model does not include any attenuation and any amplitude attenuation observed in the seismic response is therefore due to complex wave propagation. The approach used to obtain this model was pragmatic: by changing the properties within the gas anomaly the modeling results were compared to certain field data and the model that best mimicked the characteristics of the field data was chosen for the study. The wave propagation through this complex heterogeneous overburden creates multiple scattering that in turn produces dispersion and attenuation effects in the deeper reflectors. In addition, the low velocity of the gas causes traveltimes delays.

Figure 5.1a depicts the total velocity model used for numerical modeling and Figure 5.1(b-c) shows the details of the velocity and density geometries inside the gas cloud.

We used a time-shifted zero-phase source signal ($S(\omega)$) with a maximum frequency of 100Hz, the dominant frequency being 35Hz. The source wavelet and its frequency spectrum are shown in Figure 5.2. We model the wavefield (\mathbf{P}) without the free surface multiples. The parameters for the 2D numerical data simulation are shown in Table 5.2.

5.2 1.5D Example

The first synthetic dataset is for a so-called 1.5D inhomogeneous medium, for which there are lateral changes (laterally invariant medium). The data can then be modeled, inverted and deconvolved for each ray-parameter p_x with the data recorded in the full acquisition offset geometry. For the 1.5D model we consider the vertical cross section in the middle of the 2D model in Figure 5.1a. We forward model the data in the $\tau - p_x$ domain with the medium parameters in Table 5.1. We sample the ray-parameter p_x with $\Delta p_x = 1.10^{-05}$ [s/m] with a maximum value of the ray-parameter of $p_x = 6.10^{-04}$ [s/m]. Thus it contains the angle-dependent reflectivity information which is essential for later multidimensional experiments. The GA inversion and full-waveform transmission deconvolution operators \mathbf{W}^{-1} are calculated separately for each ray-parameter p_x .

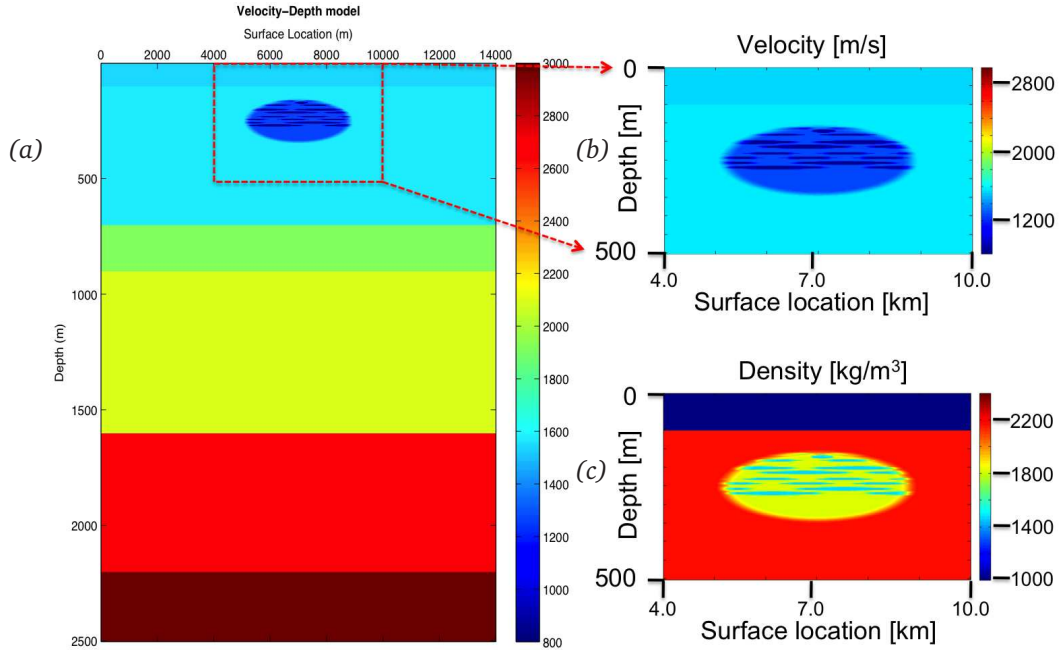


Figure 5.1 (a) Velocity-depth model used for numerical modeling. (b) Zoom of the velocity model in the gas cloud area in (a). (c) The associated density model.

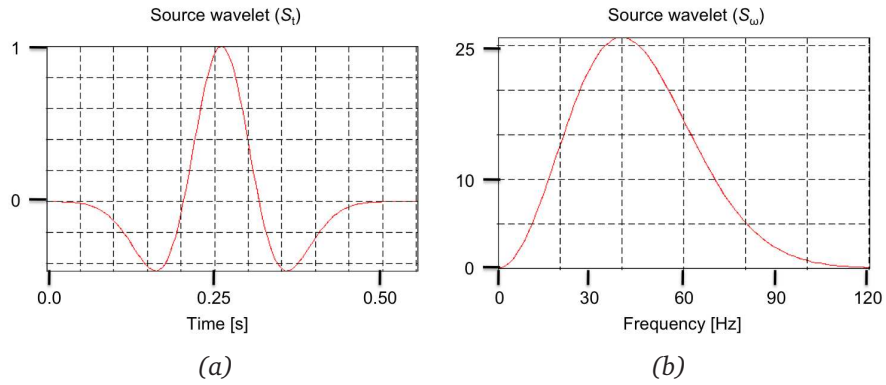


Figure 5.2 (a) Source wavelet (S_t) used for the 2D numerical experiment and (b) its respective frequency spectrum (S_ω).

5.2.1 Deconvolution with true transmission operators

We first demonstrate the proposed strategy with a 1.5D forward-modeling experiment, where we deconvolved the total reflection data \mathbf{P} with the forward-modeled transmission operators,

Table 5.2 Wavefield forward-modeling parameters - via a staggered grid acoustic finite-difference algorithm.

Model boundary	$x[\text{km}] = (0.0, 14.)$ $z[\text{km}] = (0.0, 2.5)$
Modeling grid size [$dx \times dy$]	$2m \times 2m$
Center of gas cloud	$(7.0, 0.225)[\text{km}]$
Gas cloud background lens size	$\Delta x_{max} = 4.0 [\text{km}]$ $\Delta z_{min} = 0.2 [\text{km}]$
Shot spacing	$20m$
Number of shots	701
Receiver spacing	$20m$
Maximum spread-offset per side	$1500m$
Acquisition configuration	Split-spread
Total spread length	$3000m$
Record length	$4s$
Sampling rate	$2ms$
Source type	dipole source
Source signature	Ricker wavelet
Maximum frequency	$120Hz$
Dominant frequency	$40Hz$

obtained from the actual velocity and density model. This is to test the viability of the proposed deconvolution strategy prior to nonlinear full-waveform inversion to obtain equivalent medium parameters. Figure 5.3a shows the total reflection response that was based on the logs shown in Figure 3.5a. Although all modeling and deconvolution steps were carried out in the wavenumber-frequency domain, the results are shown in the time-offset domain.

The exact full-waveform transmission operators through the gas cloud, \mathbf{W}_A^- and \mathbf{W}_A^+ , are displayed in Figure 5.3b and the deconvolved result obtained with these operators is shown in Figure 5.3c. The full-waveform redatuming is performed to the depth level (z_A) of $500m$. The estimated reflection response $\hat{\mathbf{X}}_B$ in Figure 5.4a can be compared with the direct forward-modeled reflection response without the gas imprint (Figure 5.4b). The two figures are very similar, indicating the quality of the deconvolution result. By comparison, Figure 5.4c shows the conventional redatuming result, which includes only the first arrivals of $\hat{\mathbf{W}}_A^+$ and $\hat{\mathbf{W}}_A^-$.

5.2.2 Nonlinear full-waveform inversion results

For the 1.5D experiment, the inversion is performed in the tau-p ($\tau - p_x$) domain with parameters shown in Table 5.3.

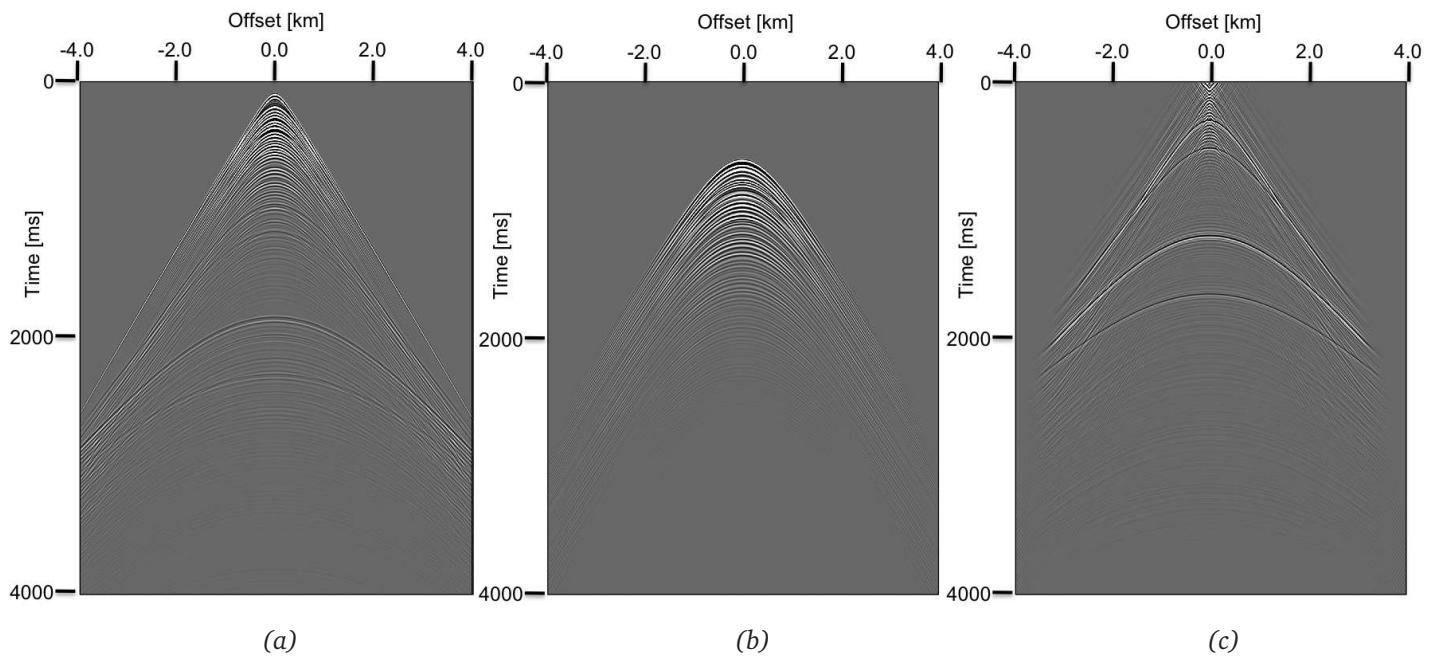


Figure 5.3 Demonstration of the full-waveform transmission deconvolution process where the transmission operators are calculated from the true 1.5D medium. (a) Total reflection response. (b) Full waveform transmission operator $W_A^- \cdot W_A^+$. (c) Full waveform deconvolution result. Note that the redatuming results are performed to the depth level (z_A) of 500m.

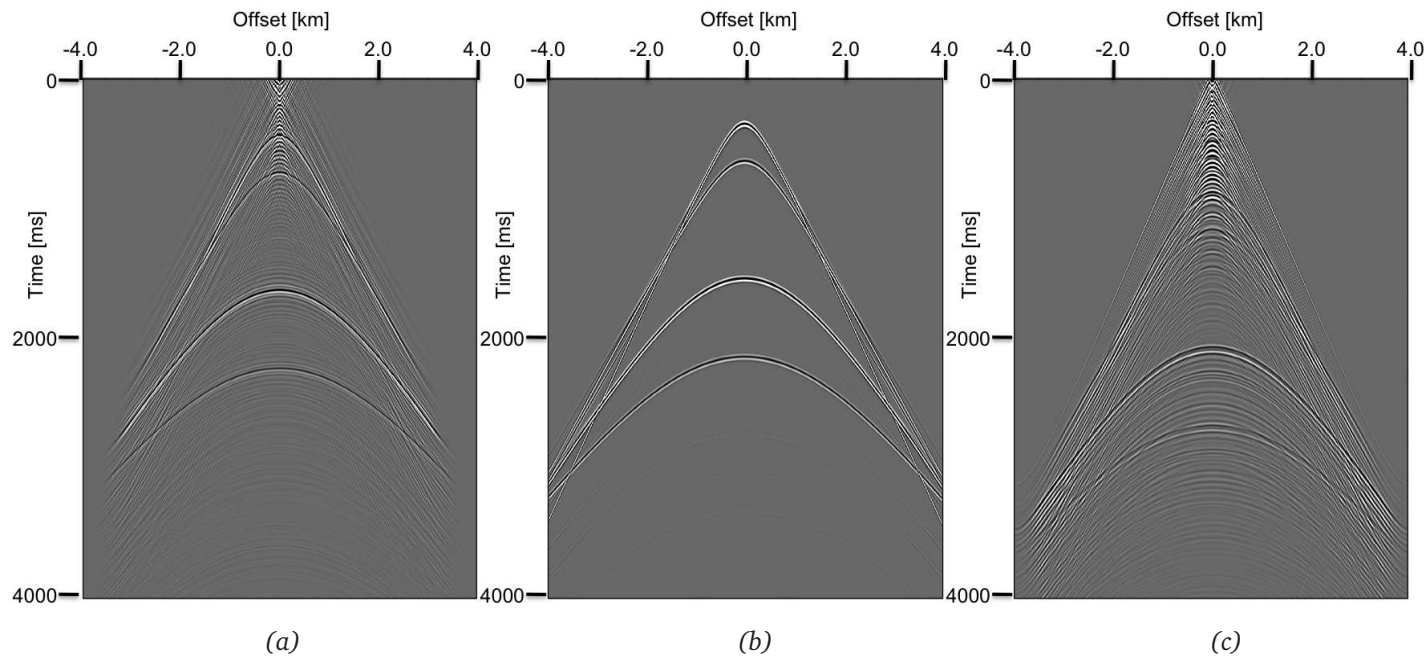


Figure 5.4 (a) 1.5D full-waveform deconvolution result using the correct transmission operators in Figure 5.3b. (b) Forward model of the reflection response as if the data was acquired at depth z_A without any influence of the gas cloud in the overburden. (c) Redatuming using first arrivals of \hat{W}_A only (i.e. redatuming via simple back propagation). Note that also, the redatuming results are performed to the depth level (z_A) of 500m.

Table 5.3 Example of 1.5D nonlinear full-waveform Genetic Algorithm inversion parameters.

Ray-parameters to invert	$p_x = 0$ [s/m] $p_x = 1.5 \cdot 10^{-04}$ [s/m] $p_x = 3 \cdot 10^{-04}$ [s/m] $p_x = 4.5 \cdot 10^{-04}$ [s/m]
Number of property parameters $2N$	250 x 2 (for velocity and density)
Number of realizations per population M	60
Number of populations K	5
Frequency range to invert	0 – 10 [Hz] 0 – 20 [Hz] 0 – 35 [Hz]
Chance of mutation	25%
Chance of crossover	10%
Chance of reinitialization	35%
Maximum iterations	300

After the GA finished, the parameter set with the best objective function value \mathcal{J} is selected and considered to be the solution of the inversion. The results for velocity and density are shown in Figure 5.5 for each of the three frequency ranges. Note the improved matching with the true models when the frequency band is broadened. Also note that though the solution does not fully match the exact model we only require for an effective model that explains the reflection data.

Figures 5.6(a,c,e) show the reflection response of the ray-parameter $p_x = 0$ [s/m], in which the true model response (red curve) is compared to the estimated response (blue) at 10Hz, 20Hz and 35Hz respectively. Figures 5.6(b,d,f) display the reflection response at $p_x = 3 \cdot 10^{-04}$ [s/m] at these frequency bands. The model estimated by the GA provides a reflection response with a very good resemblance to the true response for both p_x -values when compared to the true model.

5.2.3 1.5D transmission deconvolution results

Finally, the forward-modeled propagation operators for the estimated model are applied as deconvolution operators to the total reflection response \mathbf{P} to obtain $\hat{\mathbf{X}}_B$. Figure 5.7a displays the original total reflection response for $p_x = 0$ [s/m] at a larger time scale. The redatumed results is shown in Figure 5.7b (blue curve) and compared to the deconvolution result with the true transmission response (red curve). Note the excellent deconvolution result that is obtained with the estimated transmission response. Although there seems to be an overall scale factor, the primary reflections have been well recovered from the transmission inter-

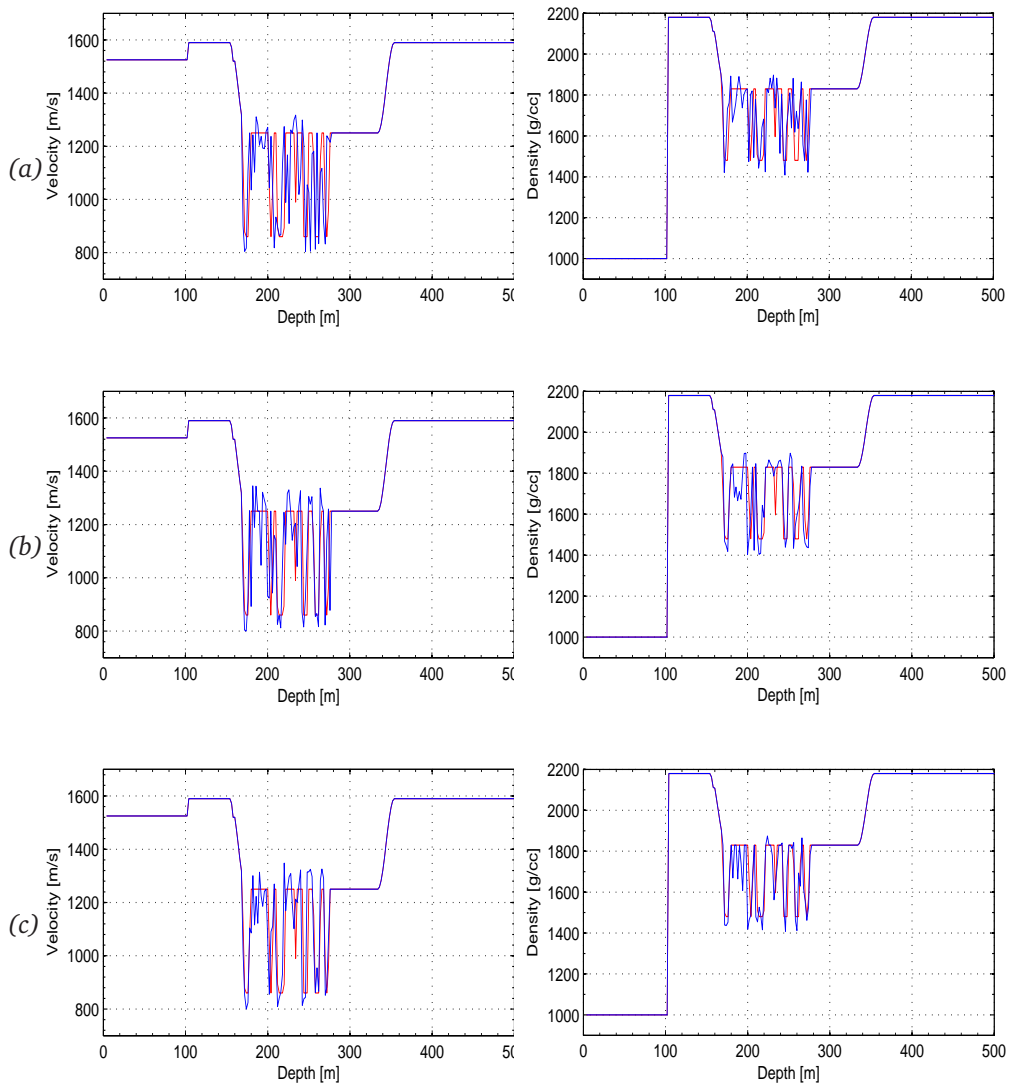


Figure 5.5 The estimated property models using the frequency marching GA full-waveform inversion method at frequencies 10Hz, 20Hz and 35Hz. Red lines are the true property models and blue lines are the inversion results. The final nonlinear inversion of each frequency range is the initial model for the subsequent higher-frequency range. Stepping from (a) to (c) shows the improvement in estimating the true property model.

ference. The quality of the deconvolution result is further proved when we compare this result with direct forward-modeling result of the reflection response without the gas imprint (Figure 5.7c). The difference between the deconvolution results of Figure 5.7b and

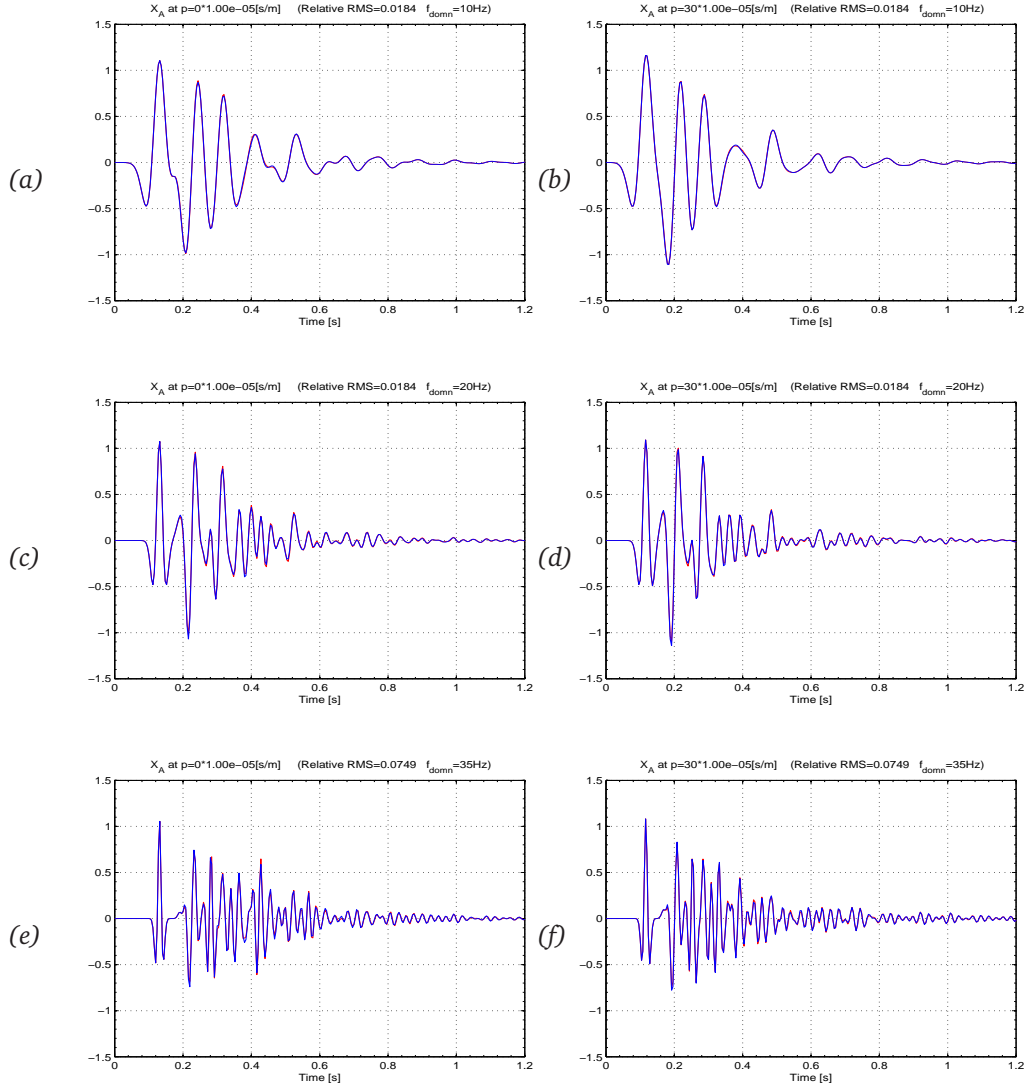


Figure 5.6 The frequency-marching full-waveform forward-modeling results at frequencies of 10Hz , 20Hz and 35Hz . Red lines are the full-waveform response of p_A using the true property models and blue lines are the results of full-waveform response \hat{p}_A using the GA inversion process. (a,c,e) show the reflection responses p_A at normal incidence (ray-parameter $p_x = 0$ s/m) and (b,d,f) show this at $p_x = 3.10^{-04}$ [s/m] for each maximum frequency.

the forward-modeled response in Figure 5.7c can be attributed to residual deconvolution artifacts and multiples between area A and B , which are not accounted for.

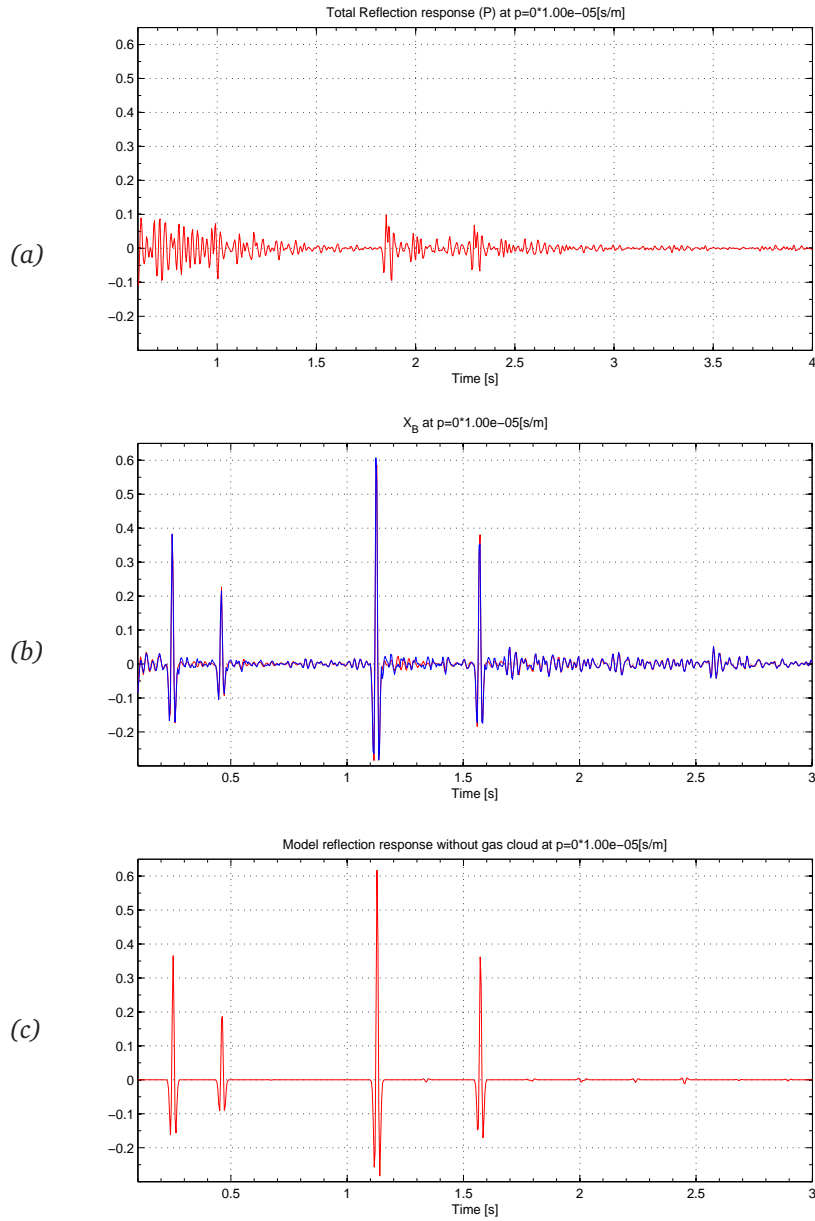


Figure 5.7 (a) Zoom of the total reflection response at $p_x = 0$ [s/m]. (b) Deconvolved reflection responses from area B, \hat{X}_B . Red lines are full-waveform redatuming of X_B using the true property models and blue lines are the results of full-waveform redatuming response \hat{X}_B using the estimated effective medium. (c) Forward-modeled reflection response X_B as if it was acquired at depth z_A , without the gas cloud as the overburden.

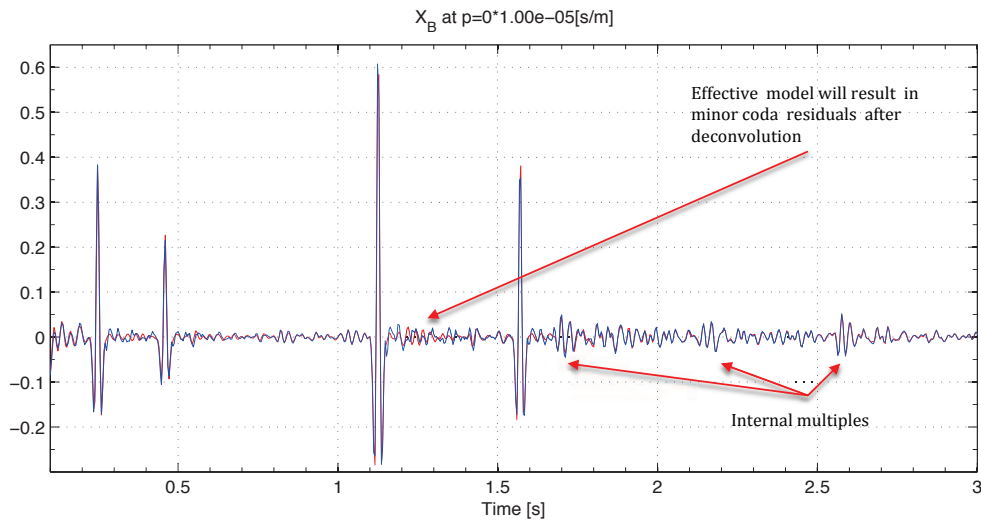


Figure 5.8 Zoom of the full-waveform deconvolution result in Figure 5.7b. Arrows point to residual errors that arise from the fact that only an effective model of area X_A is estimated and used as the deconvolution operator. The minor coda residuals appear as the remnant of the deconvolution result. Red lines are full-waveform redatuming of X_B using the true property models and blue lines are the results of full-waveform redatuming response \hat{X}_B using the estimated effective medium.

Figure 5.8 shows again the full-waveform deconvolution result (Figure 5.7b) where the remnant error is present as a minor coda of deconvolution residuals, due to the fact that the effective model is used instead of the true model. Also, since the internal multiples between the base of the gas area and zone B are neglected, these multiples still survived in our deconvolution result. Overall, the true-amplitude reconstruction of the reflectors underneath the gas area is very good and the residual coda and internal multiples can be ignored and regarded as noise.

Figure 5.9 shows the deconvolution results for a range of p_x -values. Note again that, due to the gas cloud transmission effects, the target primaries are difficult to interpret in the input (Figure 5.9). Figure 5.9b,c shows the deconvolution results using transmission operators from respectively the true and the estimated models. The corresponding deconvolution result \hat{X}_B (Figure 5.9c) matches the deconvolution result obtained with the true transmission operator (Figure 5.9b) very well for all p_x -values. This is confirmed by the difference plot in Figure 5.9d. Note that the slightly larger residuals present at the large ray-parameters.

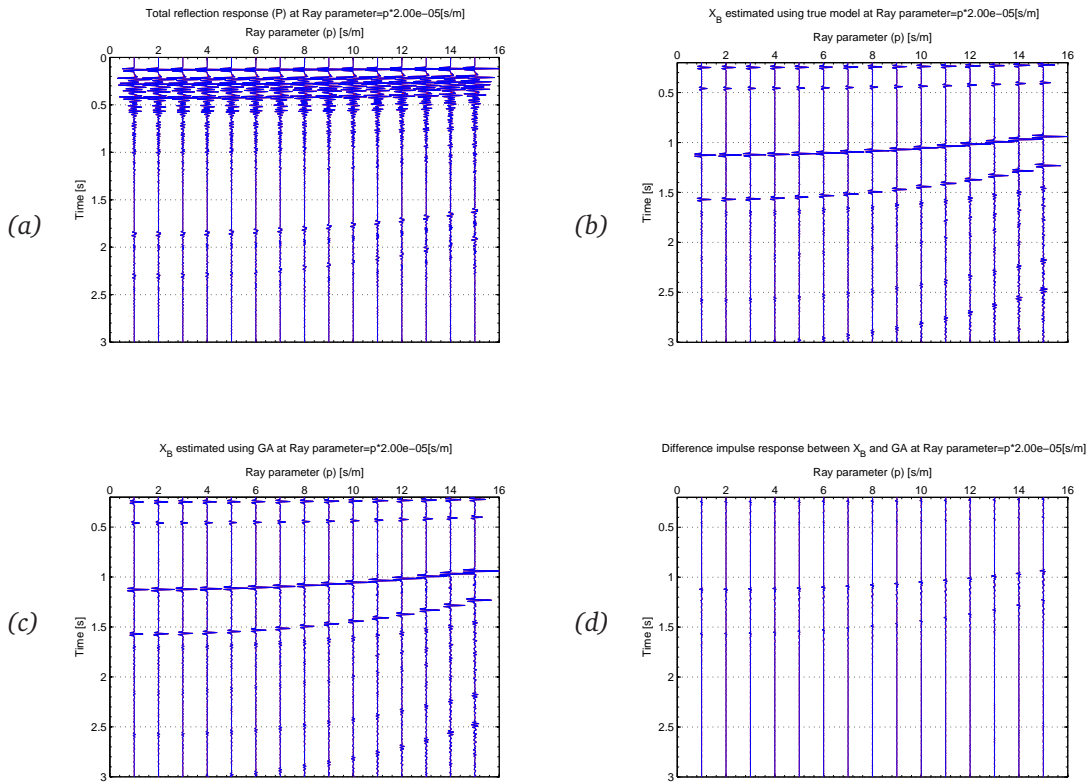


Figure 5.9 (a) Total reflection response P , from the surface displayed in the $\tau - p$ domain. (b) Deconvolution result \hat{X}_B obtained with the transmission operators from the true model. (c) Deconvolution result when using the transmission operators from the best estimate of the model. (d) Difference between the responses in (b) and (c).

5.2.4 Statistical analysis of the inversion results

After the final iteration of the GA optimization at the highest frequency range, the estimated velocity and density function solutions are obtained. Next, we consider whether the effective equivalent medium can explain our observed reflections data of area A and can be used to estimate transmissions operators. Note that we are not aiming at getting medium parameters identical to the actual model, but rather want to estimate an equivalent medium that explains the reflection response and can subsequently generate a proper transmission operator. Because we know the true model in the synthetic example, we can also calculate the RMS difference for each realization of the transmission operator and the RMS difference for the deconvolved response \hat{X}_B compared to the result with the true deconvolution operator. One of the features of the GA optimization process is that each run provides a slightly dif-

ferent result. We can therefore, run the GA several times with different random number realizations. For each model realization obtained, the corresponding transmission operators \hat{W}_A can be calculated, and applied in a deconvolution process to the input data to obtain a the redatumed response \hat{X}_B . This provides an ensemble of deconvolution results that can be used for statistical analysis.

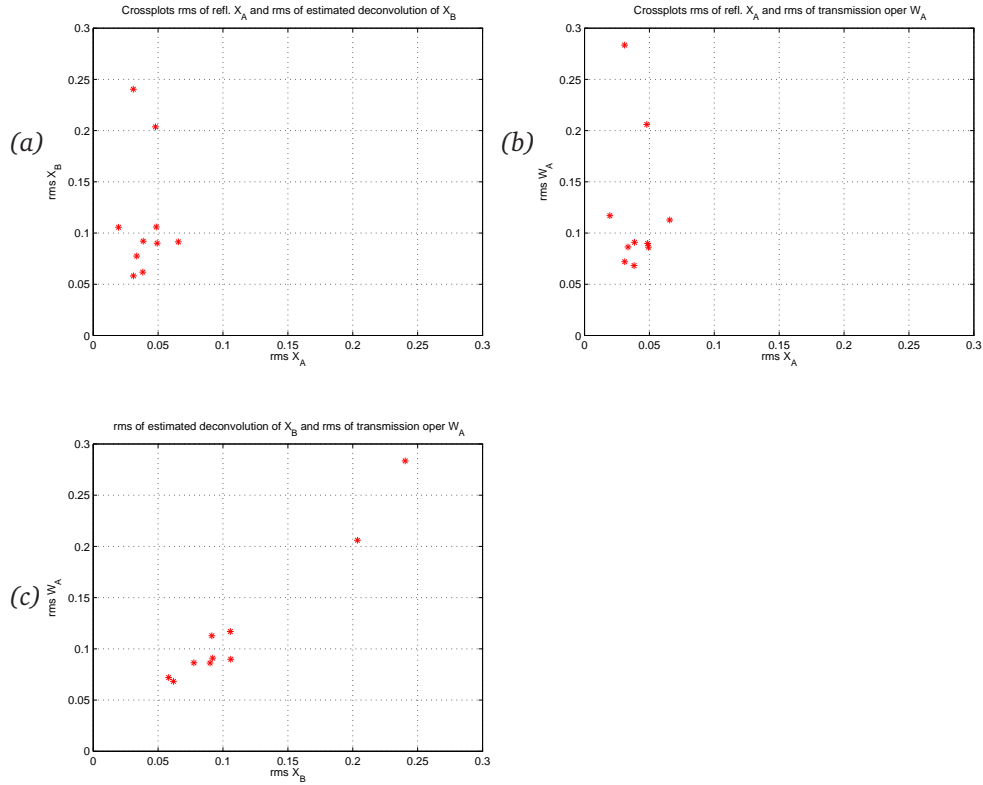


Figure 5.10 (a) Crossplot of the RMS values of the reflection responses \hat{X}_A with the RMS values of the corresponding deconvolution results \hat{X}_B for 10 different runs of the GA. (b) Crossplot of the RMS values of the reflection responses \hat{X}_A with the RMS values of the corresponding transmission operators \hat{W}_A . (c) Crossplot of the RMS values of the deconvolved responses \hat{X}_B with the RMS values of the corresponding transmission operators \hat{W}_A .

This statistical evaluation provides insight in the robustness, stability and tolerance of errors in estimating the transmission operators and the corresponding deconvolution results by nonlinear inversion from the gas cloud response. We will investigate the relationship between the reflection data obtained from each log realization with the transmission operators of \hat{W}_A . It may be that an effective model that explains the reflection response very well, does not necessarily describe the transmission effects accurately.

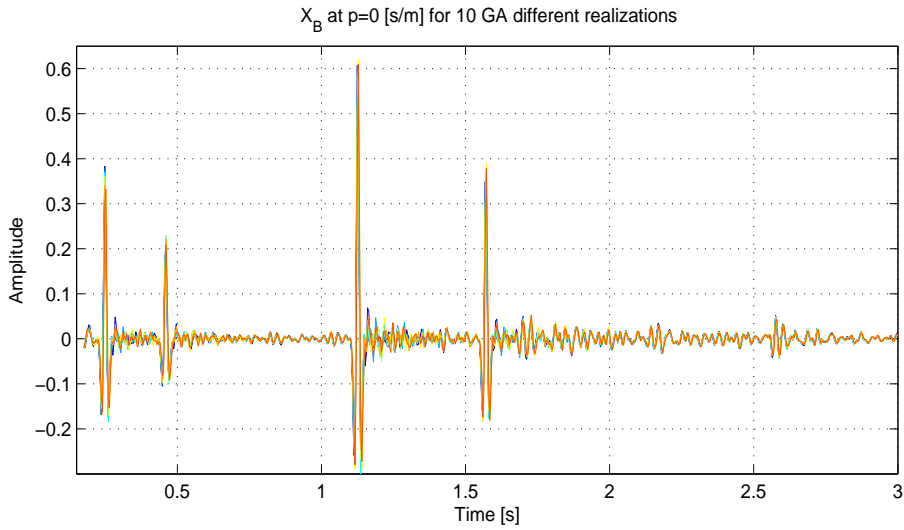


Figure 5.11 All realizations of the \hat{X}_B deconvolution results.

For this purpose the full *GA* inversion of the gas cloud reflection data was carried out. For each result, the RMS error of the estimated gas cloud reflection response was obtained. Furthermore, for each result the RMS difference of the obtained transmission operator and the transmission operator in the true model was calculated, as well as the RMS difference of the obtained response from zone *B* compared to the result obtained with the true properties. Because we are mainly interested in the amplitudes of the reconstructed reflection events and can accept small temporal shifts in the redatumed result, we used the envelopes of the deconvolution result (i.e. the estimated response of zone *B*) for its RMS calculation. Figure 5.10a to Figure 5.10c show their respective crossplot.

Figure 5.10a shows there is a good match in deconvolution result for each realization, as all RMS values of the deconvolution result are within 8% difference. There is, however, no clear correlation with the RMS values of the reflection response \hat{p}_A , but we can conclude that any effective model that gives a good match in reflection response also provides a very satisfactory deconvolution result.

To demonstrate that all inversion results give acceptable results, several realizations of the deconvolution results are plotted in Figure 5.11 for the slowness value $p_x = 0$. Note that the four reflection events are well recovered and that the differences mainly show up in slightly larger deconvolution residuals.

Figure 5.10b, which plots the RMS differences in the transmission operators versus the RMS errors in the reflection response, shows a similar behavior as Figure 5.10a, although the RMS values of the transmission operators are quite a bit larger than the RMS values of the

reflection response. Note that for the RMS values of the transmission operators the actual wavefield differences were used and not the difference of the envelopes. Combining the results of Figures 5.10a and 5.10b, in Figure 5.10c shows a crossplot of the RMS error in the transmission operator and the RMS error in the deconvolution result. As expected, the result shows a reasonably linear behavior.

5.3 2D Example

The results for the 1.5D case are encouraging enough to justify an extension of the inversion process to the full 2D case. However, extending this approach to a multidimensional nonlinear full-waveform inversion is not simple or straightforward. In this section we first perform a feasibility study of multidimensional transmission deconvolution and extend the nonlinear full-waveform inversion to multidimensional inversion using a global optimization process. From the estimated contrasts that effectively describe the reflection response of the gas cloud, transmission correction operators can be derived by forward-modeling. These can then be used in a multidimensional full-waveform deconvolution process to achieve true-amplitude imaging of the reflections below the overburden.

5.3.1 2D transmission deconvolution using the correct model

Given the success for the 1.5D case, we want to investigate the effectiveness and the viability full-waveform deconvolution process in 2D. Since the equations in the previous chapter (Chapter 3) are multidimensional in nature, application of the deterministic approach is quite straight-forward. The 2D true-amplitude full-waveform redatuming process will be demonstrated for synthetic data generated using a staggered grid finite-difference algorithm. One shot record from this survey is shown in Figure 5.12a. The source is located above the middle of the gas cloud (see Figure 3.1). Figure 5.12b shows a single shot record after the application of the multidimensional true-amplitude, full-waveform redatuming.

The transmission deconvolution operator \mathbf{W}_A^{-1} was obtained by forward-modeling the transmission operator \mathbf{W}_A using the exact model (Figure 3.1) with the receivers were placed at the arbitrary datum depth z_A of 500m and the sources were located at the surface in a model that only contains area A . This can then be used as a multidimensional deconvolution operator to be applied to the total reflection data. The transmission responses through the gas cloud were arranged for each shot in the columns of the transmission data matrices for each frequency ω . Next, these matrices were inverted, according to Equation 3.6, and applied to the total response, as described by Equation 3.7. Each matrix inversion was carried out in a stabilized least-squares manner.

Figure 5.13a shows a time stack section obtained from the surface data. Note the influence of the low-velocity anomaly on this time section resulting in delayed times and poor quality of the reflections from below the gas cloud. Figure 5.13b displays the result of our

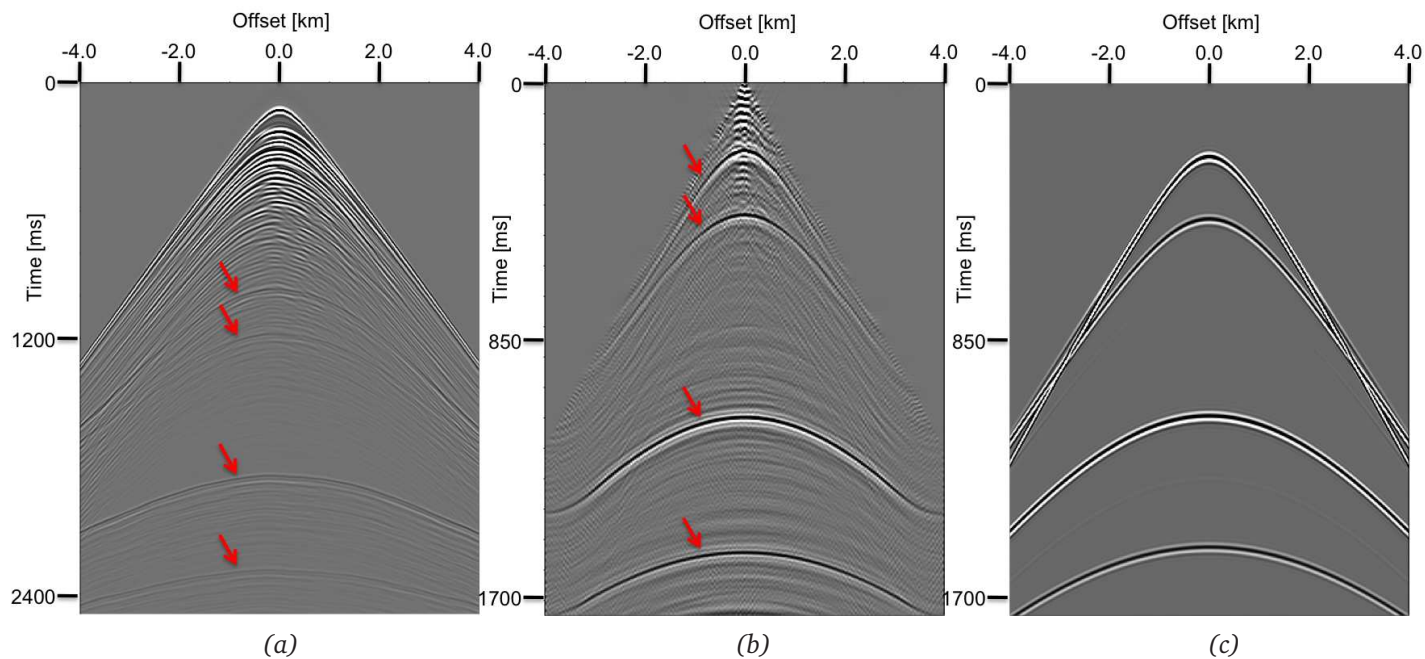


Figure 5.12 (a) Shot record generated using the actual 2D property model in Figure 3.1 with a source above the centre of the gas cloud area. The four reflectors underneath the gas cloud area are hard to recognize (indicated by the arrows). (b) Shot after true-amplitude redatuming with the source at the same lateral position as Figure 5.7a. The arrows point at the reflections from the four target horizons. (c) Forward model of the reflection response as if the data was acquired at depth z_A of 500m without any influence of the gas cloud in the overburden.

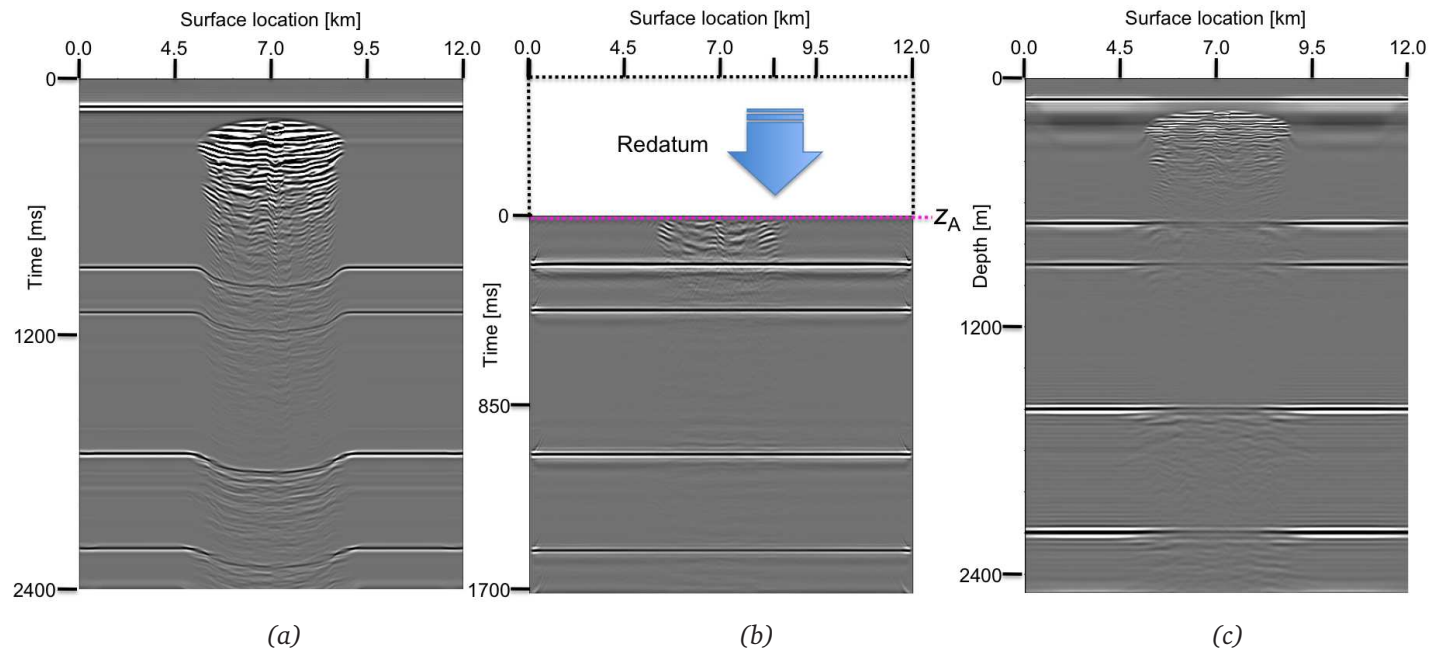


Figure 5.13 (a) Stack section resulted from acoustic finite-difference modeling of the actual 2D property model in Figure 3.1. Note the influence of the low-velocity anomaly on this time section and the poor quality of the reflections underneath the gas cloud. (b) Stack section from the estimated response \hat{X}_B after full-waveform transmission correction. Note that the target horizons are correctly recovered and also note that the transmission codas have been properly removed. Note that the full-waveform redatuming is performed to the depth level (z_A) of 500m. (c) Prestack depth migration result of the data simulated in the model of Figure 3.1. Note the imprint on this result in terms of amplitude loss and residual coda energy below the gas cloud area.

true-amplitude redatuming where the redatuming is performed to the depth level (z_A) of 500m, with post-redatuming NMO velocity analysis and stack. Note again that the target horizons are correctly recovered and that the transmission codas are also properly removed. The prestack depth migration result using the correct velocity and density model is shown in Figure 5.13c. It shows that given the correct velocities, the kinematics can be solved satisfactorily below the gas cloud area, but that the amplitude imprint and coda remain for all deeper reflectors.

Table 5.4 Example of 2D nonlinear full-waveform via Genetic Algorithm inversion parameters. Forward modeling using acoustic finite-difference algorithm at a 20m-grid.

Model boundary	$x[\text{km}] = (0.0, 14.)$ $z[\text{km}] = (1.0, 1.0)$
Inverting parameter range	$velocity[\text{km}/s] = (0.8 \sim 1.3)$ $density[\text{kg}/\text{m}^3] = (1.430 \sim 1.880)$
Model grid size for inversion [$dx \times dy$]	20m x 20m
Modeling grid of the observed data [$dx \times dy$]	2m x 2m
Minimum x -location to invert	5.0[km]
Maximum x -location to invert	9.0[km]
Minimum depth to invert	0.150[km]
Maximum depth to invert	0.350[km]
Maximum frequency to invert at 20m-grid	9[Hz]
Number of CPU's use for inversion	22
Number of populations [K]	10
Number of realizations per population [M]	273
Number of parameters [$2N$]	2 x 200 x 10
Number of correlation samples shift (n)	$-36 \times 4\text{ms} \leq n \leq 36 \times 4\text{ms}$
Center of gas cloud	(7.0, 0.225)[km]
Gas cloud background lens size	$x = 4.0$ [km] $z = 0.2$ [km]
Shot spacing	1000m
Number of shots to invert	5
Receiver spacing	20m
Maximum spread offset per side	1500m
Total spread offset	3000m
Record length	2.5s
Sample interval	4ms

5.3.2 2D nonlinear full-waveform inversion using a Genetic Algorithm

In order to implement the 2D full-waveform GA inversion cost-effectively and efficiently, we start to invert using the lowest frequency range of $0 - 9Hz$ at the finite-difference modeling grid size of $20m$ by $20m$ and step through to the frequency ranges of $0 - 9Hz$, $0 - 18Hz$ and $0 - 35Hz$. For each frequency range we build up the background model from the output of the previous frequency range and finally get to a more detailed model. Forward modeling with larger finite-difference grid for the lower frequency takes less time to execute. We started inverting from a $20m$ -grid, then to a $10m$ and finally to a $4m$ grid size. This also includes limiting the inversion area to a localized area of $4000m \times 200m$ instead of inverting for the whole model as shown in Table 5.4.

For the higher-frequency range of $0 - 35Hz$, to avoid dispersion, the maximum finite-difference grid scale is $5m$ and the total number of parameters to invert is $2 \times 800 \times 40$ for both velocity and density. The number of populations (K) and number of realizations (M) are limited to only 5×21 due to limited computing resources.

In this inversion process, we purposely selected incorrect parameter values for the initial

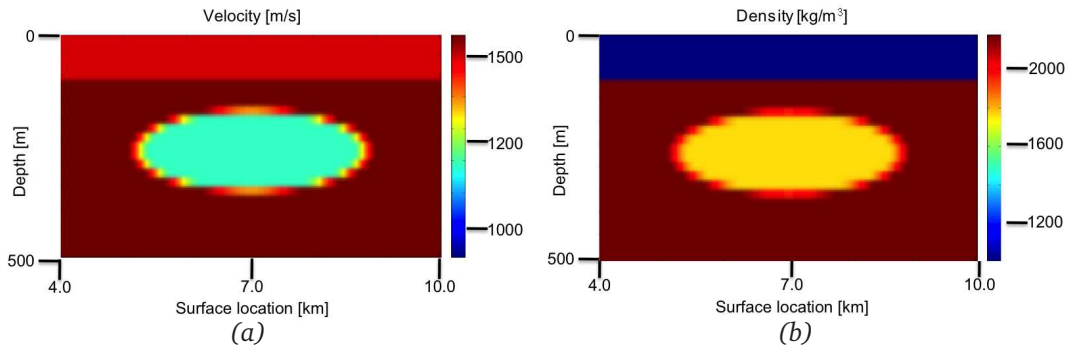


Figure 5.14 (a) The initial background velocity model [m/s] for nonlinear full-waveform inversion on a $20m$ grid with $f_{max}=9Hz$. (b) The initial background density model [kg/m³].

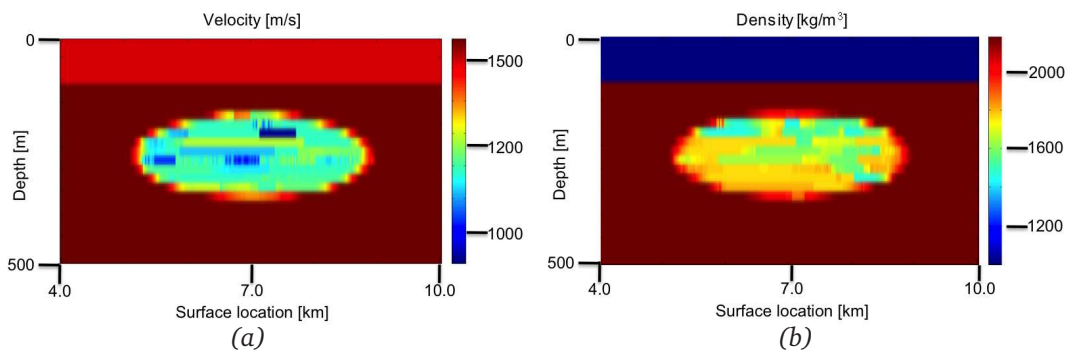


Figure 5.15 (a) The 2D nonlinear full-waveform inversion for velocity [m/s] at $20m$ grid for $f_{max}=9Hz$. (b) The density model [kg/m³].

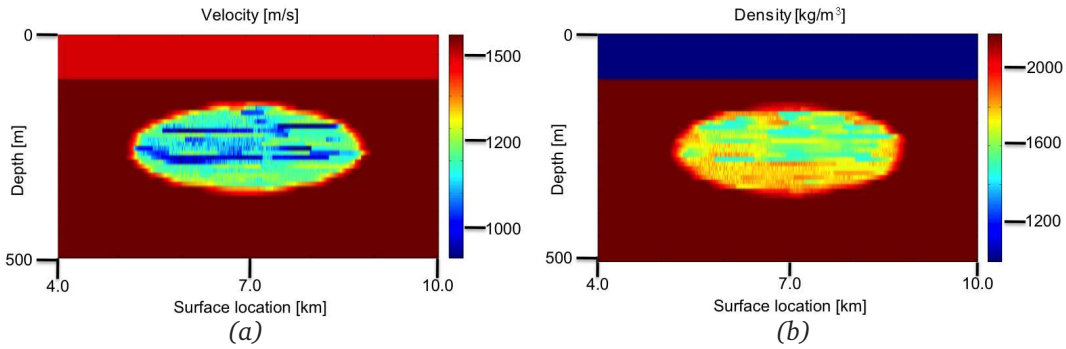


Figure 5.16 (a) The inversion result for velocity [m/s] for a 10m grid and $f_{max}=18Hz$. (b) The density model [kg/m³].

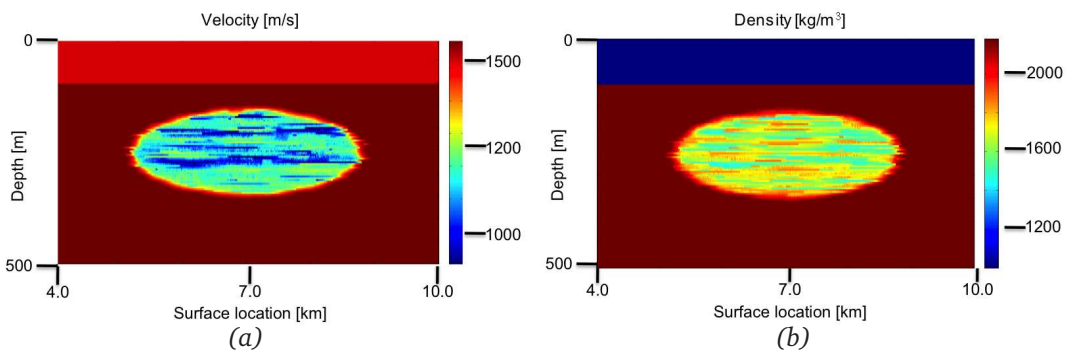


Figure 5.17 (a) The final 2D nonlinear full-waveform inversion for velocity [m/s] for a 5m grid and $f_{max}=35Hz$. (b) The density model [kg/m³].

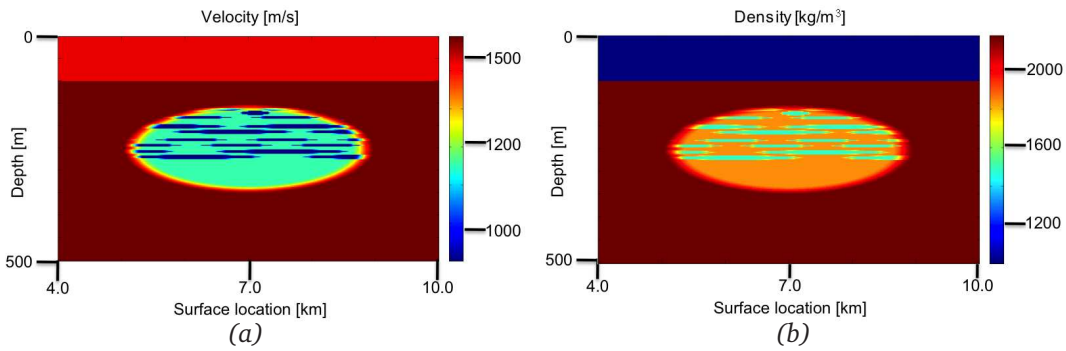


Figure 5.18 (a) The actual velocity model [m/s]. (b) The actual density model [kg/m³]. The grid sampling is 2m.

model. Figures 5.14a and Figure 5.14b are the initial background models for velocity and density at the 20m finite-difference grid with five shot locations as the input to the nonlinear inversion. Figures 5.15a,b are the estimated nonlinear full-waveform inversion results for the 9Hz inversion. The low frequency nonlinear inversion brought the effective model from

the incorrect initial model to a more accurate background model.

The final inversion result as shown in Figures 5.17a,b show a good resemblance to the actual model geometry. Furthermore, the parameter values can be compared to the actual velocity-density model in Figures 5.18a,b where the grid size is $2m$. The result of subsequent higher frequencies, as shown in Figures 5.16 and 5.17, with grids of $10m$ and $4m$ respectively, start to show more details of the gas-bearing inclusions. Figures 5.16a,b are the inversion results for $18Hz$ at $10m$ FD grid scale. Figures 5.17a,b are the inversion results for $35Hz$ at $4m$ finite-difference grid. Due to limited computational resources where we only compute for $800 \times 400 \times 2$ parameters of 21 realizations and 5 populations. This means that the sampling of the solution space was quite poor, and suboptimum results are expected. The actual velocity v and density ρ models for X_A are shown in Figure 5.18. It can be concluded that the inverted $9Hz$ inversion results produced a good background model for the low velocity and low density of the gas but still lacks details. By comparison, the $35Hz$ inversion results has some details of the actual gas pockets, although we are not aiming at estimating the actual gas cloud model but only an effective medium.

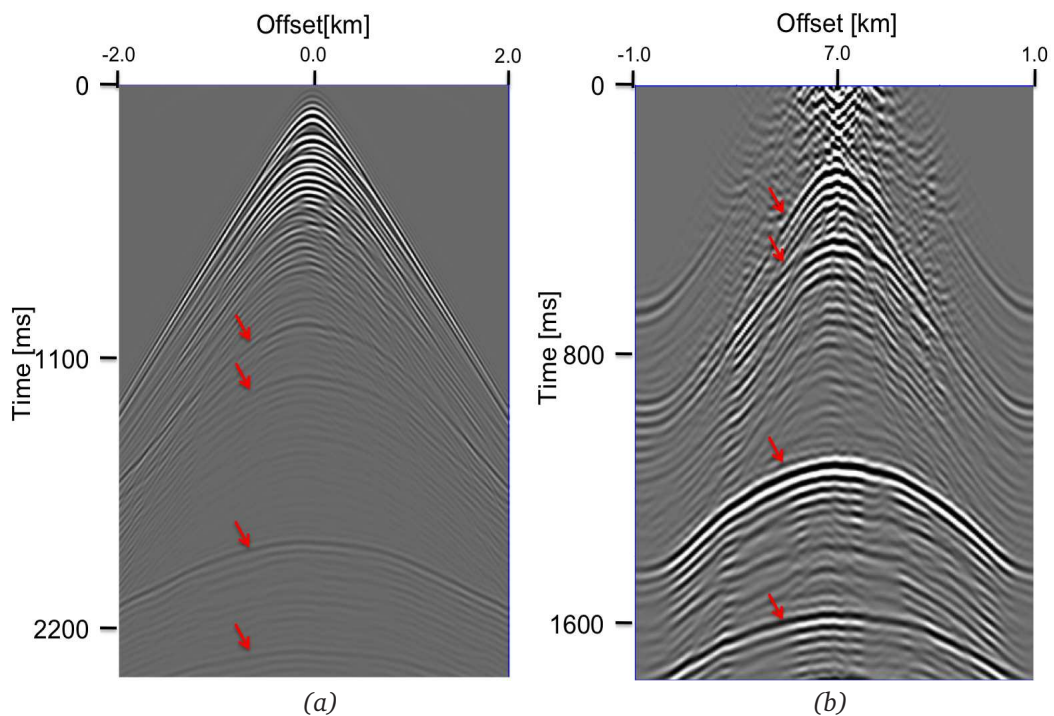


Figure 5.19 (a) Shot record generated using the actual property model in Figure 3.1 with a source above the gas cloud area. (b) Shot after true-amplitude redatuming. The arrows indicate at the reflections from the four target horizons.

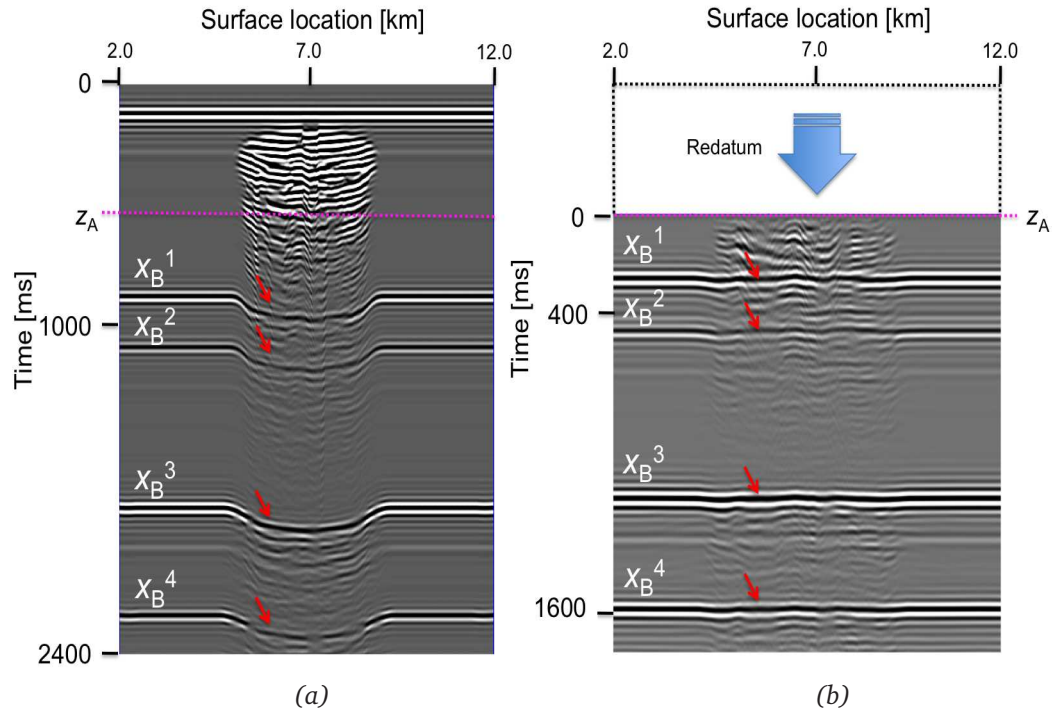


Figure 5.20 (a) Stack section from acoustic finite-difference modeling of the actual property model in Figure 3.1. Note the influence of the low-velocity anomaly on this time section and poor quality of the reflections underneath the gas cloud as indicated by the red arrows. (b) Stack section from the estimated response X_B obtained from the effective model after full-waveform transmission correction. Note that the full-waveform redatuming is performed to the depth level (z_A) of 500m (see Figure 5.13 for redatuming result using the actual property model).

To validate the estimated model, we apply the full-wavefield redatuming as proposed in Chapter 3. For this process, the estimated model from the final nonlinear full-waveform inversion (Figures 5.17a,b) are used to forward-model the full-waveform transmission operators. Receivers were placed at the arbitrary datum depth $z_A = 500m$ and the sources were located at the surface. The transmission responses through the estimated gas cloud model were arranged for each shot in the columns of the transmission matrices at each frequency ω . Then, these matrices were used to obtain \mathbf{W}_A^{-1} , according to Equation 3.6, and applied to the total response $\mathbf{P} - \mathbf{X}_A$, as described by Equation 3.7.

Figure 5.19b shows a shot record after the application of the true-amplitude full-waveform redatuming. We can observe some reduction of gas cloud transmission imprint on the four target reflection below the gas (see the arrows). Figure 5.20a shows a time stack section response obtained from the surface data. Note the influence of the low-velocity anomaly on this time section resulting in delay times and the poor quality of the reflections underneath

the gas cloud. Figure 5.20b displays the result after the true-amplitude redatuming, followed by conventional normal moveout velocity analysis and stack. Note that the amplitudes of the target horizons, indicated by the red arrows, are recovered and that the transmission codas are reduced.

6

Application to field data

In this chapter, we apply the total gas-cloud inversion strategy to a 2D line from a real marine seismic dataset. The main idea of the process is to perform depth-redatuming of seismic data using accurate transmission operators that are obtained from the result of using a 2D waveform-inversion method to get an effective overburden model. In practice, this is very challenging because of noise levels and acquisition constraints of real data, as well as limitations in the assumptions of our forward model in particular, that earth is acoustic and loss-free. Perhaps the largest limitation in our current implementation is the fact that we restrict ourselves to the 2D case whereas we know that gas-clouds are inherently 3D in nature. Therefore, in this field data study we will not even try to invert for the gas cloud itself but instead focus on propagation in the overburden, where other strong contrasts are also present.

Our approach is as follows: first we discuss essential preprocessing techniques, including surface-related multiple elimination by using the *EPSI* technique (see van Groenestijn and Verschuur, 2009a; van Groenestijn and Verschuur, 2009b). Secondly, we describe the implementation of the nonlinear full-waveform inversion for the overburden using 2D acoustic finite-difference modelling and our Genetic Algorithm technique. Finally, applying the inverse full-wavefield transmission operators to the field data, we obtain an estimate of the true-amplitude seismic image below this overburden.

6.1 Geological background

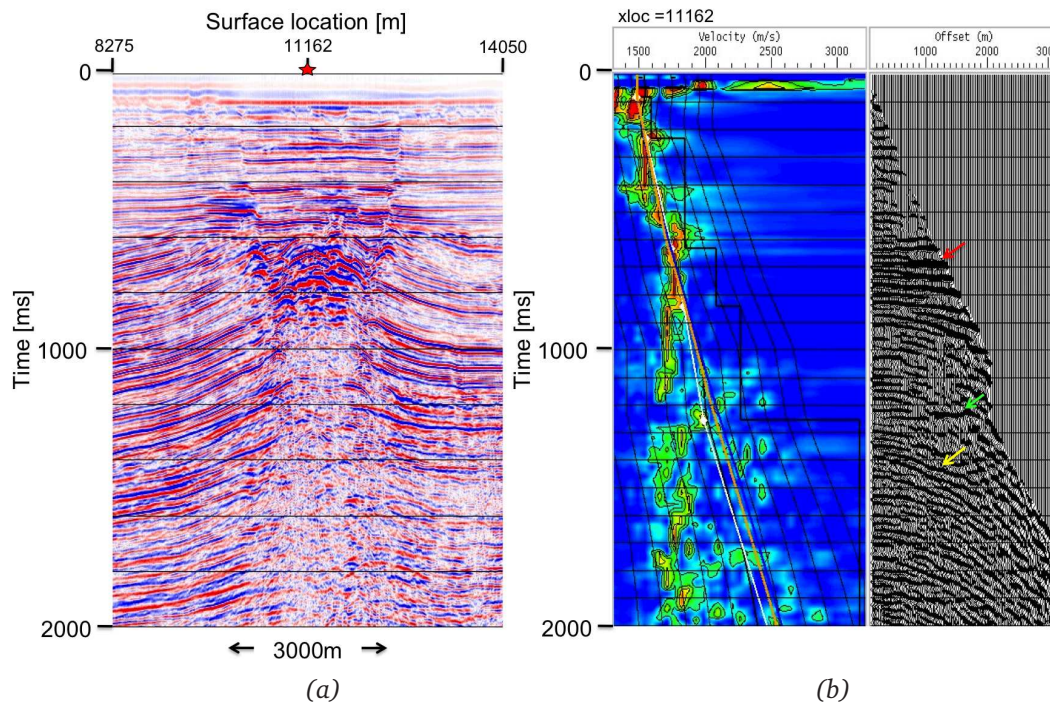


Figure 6.1 (a) Prestack time-migrated of a 2D seismic line from a gas cloud problem area in the Malaysian basin. (b) Velocity analysis panel showing velocity trends with the overlaid interval velocity (in solid black line) for the location marked by the red star in (a). The red arrow shows strong internal multiples inside the gas-cloud area while the green arrow shows the primary reflection event obscured underneath the strong multiple energy. The yellow arrow indicates at the surface-related multiples.

The field dataset used in this thesis is provided by Petroliaam Nasional Berhad (PETRONAS). The data that will be used in this study is a subset taken from a 2D marine seismic line from a region with a gas-cloud problem in the Malaysian basin. Nearby well information was used as a priori knowledge for the inversion process. The study area is located around 275km offshore east of the Malaysian peninsular and has an average water depth of about 75m. It is situated in a graben structure with an anticlinal central feature that consists of two main fault closures on the eastern and western part of the fault blocks, as shown in Figure 6.1a. There is a major discontinuity of midpliocene unconformity positioned at around 0.6s (at 450m depth) separating the younger tertiary sediments from the older sediments underneath. The majority of the sediments from the seabottom to the unconformity are made of soft clay-rich sandstone and thinly-layered limestone. Below the unconformity the sediments consist of clay-rich sandstone and thick sandstone with thinly-layered coal-shaly

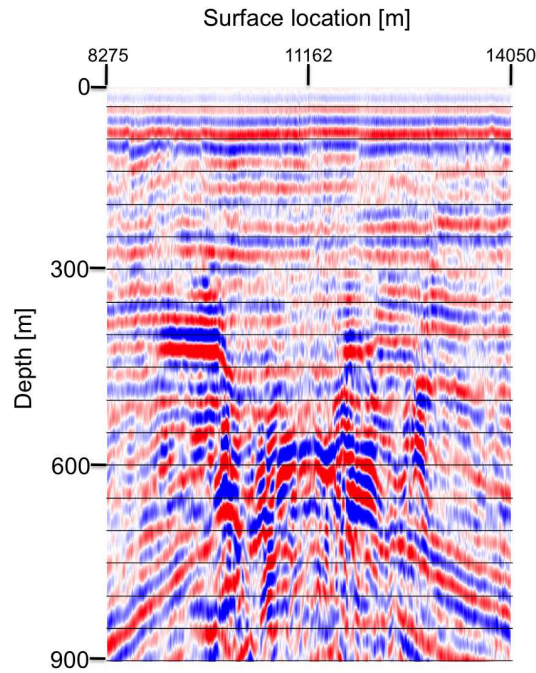


Figure 6.2 Lowpass filtered version of the prestack time-migrated section in Figure 6.1a, after conversion to depth using a smooth interval velocity model.

beds, shale and limestones. Average porosity in the main reservoir is around 27% and the gross sandstone thickness is around 85m. There are hydrocarbons in multiple reservoirs in the area. The thinly-layered coal beds, limestones and gas-charged sediments as well as the complex faulting cause strong internal multiples and scattering especially in the central area beneath the unconformity.

The red arrow in Figure 6.1b shows the strong internal multiples inside the gas cloud area, while the green arrow shows the primary reflection event obscured underneath the strong multiple energy, the yellow arrow shows prominent surface-related multiples.

We have selected part of this line for our tests. The selected part consists of 300 shot records of 120 receiver channels with shotpoint and receiver intervals of 25m. The shortest source-receiver offset is 135m and the largest offset is 3110m. The time sample interval Δt is 0.002s and each trace has a total of 2500 data samples, although this is later resampled to 1250 samples with an interval of 0.004s. The missing near offsets were interpolated using a parabolic Radon method (Kabir and Verschuur, 1995). Since we need a square data matrix for our matrix inversion process, i.e. a fixed receiver spread where each location will act as source position, and our data have a marine configuration (Figure 2.7a), we use the reciprocity theorem to achieve a split-spread configuration and fill the remaining data matrix

with zero-traces (Figure 2.7b). Note that the reciprocity principle only applies if the source and receiver configuration is identical and the directivity effects are removed. The data was preprocessed, prestack migrated in time, lowpass filtered and converted to depth using a smooth interval-velocity model (Figure 6.2).

6.2 Estimation of primaries by sparse inversion

In relation to the proposed method as described in Chapter 3, the transfer functions of the earth impulse responses denoted by \mathbf{X}_A and \mathbf{X}_B in Equation 3.2 do not include surface-related multiples but only the internal multiples. In conventional migration techniques, both surface-related multiple and internal multiples are considered to be noise that must be removed, and any remaining multiples generate strong migration ‘smile’ noise in the final migrated section. For example, in their study Tanis et al. (2006a) designed a targeted and cascaded deconvolution process to remove strong internal multiples in $x - t$ and $\tau - p$ domain. However, in our case, it is essential that the internal multiples are retained, since they contain important information on the gas cloud medium itself.

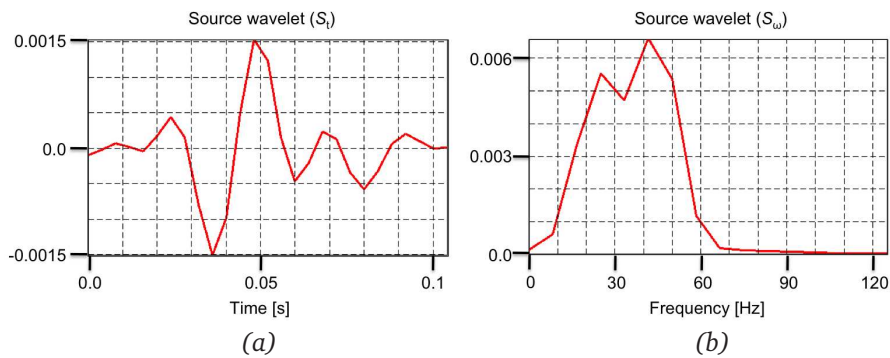


Figure 6.3 (a) Source wavelet estimated by the EPSI method. (b) The associated frequency spectrum.

For our tests, we require wave-equation-based techniques to remove the surface-related multiples rather than statistical deconvolution techniques. In particular we use the ‘*Estimation of primaries by sparse inversion*’ (EPSI) method developed by van Groenestijn and Verschuur (2009b). EPSI is a full-waveform inversion approach that estimates the primaries as unknowns in a multidimensional inversion process rather than using subtraction as in the well-known ‘*Surface-Related Multiple Elimination*’ (SRME) (see Verschuur and Berkhout, 1997; Verschuur, 2006). Note that the term ‘primaries’ here refers to events that have not reflected at the surface, which includes internal multiples and converted waves.

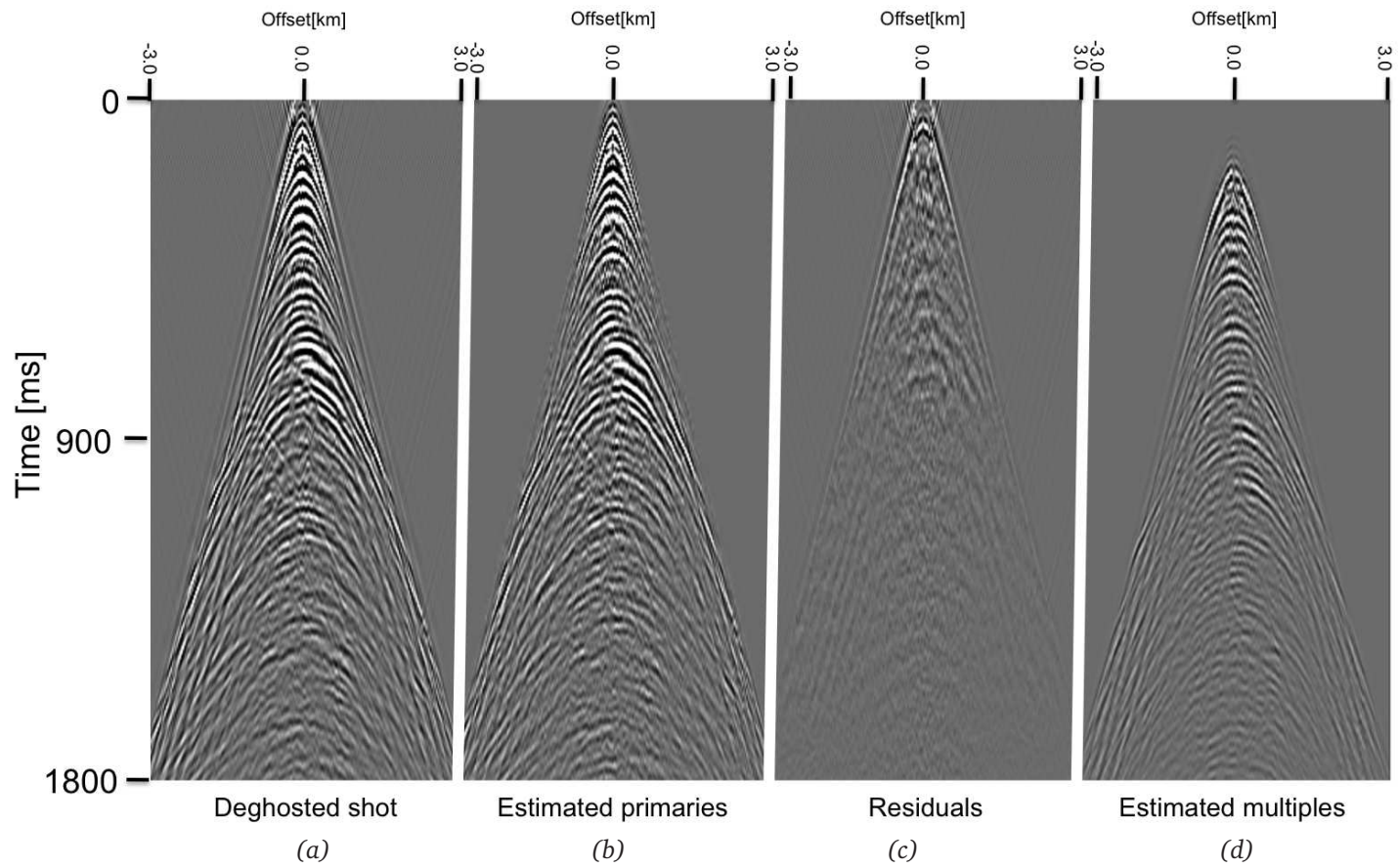


Figure 6.4 (a) A shot gather with multiples taken from the middle of the section in Figure 6.1a. The receiver ghost has been removed from this dataset. (b) The direct primary estimate obtained with the EPSI method. (c) Residual of the input data that is not being estimated by EPSI. (d) The estimated multiples from the EPSI method. Note that (b), (c) and (d) add up to (a).

In our case the advantages of applying the *EPSI* method is that it can provide an optimum:

1. extraction and estimation of the source wavelet;
2. reconstruction of missing near-offset traces at small times (i.e. from 0 to 150ms);
3. removal of surface-related multiples.

It is important to obtain an optimum source wavelet ($S(\omega)$) directly from the data since this wavelet is also used in the full-waveform inversion and is essential for minimizing the difference between the observed data $p_A(x, t)$ and the forward-modeled data $\hat{p}_A(x, t)$.

Figure 6.3a shows the source wavelet that has been estimated from the seismic data by *EPSI* together with its frequency spectrum (Figure 6.3b). Figure 6.4a shows a shot gather with multiples taken from the middle of section in Figure 6.1a before surface-related multiple removal. In addition to interpolation of missing near offsets both the receiver ghost and post-critical water reverberations have been removed. Figure 6.4b shows the primary estimate obtained with the *EPSI* method, (c) is the residual of the primary energy that is not being estimated by *EPSI* and (d) shows the estimated multiples.

6.3 Inversion strategy

In the implementation of 2D inversion, the initial velocity model is built by integrating the well information and prestack migration-velocity analysis (*MVA*) from the seismic data. The velocity picks are also consistently correlated with the main observable geologic reflectors. The paramount issue of picking velocities in the gas cloud area is the nonhyperbolic behaviour of the primary reflections because of the complex propagation through the overburden. We assume that we have obtained a proper background velocity field from *MVA* and that this explains the kinematics. The velocity field is then converted to a smooth interval velocity model that can be used as the starting point for the full-waveform inversion process. The initial background density model is then derived from the calculated interval velocities using the Gardner-Gardner-Gregory empirical relations (see Mavko et al., 2003), which we found suitable for the Malaysian tertiary-basins:

$$\rho_{ij} = 1.741v_{p_{ij}}^{0.25}, \quad (6.1)$$

where ρ is in g/cm^3 and v_p in km/s . Figure 6.5 shows the initial velocity and density models that are input to the nonlinear full-waveform inversion process.

We implement the inversion in a recursive manner with two depth steps before finally performing the inversion globally. The area \mathbf{X}_A is divided into two parts: 0–450m and 0–900m. This makes that the *GA* inversion spend most of its iterations finding optimum parameter models that explain the data in a particular depth region before moving to the next depth. The full-waveform *GA* parameter settings are shown in Table 6.1. Twenty-nine shot records

Table 6.1 Overview of parameters and settings for the 2D nonlinear full-waveform inversion via a Genetic Algorithm applied to the real marine 2D dataset.

Model boundaries	$x[\text{km}] = (8.275, 14.050)$ $z[\text{km}] = (0.0, 1.5)$
Parameter range	$velocity[\text{km/s}] = (1.2 \sim 2.4)$ $density[\text{kg/m}^3] = (1.6 \sim 2.6)$
Model grid size $[dx \times dz]$	12.5m x 12.5m
Minimum x -location	8.275[km]
Maximum x -location	14.050[km]
Minimum depth	0.075[km]
Maximum depth	0.900[km]
Maximum frequency at 12.5m-grid	20[Hz]
Number of CPU used	22
Number of populations $[K]$	2
Number of realizations per population $[M]$	462
Number of parameters $[2N]$	2 x 462 x 66
Number of correlation samples shift	$-24 \times 4 \text{ms} \leq \Delta t \leq 24 \times 4 \text{ms}$
Shot spacing	200m
Number of shots (before blending)	29
Receiver spacing	25m
Record length	2.0s
Sample interval	4ms

are selected from the data after *EPSI*, \mathbf{P}^- . These twenty-nine shot records are then blended inside the *GA* inversion process to form a single blended shot record (see Chapter 4).

6.4 Results

To obtain an effective medium for \mathbf{X}_A , we only invert up to 900m depth and use a maximum frequency of 20Hz. Note that the lowest frequency in the data is 5Hz. To avoid problems with very long wavelets in the time domain and subsequent selection of events in the shots, we did not start the inversion with a lower frequency band. The results of nonlinear full-waveform inversion via the *GA* are shown in Figure 6.6 where Figure 6.6a displays the estimated effective velocity model and Figure 6.6b shows the estimated effective density model. Figure 6.7a shows the difference of the inversion results with respect to the initial velocity model, i.e. the estimated contrasts. Figure 6.7b shows the lowpass-filtered prestack image converted to depth.

The inversion results show that the shallow overburden already contains of high-contrast heterogeneities. The black ellipse denotes the gas-cloud area and the black arrows point to

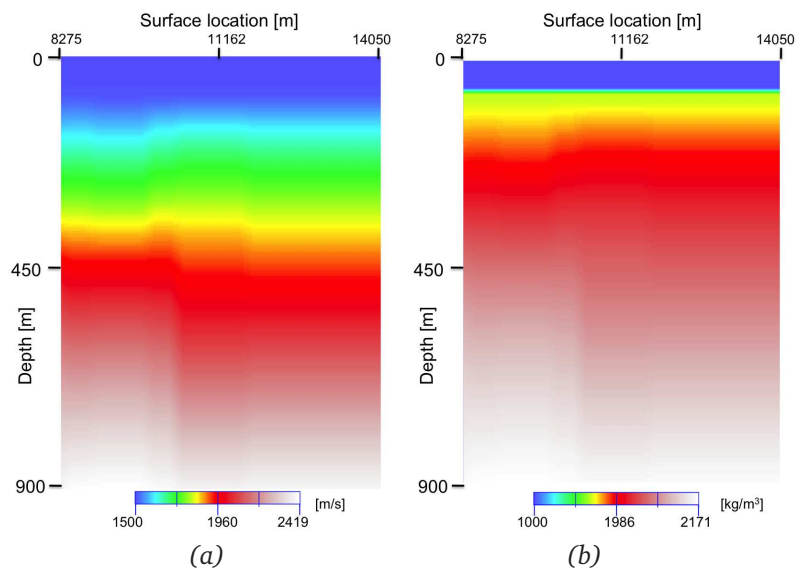


Figure 6.5 (a) Initial velocity model [m/s] built from migration-velocity analysis and well information. (b) Initial density model [kg/m^3] derived from the interval velocities using Gardner's-Gardner's empirical relations.

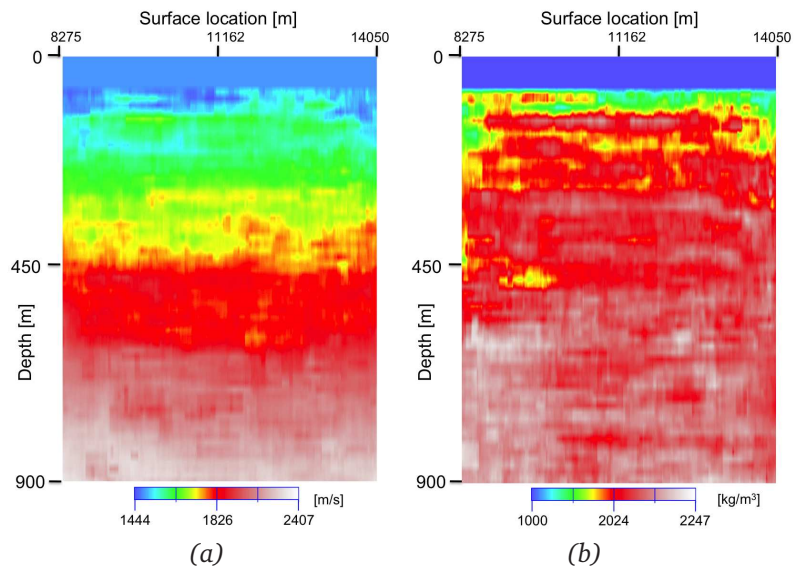


Figure 6.6 Result of nonlinear full-waveform inversion via the GA using a 12.5m grid. (a) Estimated effective velocity model [m/s]. (b) Estimated effective density model [kg/m^3].

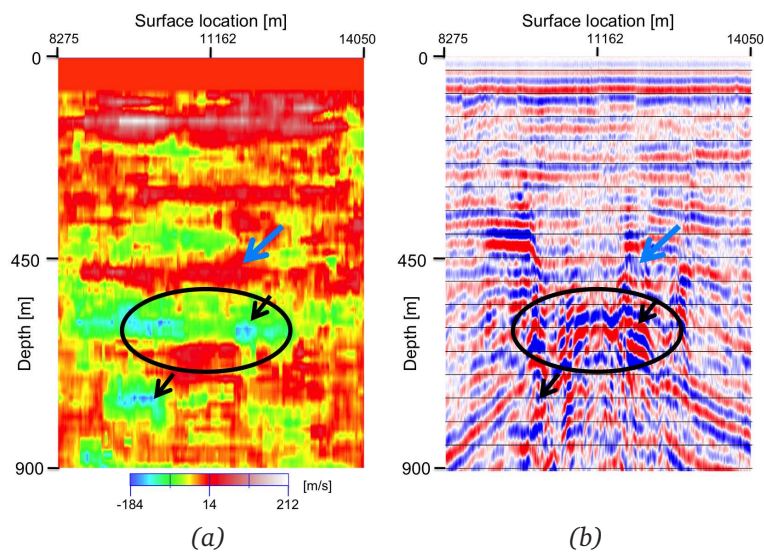


Figure 6.7 (a) Difference between the estimated effective velocity model [m/s] and initial model (Figures 6.5a and 6.6a). (b) is the lowpass-filtered prestack image converted to depth. The black ellipse denotes the gas cloud area and the black arrows point at the low-velocity zone. Blue arrows indicate a high-velocity layer associated with the geological unconformity.

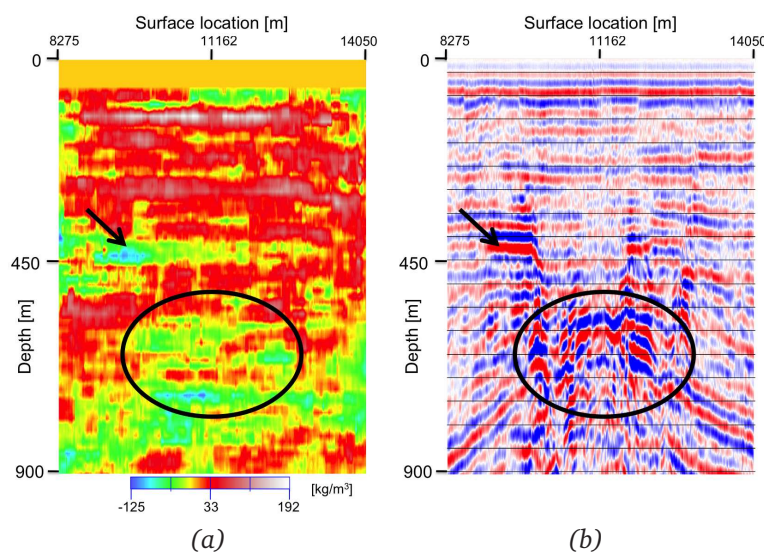


Figure 6.8 (a) Difference between the estimated effective density model [kg/m³] with respect to the initial model. (b) is the lowpass-filtered prestack image converted to depth, where the ellipse denotes the gas cloud area. The black arrow points at a low-density zone of possible shallow gas.

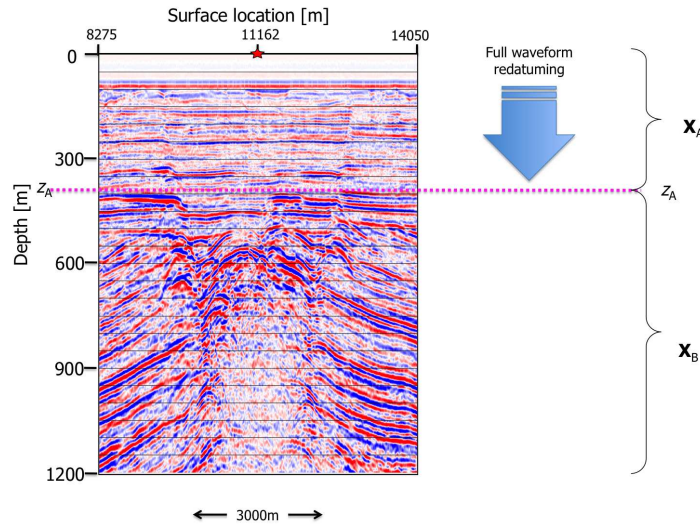


Figure 6.9 Schematic diagram showing the depth at 400m where the new virtual sources and receivers are placed after redatuming. The 400m of zone X_A is chosen just above the gas cloud area.

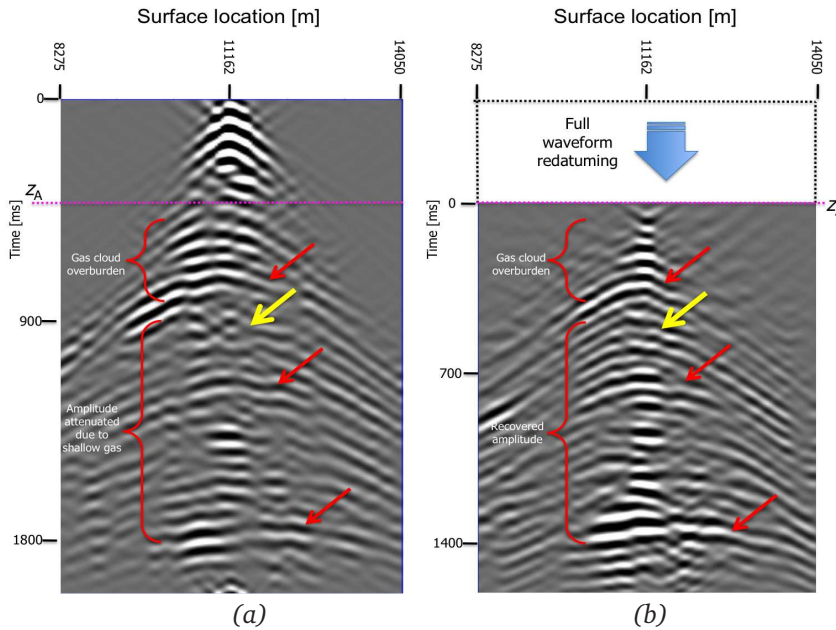


Figure 6.10 (a) Shot record taken in the middle of the seismic line with a source above the gas cloud area. (b) Shot at the same location after full-waveform true-amplitude redatuming. The arrows point at the reflections that are enhanced after the full-waveform transmission deconvolution process.

a low-velocity area that is consistent with the geology. Blue arrows in Figure 6.7 indicate a high-velocity layer associated with the geological unconformity that separates younger sediments from older sediments. Figure 6.8a shows the difference of the estimated effective-density model with respect to the initial model and Figure 6.8b repeats the depth image of Figure 6.7b. Again, the black ellipse denotes the low-density area of the gas cloud. The black arrow suggest the possibility of the shallow gas (with low density) in the area above the gas cloud.

As stated in the introduction, because of its inherently 3D nature, good 2D redatuming results cannot be expected below the actual gas cloud area. However, the overburden up to 400m appears more layered and still shows large contrasts as shown in Figures 6.7 and 6.8 (up to $\pm 200m/s$ and $\pm 200kg/m^3$). Therefore, we apply the full-wavefield redatuming for the depth level at 400m. The final nonlinear full-waveform inversion estimated effective model (Figures 6.6a,b) is used to forward-model the full-waveform transmission operators. The sources of these transmission operators were located at the surface while the virtual receivers are placed at 400m depth, as shown in Figure 6.9. Next, the forward-modeled full-waveform transmission operators were inverted to obtain full-waveform transmission-deconvolution operators.

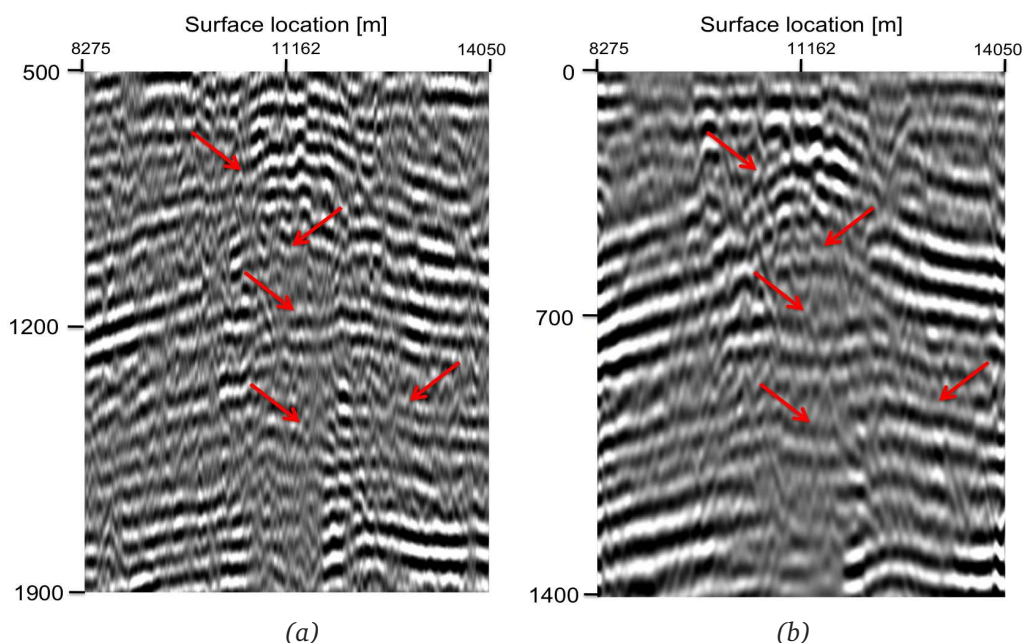


Figure 6.11 (a) Real marine 2D data section from the Malay basin resulting from prestack time migration. Note the influence of the low-velocity anomaly and poor quality of the reflections underneath the gas cloud as indicated by the red arrows. (b) Stack section from the estimated response X_B obtained after full-waveform transmission correction. Note the enhanced reflections. The redatum depth level is at 400m.

Figure 6.10b shows a single shot record from the center of the survey area after the application of the true amplitude, full-waveform redatuming. There is a reduction of the overburden transmission imprint indicated by the yellow arrow in Figure 6.10b which shows recovered reflectors underneath the gas cloud. Figure 6.11a shows a prestack time-migrated section response obtained from the surface data. Note the influence of the low-velocity anomaly on this time section resulting in delay times and poor quality of the reflections underneath the gas cloud. Figure 6.11b displays the result after the true-amplitude redatuming, followed by conventional normal-moveout correction and stack. Note that the amplitudes of the target horizons, indicated by the red arrows, are recovered and the transmission codas are reduced. Overall the stack after the full-waveform redatuming shows better and more continuous reflections.

7

Discussions and recommendations

7.1 Discussions

7.1.1 Crosscorrelation versus deconvolution redatuming for high-contrast heterogeneous media

In this thesis we have discussed the redatuming of seismic data through a heterogeneous overburden. For this full-waveform redatuming process the forward-propagation operator \mathbf{W} , which describes wave propagation between the datum level and the acquisition surface, needs to be removed from the data. This can be achieved by calculating the inverse of this operator and applying it to the seismic measurements, both on the source side and the receiver side.

The inverse propagation operators can be approximated by:

1. the conjugate transpose of the operator \mathbf{W}^H (H denotes the Hermitian), or
2. the actual inverse of the propagation operator, \mathbf{W}^{-1} , usually calculated as a least-squares inverse (see Section 3.1.3).

In a smoothly-varying medium \mathbf{W}^H is approximately equivalent to the inverse of the transmission operator \mathbf{W}^{-1} . However, in strongly-heterogeneous media they can be very different. The drawback of using the deconvolution method, i.e. using the actual inverse \mathbf{W}^{-1} , is that it creates artifacts because the inverse is sensitive to zeroes in the spectrum of the estimated

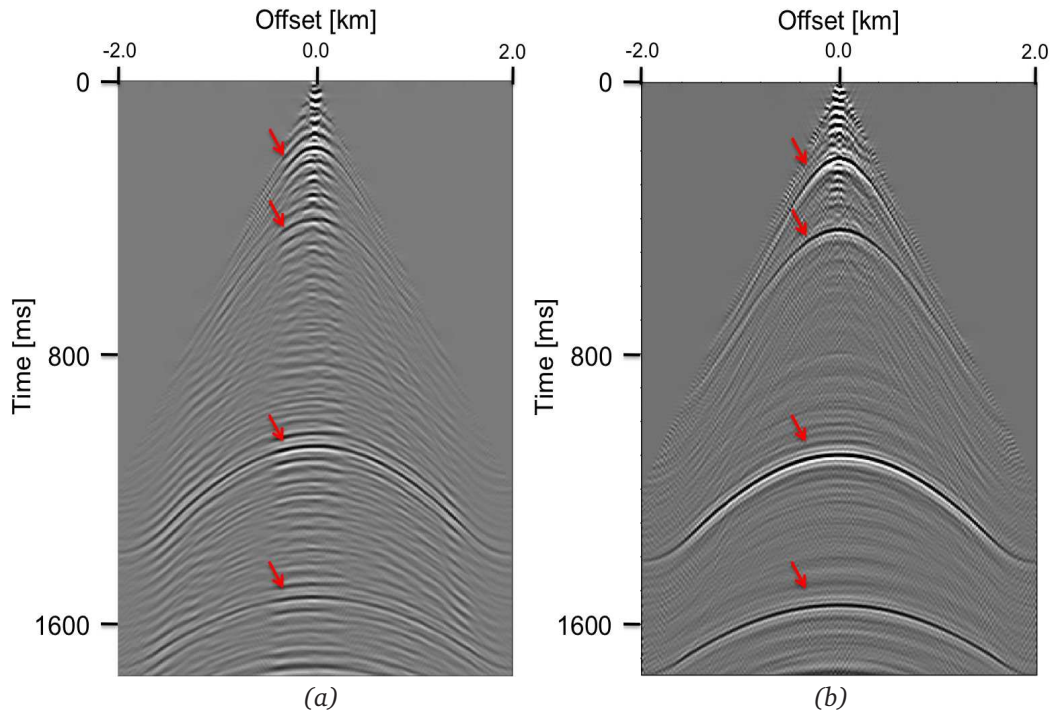


Figure 7.1 Full-waveform true-amplitude redatuming of shot records based on (a) the Hermitian operator (b) the deconvolution operator. The red arrows indicate the four reflectors of \mathbf{X}_B .

operator. As with conventional deconvolution, this can be controlled by the addition of a stabilization constant (ϵ in Equation 3.6).

In a moderately-inhomogeneous medium, the traveltimes are calculated using an eikonal-solver or ray tracing with the assumption of maximum energy or the shortest ray-path. The accuracy of these Green's functions is more dependent on the accuracy of the velocity model than on the reflectivity model.

For a strongly-heterogeneous medium, such as a gas cloud, in order to achieve true-amplitude redatuming, we have to use full-wavefield operators that include all transmission effects, including the coda. The accuracy of the amplitude response of the reflectors from below the gas cloud therefore in turn depends on the accuracy of the inverse of these operators.

Figures 7.1 and 7.2 show a comparison of using the crosscorrelation (Hermitian) and deconvolution operators for transmission operators modelled from the true medium. Although we are using the true property model to calculate the transmission operators, the Hermitian operator (Figure 7.1a) does not succeed in recovering the reflectors (\mathbf{X}_B) underneath the heterogeneous overburden as well as the deconvolution result (Figure 7.1b). Figure 7.2a shows that after applying NMO and stack, although the kinematics are corrected for, the am-

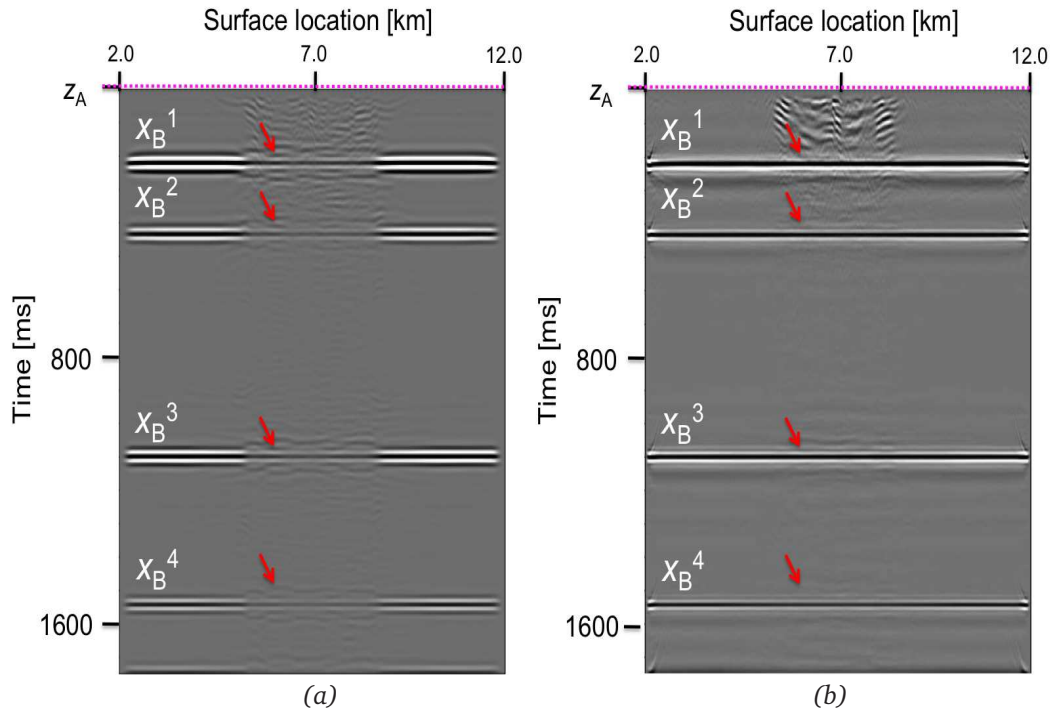


Figure 7.2 Stack sections of the redatumed shot records in Figure 7.1 for (a) Hermitian redatuming operator (b) deconvolution redatuming operator.

plitude underneath the gas cloud could not be recovered properly using the crosscorrelation method. Figure 7.2b shows that reliable amplitudes are obtained with the deconvolution approach.

7.1.2 Layer-stripping redatuming

In Equation 3.2 of our formulation, the depth level z_A beneath the gas cloud is chosen arbitrarily. Typically, in a gas field area, below the gas cloud overburden multiple hydrocarbon reservoirs are located. In many areas with shallow gas clouds, there are many multiple hydrocarbon reservoirs beneath the gas. In this case, there is a question as to where z_A should be located. In this regards, \mathbf{X}_A can be taken to be the region that captures the full wavefield of the gas cloud reflection response above it. This is then acts as an overburden for the reflectors below. We can therefore devise a strategy where several overburden layers are corrected in a recursive manner using a layer-stripping procedure.

For example, we have shown in our 2D real marine field data application (see Chapter 6), that the shallow sediments in the area 0 – 400m already acted as a first complex overburden. After full-waveform redatuming to 400m, we remove effect of the shallow overburden, are

left with a simpler wavefield that only has the gas cloud below as the overburden. As shown in Figure 6.11b this first full-waveform redatuming step help define the geometry of the gas cloud, as well as the deeper reflections.

It follows that a viable strategy for handling complicated overburden of this kind is to unwind the complex-propagated wavefield scattered by the overburden into a simpler wavefield by recursively removing its effect layer by layer. The advantage of this approach is that the full nonlinear inversion problem is divided into a few smaller ones. It may produce a better true-amplitude seismic image of the reservoirs.

7.1.3 Land near-surface problem

In principle, our inversion/redatuming approach should also be applicable to the complex near-surface problem that often occurs in land data. However, the gas cloud situation is different from the typical land near-surface problem. In particular, we measure the gas cloud reflection response and this allows the response to be inverted for an effective gas-cloud model. By contrast, in land seismic data, the reflection response of the near-surface heterogeneities is not usually (properly) measured. Therefore, the near-surface problem requires a different approach, such as that described by Kelamis et al. (2002).

7.2 Recommendations

7.2.1 3D implementation

We know that subsurface geology is three dimensional, hence to fully measure the wavefield and image the subsurface requires 3D measurements, 3D methodologies and 3D algorithms. It is known that gas clouds are highly heterogeneous and scatterer energy in all directions. Therefore, the only way to handle this properly is with a full 3D implementation of the described methodology. Although the algorithm described in Section 3.1.1 - 3.1.3 is in principle is already 3D, we have shown results of 2D implementations in Chapter 5.3 and Chapter 6, which are promising.

The biggest issue in 3D marine acquisition is the sampling issue of a 3D wavefield. Typically the receiver sampling in the inline direction is better than the sampling in the crossline direction. 3D full-waveform redatuming requires a 3D effective model, forward modeling the 3D full-waveform transmission operators and redatuming in a full 3D sense. Consequently, obtaining a 3D effective model requires 3D full-waveform inversion. Note that a full 3D redatuming is not straightforward (Tegtmeier et al., 2004). Perhaps an easier route to implement such redatuming/imaging strategy is by incorporating the 3D transmission operator correction in Reverse-Time-Migration (*RTM*). This is discussed in Section 7.2.5.

7.2.2 Elastic solution

Since the earth is elastic, in order to achieve full-wavefield true-amplitude imaging underneath the gas cloud, we have to measure the total wavefield not only in 3D but also address its elastic nature. Furthermore, the full-waveform inversion process needs to be extended to the full elastic case to get an effective elastic medium. This is possible and several studies have already been done on elastic full-waveform inversion (see Sears et al., 2008; Sirgue et al., 2010). With an elastic full-waveform inversion process, elastic effects especially amplitude variations with offset and mode converted events within the gas-cloud region can be taken into account. The elastic parameters contain vital information not only on the rock matrix but also on the density and associated fluid. The most important requirement for elastic waveform inversion is to use an elastic forward modeling engine. The obtained elastic full-waveform transmission operators will provide a more accurate true-amplitude full-waveform redatuming result.

7.2.3 Anelastic solution - incorporating attenuation

One of the issue is the incorporation of true attenuation. We refer back to some observations made earlier in this thesis. We stated that what is often referred to as ‘absorption’ is mainly a complex wave propagation phenomenon. Although some energy may dissipate into heat (anelastic loss), we believe that a large part of the energy is lost in elastic mechanisms (internal scattering, multipathing etc.), and can in principle be corrected for. If anelastic losses (i.e. true absorption) do occur, they can be accounted for as a secondary process in the inversion, by allowing the effective velocity parameters to become complex-valued. This should account for squirt flow mechanisms at a macroscopic level and also effectively describe anelastic effects due to microscopic details such as gas bubbles and very fine heterogeneous layering of sediments.

Virieux and Operto (2009) propose to incorporate complex-valued velocity $v(x)$ in the medium properties using the Kolsky-Futterman model with a linear frequency dependence of the attenuation coefficient:

$$v(x) = \frac{1}{c^2} \left[1 - \frac{2}{\pi Q} \log(f/f_r) + \frac{i}{Q} \right], \quad (7.1)$$

where $v(x)$ is the complex-valued velocity in a constant-density visco-acoustic medium with a propagation velocity c , quality factor Q and reference frequency f_r . Also, Mulder and Hak (2009) propose to include a similar kind of approach using a complex-valued velocity.

In this way damping is included as a simple extension of the acoustic theory by introducing extra parameters specifically by including the imaginary parts of the observed propagation properties, or by fixing f_r and introducing Q as an extra parameter.

7.2.4 Other full-waveform inversion methodologies

In this thesis the Genetic Algorithm is used to solve the nonlinear inversion problem. However, we do not claim that this is the best approach for this problem. Like all methods it has its pros and cons:

- The advantages of the GA approach are:
 - it is relatively easy to program;
 - it can in principle solve a very nonlinear problem i.e. it can escape from local minima;
 - it is easy to incorporate different parametrization strategies;
 - it is easy to include different norms and penalties/constraints in the objective function;
 - it can provide an ensemble of solutions that could be used for statistical analysis.
- The disadvantages of the GA approach are:
 - every possible parameter solution requires forward modeling, which is expensive in the 2D (or 3D) case;
 - convergence is very slow, it will not easily find the true minimum;
 - multidimensional-inversion (with many parameters) may become inefficient;
 - heuristic approaches such as GA always need fine-tuning in the parameter settings.

Alternatively, full-waveform inversion using finite-difference modeling in combination with conjugate-gradient inversion schemes (see Virieux and Operto, 2009) is currently a very active area of research. However, it carries its own advantages and disadvantages.

- The advantages of a conjugate-gradient nonlinear inversion are:
 - the forward modeling is performed only a few times per iteration;
 - more effective updating is achieved if the nonlinearity is small i.e. in low-contrast media.
- The disadvantages of a conjugate-gradient inversion scheme are:
 - it is cumbersome and complicated to implement, especially in a parallel-computing environment;
 - different penalty functions and parameterizations are not easily implemented in the objective function calculation;
 - the inversion process can become unstable at higher frequencies and very large medium contrasts.

In order to make this full-waveform inversion viable, full-waveform inversion currently inverts very low frequencies typically in the range of 2 to 7Hz, due to limitations in the finite-difference modeling implementations (see Virieux and Operto, 2009). These frequencies are not normally recorded in conventional seismic data acquisition. However, Sirgue et al. (2010) recently presented results of full-waveform inversion of a marine 3D OBC dataset. They performed the seismic modeling in the frequency domain with a multidimensional iterative solver. Also, Plessix et al. (2010) performed full-waveform inversion on land data with frequencies down to 1.5Hz. Note that most current low-frequency inversion approaches do not aim for an accurate subsurface properties model, but only at getting an accurate velocity model for prestack depth migration.

Perhaps a more suitable solution is by using a hybrid optimization strategy with a combination of a gradient method and the GA. For example, we can use the GA to find the global effective medium, i.e. a solution close to the global minimum, and then using the gradient method to fine-tune the solution to find the true minimum.

As an alternative, we can use scattering theory (see Abubakar et al., 2005; Gisolf and Verschuur, 2010) where the frequency range is not limited by fundamental considerations. In the scattering theory, the total wavefield P_{tot} is the sum of incidence P_{inc} and scattered P_{sct} wavefields.

$$P_{tot} = P_{inc} + P_{sct}. \quad (7.2)$$

where κ is the true medium compressibility and χ is the normalized difference of the two media:

$$\chi_{\kappa} = \frac{\kappa - \kappa_0}{\kappa_0}. \quad (7.3)$$

The wavefield P_{sct} is the response from the medium contrasts (χ) against the background medium compressibility κ_0 .

From Fokkema and van den Berg (1993), the scattering integral equation for the total wavefield is:

$$P_{sct}(\vec{x}_r, \vec{x}_s; \omega) = -\omega_0^2 \int_V G(\vec{x}_r, \vec{x}'; \omega) \chi(\vec{x}') P_{tot}(\vec{x}_r, \vec{x}_s; \omega) dx' \quad (7.4)$$

and

$$P_{tot}(\vec{x}_r, \vec{x}_s; \omega) = P_{inc}(\vec{x}_r, \vec{x}_s; \omega) - \omega_0^2 \int_V G(\vec{x}_r, \vec{x}'; \omega) \chi(\vec{x}') P_{tot}(\vec{x}_r, \vec{x}_s; \omega) dx'. \quad (7.5)$$

For small contrasts, χ , or low frequencies, Equation 7.5 can be solved via linearisation (Born approximation) where we assume that the incidence wavefield is much stronger than the scattered wavefield, so $P_{tot} \approx P_{inc}$ and $P_{inc} \gg P_{sct}$. The integral equation is then linear in the wavefield P . For high-contrast media, Equation 7.5 states that the total wavefield P_{tot} is nonlinearly-related to the medium contrasts χ .

To solve Equation 7.5, we first assume that $P_{tot} = P_{inc}$. When the scattered data have been measured in a data domain, Equation 7.4 can be solved to get the value of initial χ . This

value can then be used as the input for Equation 7.5 to get a new P_{tot} which can then be fed back into the Equation 7.4.

Note that the Green's functions (G) and the incident wavefield (P_{inc}) always propagate in the background medium and that the scattering of the wavefield is only due to the medium contrasts. The advantage of this approach is that large contrasts can be handled properly although this increases the number of iterations that are required.

7.2.5 Including transmission compensation in Reverse Time Migration

Seismic imaging algorithms such as Kirchhoff PreSDM, one-way wave-equation migration, or Reverse Time Migration, require an accurate velocity model. The Kirchhoff migration algorithm has difficulties with multipathing, but can handle dips more than ninety degrees. By contrast, the one-way wave-equation migration can handle multipathing but cannot image beyond ninety degrees. The Reverse-Time-Migration (*RTM*) can handle both multipathing (multiarrivals) and dips more beyond ninety degrees, including turning waves.

Conventional Kirchhoff migration traveltimes tables calculated using either solutions of the eikonal equation or geometric ray tracing. However, eikonal solvers are insufficiently inaccurate in high-contrast media. One can also opt for maximum energy in the eikonal solver for the travel-time calculation, but this still cannot handle the multipath effects of the wavefield. Similarly, in geometrical ray tracing, a lot of rays are lost and are not recorded at the surface. In high-contrast heterogeneous media this is due to the fact that most rays travel along the shortest ray-paths and try to avoid low-velocity regions or very large contrasts.

Two-way wave-equation migration methods such as *RTM* (see Baysal et al., 1983; Baysal et al., 1984; Levin, 1984; Robein, 2003; Jones, 2008) use the full two-way wave equation for the propagators. This means they calculate the full wavefield from the source and receiver positions at the surface to every depth level. These wavefields also contain multipathing, multiple scattering and diving waves. *RTM* first applies the forward-propagation operator from the source ($\mathbf{W}^+S^+(\omega)$) to the image level and by reversing the time of the data and then feeding it back into the finite-difference algorithm it performs the back propagation from the receivers to the image level.

RTM can handle turning waves and dips beyond ninety degrees if the target is illuminated by turning waves. The drawbacks of *RTM* are *i*) it is computationally very expensive and to make it viable, migration is normally limited to only low frequencies and a coarse forward-modeling grid, and *ii*) boundary conditions such as absorbing boundaries at the edge of the computational domain need be incorporated to avoid artifacts.

The imaging condition of reverse time migration can be applied as crosscorrelation of the incident source wavefield and the back-propagated receiver wavefield, applied as zero lag as a function of space and summed over all the sources (Biondi and Shan, 2002).

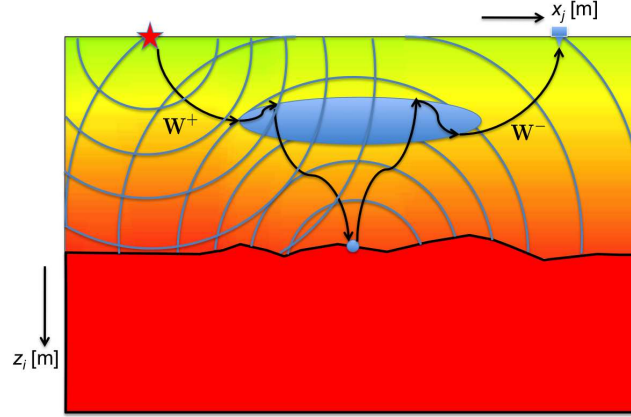


Figure 7.3 Schematic diagram of the downgoing propagation of the source wavefield (W^+) and the upgoing propagation of the receiver wavefield (W^-) shown by the blue curves. The solid black curves depict the ray-paths of the two wavefields.

Figure 7.3 illustrates the forward-propagating source wavefield and scattered wavefield recorded by the receiver.

The acquired seismic wavefield at the surface can be written as a sum of reflected events:

$$\mathbf{P}^-(z_0, z_0) = \sum_{d=1, \dots, m} \mathbf{W}^-(z_0, z_d) \mathbf{R}(z_d, z_d) \mathbf{W}^+(z_d, z_0) \mathbf{S}(z_0, z_0). \quad (7.6)$$

For *RTM* in a low contrast inhomogeneous medium, we can apply crosscorrelation imaging condition such that:

$$\text{diag}\{\mathbf{R}(z_d)\} \approx \sum_j \sum_{\omega} \text{diag} \left\{ (\mathbf{W}^H \vec{P}_j^-) (\mathbf{W} \vec{S}_j^+)^T \right\}, \quad (7.7)$$

where the diagonal elements of \mathbf{R} contain the angle-averaged reflection coefficients at depth z_d and j is the shot record index (see Berkhout, 1982).

If we include the estimated gas cloud model in *RTM*, only the source is correctly forward-propagated while for the receiver *RTM* still effectively uses \mathbf{W}^H . If we want to remove the wavelet from the data and compensate for geometrical spreading in the background medium in *RTM*, we need to apply a deconvolution-type imaging condition. In that case we should precondition the whole recorded wavefield \mathbf{P} with $\frac{1}{\mathbf{W}^H \mathbf{W}^- + \epsilon^2 \mathbf{I}}$ before the application of the reverse-time-migration process. Equation 7.7 then becomes:

$$\text{diag}\{\mathbf{R}(z_d)\} \approx \sum_{\omega} \text{diag} \left\{ \mathbf{W}^H \left[\frac{\mathbf{W}^-}{\mathbf{W}^H \mathbf{W}^- + \epsilon^2 \mathbf{I}} \right] \mathbf{P}^- [\mathbf{W}^+ \mathbf{S}^+(\omega)]^{-1} \right\}. \quad (7.8)$$

Equation 7.8 shows that the transmission compensation in *RTM* is similar to our full-waveform transmission redatuming. However, in *RTM*, this deconvolution needs to be applied at each depth level.

It is worth noting that the velocity model from full-waveform inversion of the gas cloud reflections can be used as in full two-way wave-equation migration such as *RTM*, even if the deconvolution imaging condition is not used. This velocity model is more accurate since it fully explains the kinematics of the propagating wavefield, but not the dynamics. Examples of a migration of this kind is shown by Sirgue et al. (2010) where the migrated image is more focused and the kinematics are better-resolved.

7.2.6 Wavefield replacement operators

The result of full-waveform transmission deconvolution of the total data \mathbf{P} is a dataset that is redatumed to a datum z_A (see Figure 3.1). A seismic interpreter usually prefers a full seismic section that has seismic information from the acquisition datum down below the exploration target. In order to ‘forward propagate’ the data from the redatum level back to its acquisition datum using a notional model which does not have the gas cloud in the overburden, we propose applying a wavefield replacement operator.

After full-waveform redatuming we have:

$$\hat{\mathbf{X}}_B S^+(\omega) = (\mathbf{W}^-)^{-1} \mathbf{P}_{0_B}^- (\mathbf{W}^+)^{-1}. \quad (7.9)$$

We can forward extrapolate this result back to the original datum with a replacement operator, \mathbf{W}_{repl} , that does not contain the gas cloud:

$$\hat{\mathbf{P}}_{0_B}^- = \left(\mathbf{W}_{repl}^- (\mathbf{W}^-)^{-1} \right) [\mathbf{P}_{0_B}^-] \left((\mathbf{W}^+)^{-1} \mathbf{W}_{repl}^+ \right), \quad (7.10)$$

By determining the difference operator $\delta\mathbf{W} = \mathbf{W}_{repl} \mathbf{W}^{-1}$, and remembering that $\mathbf{P}_0^- = \mathbf{X}_A S(\omega) + \mathbf{P}_{0_B}^-$, we can write:

$$\hat{\mathbf{P}}_{0_B}^- = \delta\mathbf{W}^- [\mathbf{P} - \mathbf{X}_A S(\omega)] \delta\mathbf{W}^+, \quad (7.11)$$

where $\hat{\mathbf{P}}_{0_B}^-$ is the new replacement wavefield as from which the gas-cloud propagation imprint has been removed. It is optional to remove $\mathbf{X}_A S(\omega)$ from the total data \mathbf{P} since it is mapped to anticausal (negative time), but after replacement it will be mapped back to positive times again. However, the replacement process will not treat the response of layer *A* correctly.

7.2.7 Application generalizations to other complex geological problems

Finally, it needs to be stressed that the methodology proposed in this thesis is not restricted to the gas-cloud situations and can be generalized to other complex geological problem such as shallow-salt structures or basalt layers. Any localized heterogeneity in the overburden that has a severe imprint on the reflections from below can be treated in the same way as long as the full-wavefield contains the multiple-scattering energy is recorded and sample adequately.

8

Conclusions

This thesis has considered the situation of a heterogeneous overburden such as a gas cloud, its effect on seismic wave propagation and related imaging problems. We discussed current solutions to mitigate and solve the imaging problem in terms of solving the kinematics as well as the dynamic issues of the gas cloud imprints.

In this thesis we propose to solve the problem of seismic imaging below gas clouds via a full-waveform inversion strategy that consists of the following steps:

1. performing nonlinear full-waveform inversion on that part of the seismic data that contains the gas cloud reflections, for its effective-medium properties;
2. forward modeling the full-waveform transmission operator of the effective medium;
3. calculating the inverse of the transmission operators via least-squares inversion;
4. applying the inverse transmission operators to the seismic data to get full-waveform redatumed data.

For the 1.5D case we have demonstrated that the transmission operators are invertible from the reflection response of the gas-cloud area via a nonlinear full-waveform inversion method. Although some of the imperfections translated into deconvolution noise, the target reflections events can be recovered very well from the transmission coda. For this 1.5D situation it was demonstrated that this full-waveform inversion process can provide an effective model of the gas cloud from which the required full-waveform transmission operators can be derived.

The positive results of the inversion for the 1.5D case opened the door for extending the target-oriented inversion process to the 2D (and potentially 3D) situation. Furthermore, using a 2D forward-modeling experiment, in which true gas-cloud properties were known, it was demonstrated that a full-waveform deconvolution approach could reconstruct the reflection response below a 2D gas cloud anomaly, such that the complex transmission imprint is properly removed.

For the realistic situation, the medium properties in the gas cloud are unknown, we have shown that the complexity of the wavefield propagated through the gas cloud is invertible via a multidimensional nonlinear full-waveform inversion process using a Genetic Algorithm. The Genetic Algorithm, together with blended acquisition and a frequency marching approach, was able to get an effective model of the gas cloud from the gas-cloud reflection response, both for a 2D synthetic example and for a 2D subset of a field dataset. Note that the gas cloud situation is different from the typical land near-surface problem: usually we properly measure the gas cloud reflection response; this provides the possibility of inverting this response for an effective gas cloud model. In land data, usually the near-surface reflection response is not well measured.

For the 2D numerical dataset, we recovered a good reconstruction of the model properties via nonlinear full-waveform inversion. Redatuming the seismic data using the full-waveform transmission operator obtained from effective-medium models, successfully recovered primary reflections from underneath the gas cloud.

In a real 2D marine dataset, we inverted for the effective-medium describing the first 400m of the subsurface and applied the full-waveform redatuming process. There are many effects that could have limited the accuracy of the final result, such as the 3D geometry effects of the gas cloud body itself, mode conversion, the source estimation, limitations in the forward modeling (such as low-frequency requirements and high-frequency limitations), inversion instability and 3D surface-related multiples. Nevertheless, the result after the 2D true-amplitude redatuming showed that the amplitudes of the target horizons were recovered and the transmission codas were reduced. The stack after the full-waveform redatuming displayed overall better and more continuous reflections.

Inverting real data via full-waveform inversion is still a topic of ongoing research. Solving the inversion for the multiple scattering in a high-contrast heterogeneous medium still poses mathematical and practical problems. Current full-waveform solution via stabilized Born inversion can only cater for small contrasts. Ideally, a full-wavefield inversion that includes visco-elastic and anelastic effects would be preferred.

The results of this research has confirmed our belief that what is often referred to, as ‘absorption’ can to a large extent be attributed to a complex wave-propagation phenomenon. Although some energy really may disappear into heat (anelastic loss), we believe that a large part of the energy is scattered in elastic mechanisms (internal scattering, multipathing etc.) and is, therefore, recoverable by full-waveform deconvolution. For the case that anelastic losses (i.e. true absorption) contribute to the amplitude decay, this could be included in our inversion strategy by making the effective velocity parameters complex-valued. We believe

a large part of the observed attenuation effects is due to complex wave-propagation rather than anelastic losses, especially in cases where the gas cloud has a localized shape with limited thickness both of which can in principle be corrected for. This is what we addressed in this thesis.



Data-driven imaging for heterogenous media via automated nonhyperbolic focusing operator estimation

A.1 Summary

In Malaysian basins, offshore Malaysia, there are many imaging problems related to the so-called gas clouds or gas chimneys. Conventional imaging processes do not offer satisfactory solutions, because of the complex propagation effects that occur. The involved simplified Green's functions that are used in these algorithms do not properly describe the kinematics as well as the dynamic behavior of the actual visco-elastic wave propagation. The proposed method in this appendix aims at solutions beyond the traditional imaging approaches. The focusing of the wavefield is addressed via the so-called Common Focus Point (*CFP*) method, where the estimation of a velocity-depth model is deferred as much as possible. This method will be augmented by an automated focusing operator estimation process, in which the focusing operator parameterization allows nonhyperbolic and non-symmetric one-way travel time functions. In this way an optimum focusing of the energy below the anomaly is obtained. As a demonstration, a synthetic dataset with a complex, low velocity anomaly was generated. The *CFP* imaging approach has contributed significantly toward the improvement in reflector continuity and amplitude restoration. Finally, results on a field dataset confirm the viability of the approach.

A.2 The Common Focus Point (CFP) Method

Heterogeneous media, such as the ones that contain gas clouds, yield problems in the migration velocity analysis process. Due to the localized nature of the velocity anomaly, it imposes problems in the parameterization of the velocity model. Therefore, the Common Focus Point (CFP) methodology may provide a solution.

The technology was proposed and described in detail by Berkhout (1997a,b) and Thorbecke (1997). The key element in this methodology is the focusing operator, which is a one-way travel time function between one point in the subsurface and all acquisition points at the surface. With such a focusing operator, the imaging of one point in the subsurface is fully described, as imaging involves the removal of the one-way travel time from each seismic source to the chosen subsurface point and the removal of the one-way time from that point to the receiver locations.

Therefore, a focusing operator can also be called migration operator and actually corresponds to a time-reversed Green's function (i.e. a point source response with a source in the subsurface and measurements at the acquisition surface). Traditionally, these migration operators are obtained via a velocity-depth model, which is estimated by iteratively migrating the seismic data and checking the so-called image gathers (Stork, 1992). However, this involves decisions on the parameterization of the velocity-depth model at forehand and also involves several expensive migrations. Therefore, Berkhout (1997b) proposed an alternative in which these focusing operators are directly estimated from the seismic data, without involving the translation into a velocity-depth model. The one-way travel times functions are directly extracted from the seismic data via a focusing analysis.

A central role in this methodology is played by the CFP gather. This is a virtual receiver response that is created from the surface seismic data by a refocusing process: the seismic receivers at the surface are translated into a virtual receiver (i.e. a buried receiver) at a reflecting boundary, whereas the sources are still at the original surface locations. This refocusing is possible via the Rayleigh (II) integral (see e.g. Berkhout, 1982):

$$P(x_A, y_A, z_A; \omega) = 2j\omega \rho \iint_{-\infty}^{\infty} dx dy P \left[\frac{\gamma}{\rho} \left(\frac{\partial t_G}{\partial z} \right) \right] e^{j\omega t_G}. \quad (\text{A.1})$$

where z denotes depth, x and y are spatial locations, and $P(x_A, y_A, z_A; \omega)$ is the new extrapolated pressure wavefields at CFP location and depth A , based on measurements along the surface. The Green's function can be approximated by using the direct travel time from point A to the receivers (t_G) where it actually describes a one-way travel time between the surface location and point A , i.e. this is the focusing operator. The gamma (γ) is an amplitude factor that typically compensate for the geometrical spreading involved in propagation.

If this process is applied to each shot record, then each shot provides one trace in a virtual receiver gather. By applying reciprocity, this virtual receiver gather can also be interpreted as a virtual source gather, i.e. the response of a virtual source at the reflecting boundary

measured by receivers at the surface. Thus, the process to build one *CFP* gather is to delay the traces of one shot record according to the focusing operator, apply amplitude weights according to Equation A.1 and sum all these traces, producing one trace per shot in a *CFP* gather. If many shot records across the acquisition surface locations are used, a complete *CFP* gather for one subsurface location at the reflecting boundary is obtained. Note that a *CFP* gather can also be interpreted as a (reciprocal) walk-away VSP measurement: one source in the subsurface and many receivers at the surface. Thus, this *CFP* gather will also contain the direct wave response of the considered reflection point, which again describes the one-way travel times.

When the correct focusing operator was used to construct the *CFP* gather, then the *CFP* gather should give a reflection event at exactly the same one-way travel times. Any error in the involved focusing operator yields a deviation of the resulting reflection event in the *CFP* gather. By comparing the focusing operator and the time of the corresponding arrival in the *CFP* gather, a validation of the focusing operator is obtained. Berkhout (1997b), Thorbecke (1997) and Bolte (2003) have exploited this mechanism to iteratively update initial focusing operators that are based on the local NMO velocity. A key role in this process is played by the Differential Time Shift (*DTS*) panel, which is a *CFP* gather, time-corrected for the involved focusing operator. When the operator is correct, the *DTS* panel will show a horizontal reflection event at zero differential time for all *CFP*-offsets. An erroneous operator will result in an event that is not at zero differential time for all *CFP* offsets, indicating that an update of the focusing operator is required.

A.3 CFP implementation

The main feature of the *CFP* technology is that the focusing operators are estimated from the data without estimating the corresponding velocity model. One-way travel times are inherently simpler than two-way travel times, allowing simple and efficient parameterizations as illustrated in Figure A.1. With such a focusing operator, the imaging of one point in the subsurface is fully described, as imaging involves the removal of the one-way travel time from each seismic source to the chosen subsurface point and the removal of the one-way time from that point to the receiver locations. Conventional travel time calculation methods often adopt simplified analytical Green's Function (hyperbola) or use an eikonal solver or ray tracing, which often are not sufficient to achieve proper focusing. For the method in this paper, we propose a flexible focusing method, which allows propagation through heterogeneous layers in an automated manner by data-driven estimation of one-way focusing operators beyond the traditional restricted parameterization and without the need of determining the velocity-depth model.

A.4 Estimation of focusing operators by global inversion

A few authors have already demonstrated the basics and initial results with this methodology for the complex near surface problem. Hindriks and Verschuur (2001) propose a redatuming procedure similar to procedures described by Shtivelman and Canning (1988) and Berryhill (1979), involving a multitrace stack over high frequency Green's operators. However, the conventional wave equation redatuming methods described by Shtivelman and Canning (1988) and Berryhill (1979) explicitly require a velocity model of the near surface. Often, the near surface contains complexities, which can hardly be taken into account in any model estimation procedure, thus affecting the resolution of the final redatuming results. In work by Bolte and Verschuur (1998) and Hindriks and Verschuur (2001), travel time operators (representing Green's functions) are derived in a data-driven way, based on the *CFP* technology as described by Berkhout (1997a); Berkhout (1997b) and Thorbecke (1997) and, therefore, avoid the explicit use of a near surface model. Kelamis et al. (2002) demonstrated the procedure successfully on synthetic and real data. To appreciate the depth and secondary receiver locations after redatuming, a travel time inversion process such as described by Cox and Verschuur (2001) can be applied to the obtained operators. This will result in an estimated velocity-depth model for the area above the datum reflector, including the location of the focal points along the datum (see also Al-Ali and Verschuur, 2006).

In this paper we will expand on the work of Verschuur and Marhfoul (2005), which propose an automated process to estimate one-way focusing operators by a global inversion method from the two-way reflection response as observed in the seismic pre-stack data. For the optimization a genetic algorithm was employed, which requires a parametric description of the one-way focusing operators. However, a severe limitation of the method proposed by Verschuur and Marhfoul (2005) is that they adopt the parameterization of the focusing operators via semi-hyperbolic functions, as proposed by Hindriks and Verschuur (2001), which was geared towards the complex near surface problem. For the problem of a more general complex overburden such a parameterization is found to be inadequate, because for heterogeneous media we can expect the one-way travel time functions to be highly nonhyperbolic. Abbad et al. (2009) used automatic nonhyperbolic parametric search for anisotropic media, but still rely on an offset-symmetric parameterization. In this paper we implement a different and efficient parameterization with a control on the smoothness of these functions, based on bi-cubic spline interpolation functions (Akima, 1970). The arrival times belonging to propagation through a gas cloud can then be properly described (see Figure A.2a) such that each one-way travel time operator is depicted by a few spline knots at fixed lateral positions (see Figure A.2b). These knots can be placed either uniformly along the focusing operator-offset range or placed strategically in the region of near offsets to handle irregularities of the near surface overburden. Furthermore, at the far offsets, two fixed spline knots are imposed, indicated by the yellow dots in Figure A.2b, to control the behavior of the operator times for larger offsets, which is outside the area of interest. These fixed travel times at the extra control points are based on an initial hyperbolic velocity. Only small travel time variations

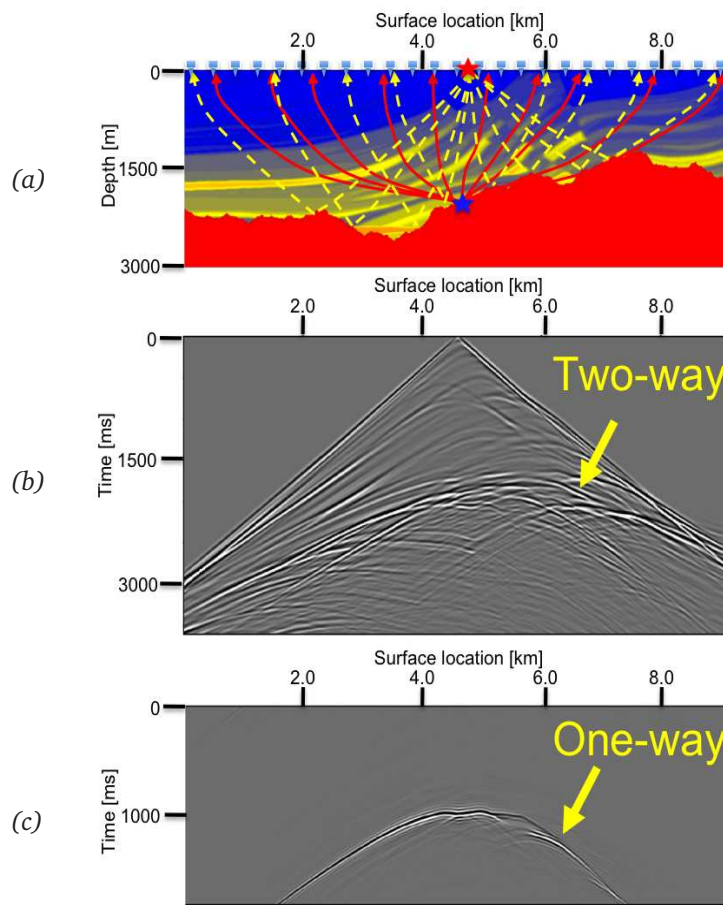


Figure A.1 (a) A complex subsurface overburden model with a rugged reflector topography in solid red area. The yellow dotted arrows illustrate the two-way wavefield raypath and the solid red arrows denote the one-way propagation raypath. (b) The result of two-way wavefield propagation, where the reflection energy from this rugged topography, indicated by the yellow arrow, is completely obscured. (c) A one-way wavefield is inherently simpler than the two-way wavefield propagation shown in Figure A.1b. As illustrated in Figure A.1a, the red star is the source location from the rugged topography and the wavefield energy is received at the acquisition surface and the blue star represents the virtual source location.

Δt will be allowed at the solid spline knots. Red dotted lines in Figure A.2b show different realizations of the spline approximation functions.

Note that only a limited offset range of the operators are supported by the seismic data. As a rule of thumb, the reliable one-way offsets are half of the offsets over which the reflection event is visible in the seismic data. For the optimization process, operators for a dense set of CFP locations along the target horizon are required. Therefore, these spline knots are

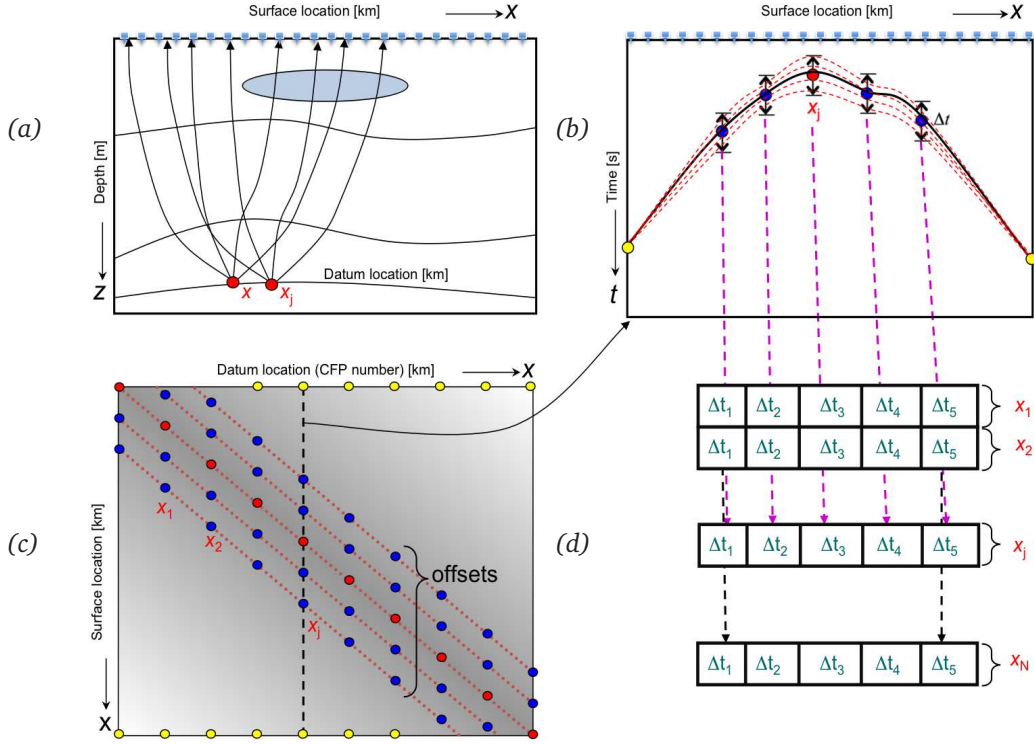


Figure A.2 (a) A CFP operator through a heterogeneous subsurface yield nonhyperbolic travel times due to effect of the gas lens. (b) A number of knots shown as red, blue and yellow dots that parameterize the one-way travel time functions defined along the offset axis. The operator times are interpolated by spline functions. Allowing variations of the travel times at the knots (Δt) yields different realizations of this one-way travel time function (red dotted lines). (c) Parameterization for the one-way travel times as a function of CFP location and surface x -locations. The red dots form the spline knots, which are first interpolated in the CFP direction (along the blue dotted lines) and then in the x -direction for each CFP-point. (d) The times at the spline knots yield the parameter set to be optimized.

defined for CFP locations at a regular interval. Next, similar spline knots are interpolated along the CFP axis, visualized by the dotted lines in Figure A.2c, after which the operator is obtained for each CFP location by spline interpolation. One such an operator, for the black dashed line, is shown as a zoom in Figure A.2b. For global optimization, by randomizing the time values within a certain range of Δt at each spline knot, new travel time functions can be created for each definition point along the lateral axis. Thus, referring to Figure A.2c, the time value at each red and blue dot is varied and for each realization, the one-way travel time functions are interpolated in both the focal point and the surface direction. Next,

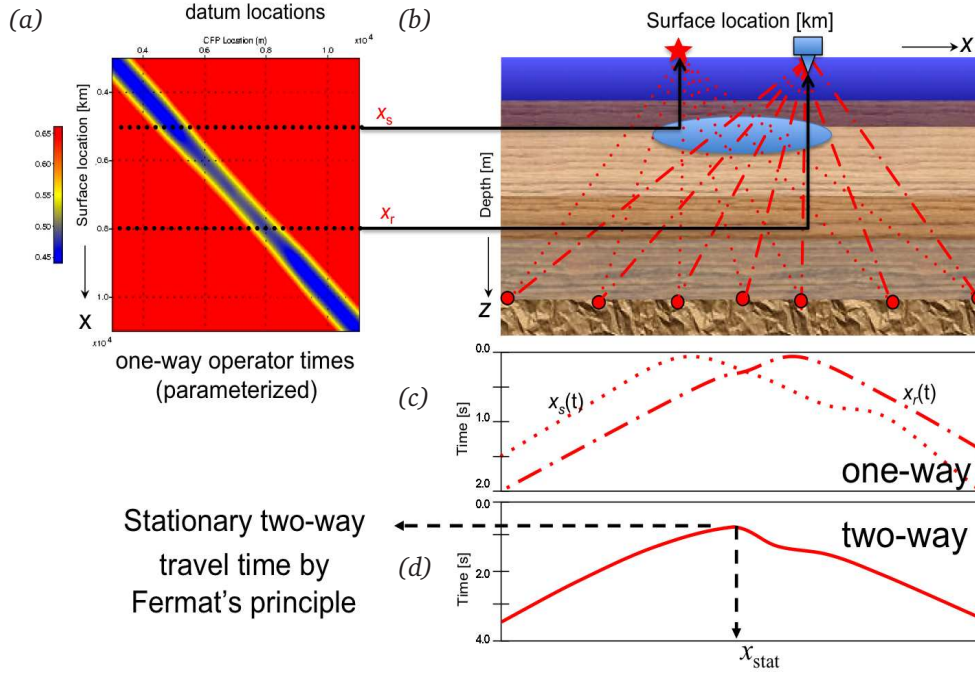


Figure A.3 Schematic diagram of Fermat's modeling principle that is based on minimum travel time. (a) One-way-travel time operator matrix where source location (x_s) and receiver location (x_r) are annotated. (b) The red circles represent the CFP locations and thin red dotted lines show all possible one-way-time from x_s , via the CFP locations to x_r and vice versa. The thick solid red line describes the minimum two-way-time combination based on Fermat's principle. (c) Schematic of one-way-time functions for each x_s and x_r to x_{cfp} . (d) Schematic of the minimum two-way-time function based on equation A.2, where x_{stat} is the stationary point.

Fermat modeling (Verschuur and Marhfohl, 2005) is used to create the corresponding two-way times for each source-receiver pair. These two-way times are validated in the seismic traces, thus defining a fitness value for each set of parameters.

Figure A.3 shows a schematic diagram illustrating the Fermat modeling principle, where two-way travel times are estimated for a certain source/receiver pair (x_s and x_r in Figure A.3a), by constructing all possible reflection paths from the source, towards different CFP locations and back to the receiver (the red dotted lines in Figure A.3b). The CFP location with the shortest one-way travel time operator, shown as the thick solid red line in Figure A.3b, yields the physical two-way time in Figure A.3d. The minimum two-way-time $t_{twt}(x_r, x_{cfp})$ for a certain source-receiver combination can be expressed as:

$$t_{twt}(x_s, x_r) = \min_{x_{cfp}} [t_{owt}(x_s, x_{cfp}) + t_{owt}(x_r, x_{cfp})], \quad (\text{A.2})$$

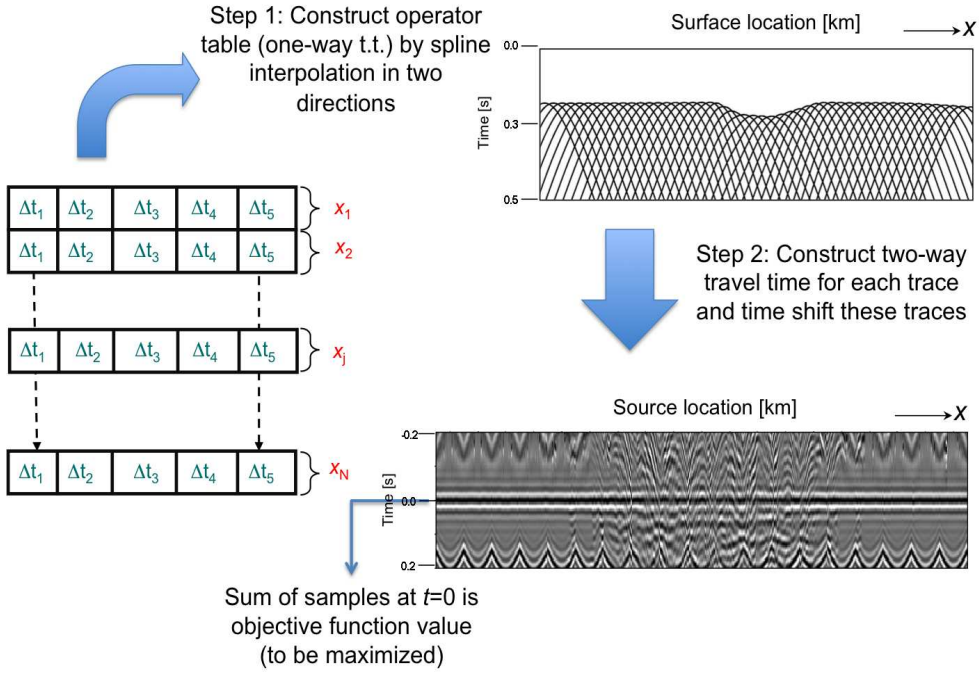


Figure A.4 Workflow of the Fermat modeling principle. The one-way-time table as shown in Figure A.2d is interpolated by spline functions in two directions, along surface and CFP locations. By calculating the corresponding two-way travel time for each trace, applying this as a time shift and calculate the sum of the samples at $t=0$ provides the objective function value to be maximized. The global optimization process will vary the one-way travel time parameters until the objective function is maximum, meaning perfect alignment of the reflection at $t=0$ for all traces.

where $t_{tw}(x_r, x_{cfp})$ is the one-way travel time from the source location x_s to CFP location x_{cfp} and $t_{owt}(x_r, x_{cfp})$ the one way time from receiver location x_r to x_{cfp} .

At the predicted two-way time in the corresponding trace the value of the corresponding time sample is selected. Adding these amplitudes for all traces, the objective function is obtained. By using a genetic algorithm, this objective function is maximized by changing the spline functions until the stacked amplitudes along these operator times is maximized (Figure A.4).

A.5 Proposed CFP imaging workflow for gas clouds

The proposed gas cloud imaging workflow can be described as follows:

1. Based on a time section of the seismic data, target horizons are identified. These vertical time picks will be used as the apex times for the initial focusing operators for each boundary. The initial focusing operator from reflecting boundaries are calculated by generating hyperbolic operators based on these time picks and NMO velocities.
2. A grid of spline knots is defined, which forms the parameters of the optimization process. Initial values are set based on the hyperbolic operators in step 1 and the operator times are allowed to vary within a certain pre-defined Δt parameter.
3. Applying Fermat's principle by combining two one-way-travel time functions for each source-receiver combination to produce a two-way-time and collect its corresponding data sample in the trace. Repeating this for each seismic trace yields an objective function based on the stack power: if the focusing operators are correct then the sum of all data samples along the estimated two-way times will yield a maximum. A genetic algorithm changes the parameters of the one-way focusing operators until the best set is obtained.
4. As a QC for the final one-way focusing operators, its corresponding two-way travel times can be used to flatten the shot records. The reflection event is expected at zero time for all offsets. This process is repeated for a number of key horizons in the data.
5. An interpolation algorithm is used to obtain focusing operators for each vertical apex time and each lateral focal point position (i.e. for locations between the key horizons). The interpolated focusing operators represent a complete migration operator travel time table, without any knowledge about the underlying velocity model. With this densely sampled travel time table, a complete pre-stack image can be obtained, although the output is in vertical one-way time (see Berkhout and Verschuur (2001)).
6. The focusing operator times can be used as input for a tomography inversion algorithm (Cox and Verschuur, 2001) to produce a velocity-depth model. This velocity model can be applied for depth migration or time-to-depth conversion of the CFP image.

A.6 Results for synthetic data

We first tested the proposed methodology on a synthetic model as shown in Figure A.5a. The model for this study was built to mimic Malaysian tertiary basins characteristics (Ghazali et al., 2008). The synthetic data was obtained via a 2D acoustic finite difference algorithm. The medium properties were collectively based on surface seismic, check-shots, sonic and dipole sonic, density and lithology log information. The velocity and density field in the

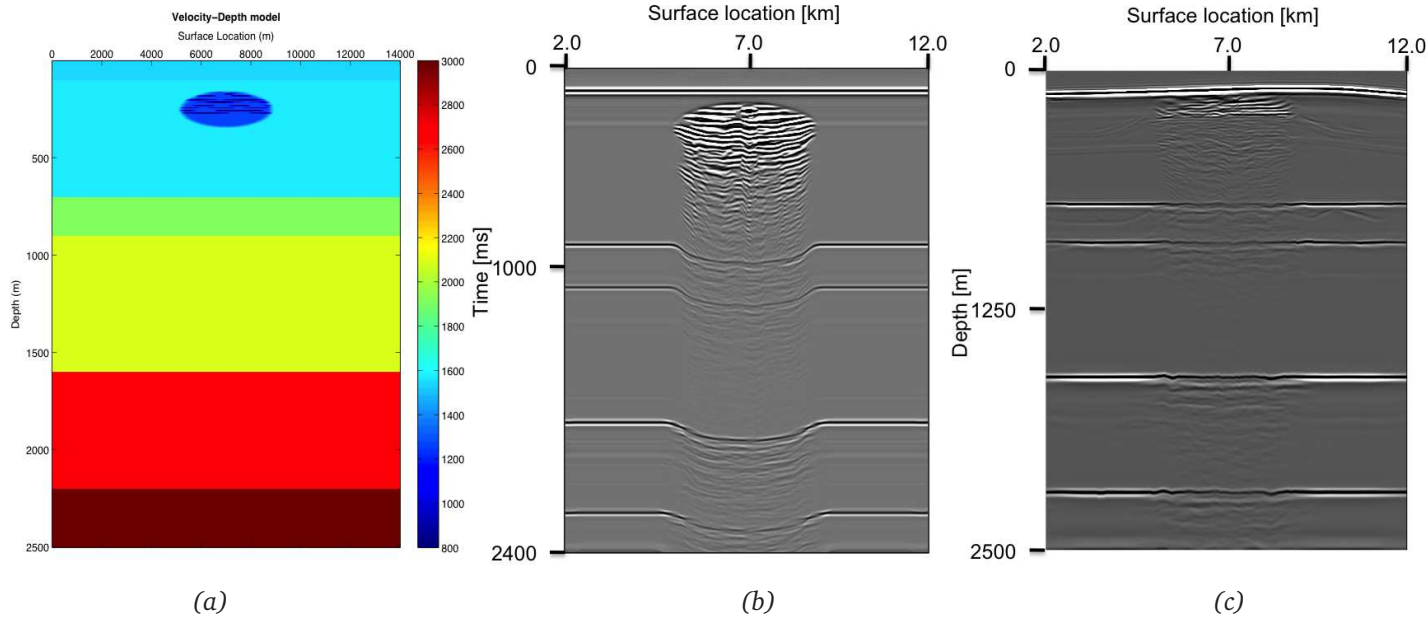


Figure A.5 (a) Velocity depth model, including a low velocity anomaly. (b) Stack section. Note that very poor consistent reflections underneath the gas cloud. (c) CFP one-way time image after full execution of the proposed gas cloud imaging workflow. Result after proper time-to-depth conversion. Note that the CFP image directly uses the estimated focusing operators. This ensures better amplitude focusing below the subsurface complexities, thus providing good lateral reflection continuity.

model have the same structural geometrical features. At this stage, there was no attenuation built into this model, thus any amplitude attenuation seen on the seismic is due to complex wave propagation.

The five boundaries in this model were used to evaluate the proposed workflow: for each boundary the zero offset times were picked in the stack section (Figure A.5b) and with the genetic algorithm focusing operator times were estimated. With these focusing operators a *CFP* image was calculated. Note that the focusing of the reflection events below the gas anomaly is quite good, however, the output is still in one-way vertical time. A time to depth conversion (Figure A.5c) yields the final depth image and reflection energy below the gas cloud area is mostly recovered. As a QC, shot records were flattened with the estimated two-way travel times. In Figure A.6a and Figure A.6d the results are shown for the best matching hyperbolic focusing operators for shallow and deeper reflectors respectively. Next, the method proposed by Verschuur and Marhfoul (2005) yields the result of Figure A.6b and Figure A.6e. They allow a semi-hyperbolic parameterization with five parameters per operator, which increases the focusing quality. However, these operators cannot adequately describe the propagation through an anomaly as present in this model, especially for the deeper horizon (Figure A.6b, right hand side). However, by using the spline parameterization to estimate focusing operators shows better degree of flatness for the shots, as can be observed in Figure A.6c and Figure A.6f. Note that the difference between Figure A.6a and Figure A.6c represents the difference between *PreSTM* and *CFP* one-way imaging. The continuity of the reflectors underneath the gas area is better in Figure A.6c and also notes that the codas underneath the main reflectors are also well constructed. Summing along this operators at $t = 0$ the maximum resultant stack power of the sum will indicate that optimum migration operators have been used.

A.7 Results for field data

The workflow was also applied for a 2D field dataset from Malay basin area, in Malaysia. Prior to imaging steps, wavelet deconvolution and surface multiple suppression, using a combination of surface-related multiple elimination (*SRME*) and Radon demultiple, were applied. The boundaries of interest are picked on a time section, as shown in Figure A.7. Next, from these vertical times initial focusing operators are constructed. Via the genetic algorithm the focusing operators were optimized. As a QC, some shot records after flattening with the estimated two-way times are shown in Figure A.8a. The red arrow indicates the lateral extend of the gas cloud area. Note that reflection energy is observed in the area below the gas cloud. Another QC-tool is to stack all traces of the time-corrected shots in the *CMP* domain. The result (Figure A.8b) can be used to investigate the lateral consistency of the estimated operators.

Finally, we interpolated the estimated focusing operators to a dense grid of vertical one-way times and calculated the *CFP* image. In Figure A.9 this result is compared to the traditional Kirchhoff pre-stack time migration result (*PreSTM*). Both methods have their output in ver-

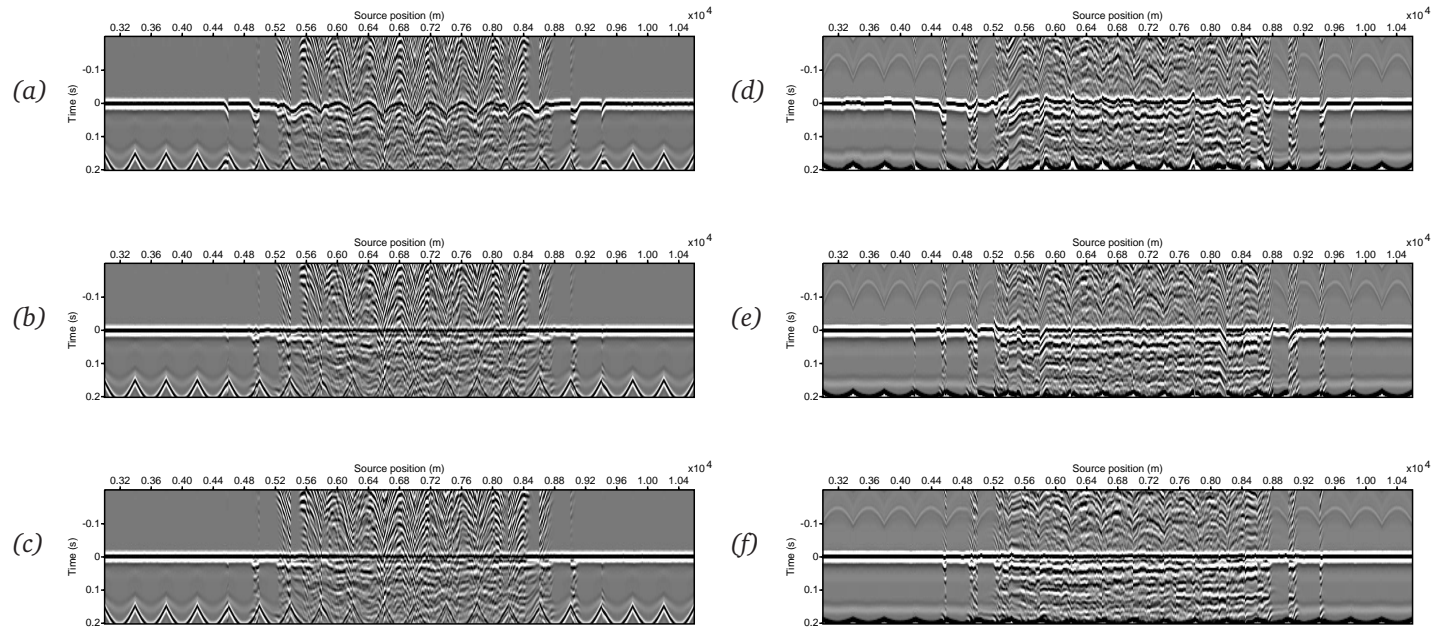


Figure A.6 Synthetic data shot records flattened with two-way travel times estimated from best-matching travel time operators for shallow (Figure A.6(a-c)) and deeper reflectors (Figure A.6(d-f)). (a) Flattened shot records using only pre-stack time migration operators. (b) Flattened shot records based on the estimated operator proposed by Verschuur and Marhfoul (2005) using two half hyperbolae. (c) Flattened shot records based on the new nonhyperbolic spline-genetic algorithm focusing operators.

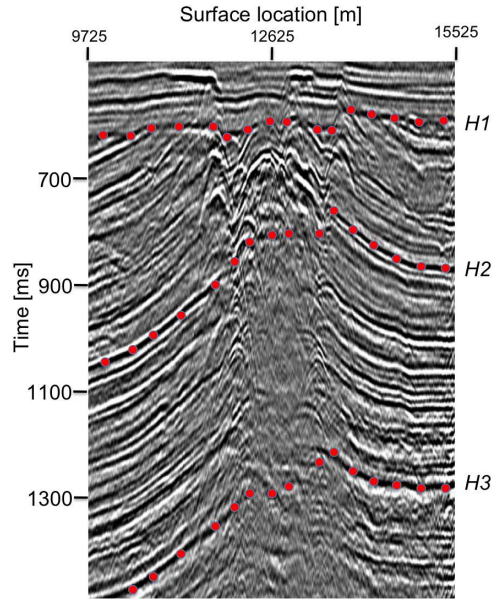


Figure A.7 Three horizons, indicated by $H1$, $H2$ and $H3$, picked in a stacked section of the field data. The gas cloud is mainly located between $H1$ and $H2$ in the middle of the section. The red dots indicate the CFP locations at each horizon. They serve as initial one-way time values, after which the global optimization process will find the best travel time operators for that particular reflector.

tical time, but the *PreSTM* (Figure A.9a) uses hyperbolic focusing operators and the *CFP* image (Figure A.9b) is based on the estimated nonhyperbolic and non-symmetric focusing operators. As the one-way time operators were estimated such that they optimally focus the seismic energy, a better-focused result is obtained. The *CFP* image shows an improved lateral continuity of the imaged reflectors and has a better amplitude reconstruction below the gas cloud. It is important to note that the *CFP* image does not require a macro velocity model for the focusing part, but only for the time-to-depth conversion, which was not described here. Thus, the *CFP* imaging approach yields an optimum focusing of energy below complex areas, with less sensitivity to the estimation and parameterization of the velocity-depth model; the latter is only used for time-to-depth conversion.

A.8 Conclusions and discussion

The proposed imaging workflow in this appendix demonstrates the potential of using and enhancing *CFP* technology to image reflectors underneath complex overburdens, such as gas clouds. It avoids the estimation of a velocity-depth model in an early stage and finds focusing operators directly from the data via a hands-off data-driven strategy. Furthermore, it allows

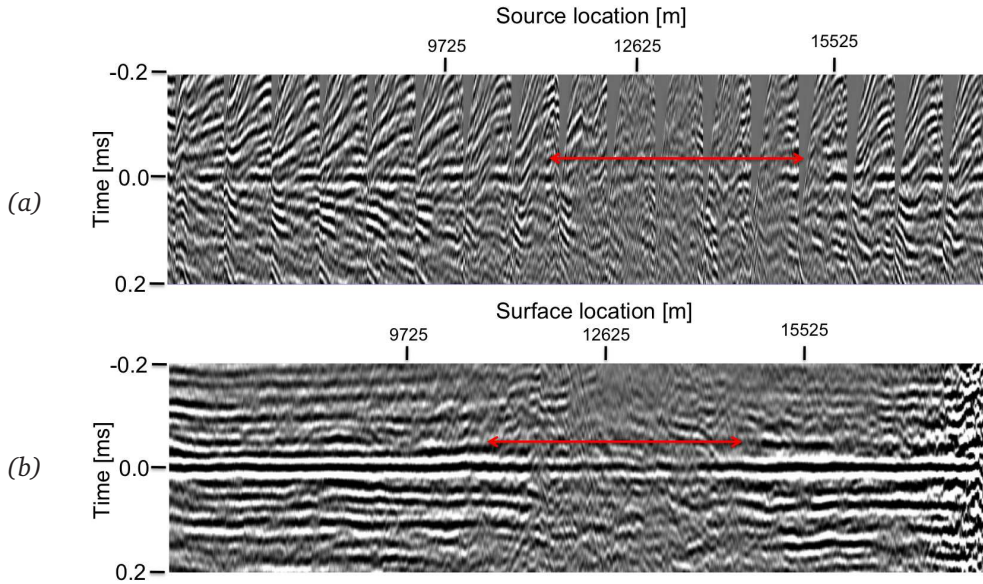


Figure A.8 (a) Flattened shot records using the predicted two-way travel times of the estimated operators for horizon $H3$ as indicated in Figure A.7. (b) Result of CMP stacking all traces of the time-corrected shots. Note the recovered reflection energy below the gas cloud. The arrow shows the lateral extent of gas cloud region above this reflector. Note that focused energy has been recovered below the gas cloud.

nonhyperbolic and non-symmetric focusing operators, such that it overcomes the limitations of traditional time-migration processes in complex areas. Final imaging results demonstrate improvements in overall resolution, reflection continuity and recovered amplitudes. It proves that there is reflection information from underneath the gas clouds available in the seismic data. Finding the right focusing operators that correct for these effects will reveal a lot of the information from underneath such anomalies. We have also demonstrated that the new dual directional spline-offset knots parameterization strategy has given good result to estimate the nonhyperbolic one-way travel times with a hands-off global optimization method. In this way one-way travel time operators could be obtained that describe the reflection events below a low velocity gas cloud anomaly.

Finally, note that what is often referred to as ‘absorption’ is perhaps is due to more a complex wave propagation phenomenon. Although some energy may really disappear into heat (anelastic loss), we believe that a large part of the energy is lost in elastic mechanisms (internal scattering, multipathing, nonhyperbolic migration operators etc.). Thus, no-data-zones actually are no-proper-tool-zones. By improved imaging algorithms, more energy can be recovered and imaged.

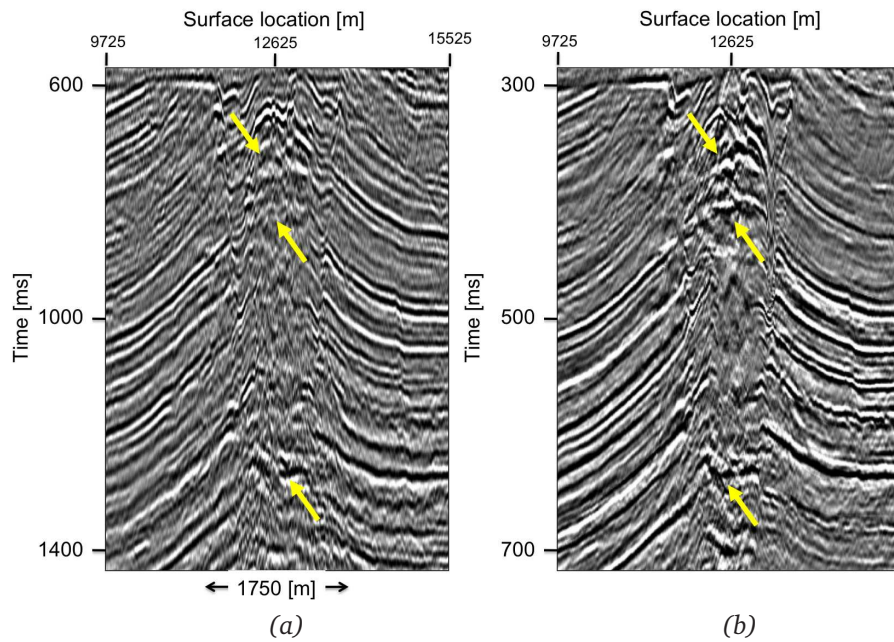


Figure A.9 (a) The Kirchhoff pre-stack time migration result and (b) the CFP one-way time image. The CFP image directly uses the estimated focusing operators, ensuring better amplitude focusing below the subsurface complexities. The arrows in Figure A.9b show the improvements inside and underneath the gas cloud.

A.9 Acknowledgment

We extend our gratitude to PETRONAS and PETRONAS Research, Malaysia, for providing the seismic data and for giving the permission to publish this work. Also, we thank the sponsors of the DELPHI consortium for their support.

B

Recursive seismic modeling in the ray-parameter-frequency domain

One of the approaches in computing wave propagation in layered media is the use of Kennett's method (Kennett, 1983), where the invariant embedding method is used to generate the response of a layered medium recursively (Mavko et al., 2003). The layered medium is assumed to have no lateral heterogeneities and layers are isotropic. For P-waves traveling in isotropic media, incidence at a boundary between two isotropic media is shown in Figure B.1. The reflections and transmission coefficients are expressed in terms of ray parameter (p_x) and frequency (ω). The terms \hat{R}^+ and \hat{T}^+ are functions of ω and represent the overall transfer functions of the layered medium in the frequency domain:

$$R^+(p_x) = \frac{\rho_n c_n \cos\alpha - \rho_{n-1} c_{n-1} \cos\beta}{\rho_n c_n \cos\alpha + \rho_{n-1} c_{n-1} \cos\beta} \quad (\text{B.1})$$

$$T^+(p_x) = \frac{2\rho_n c_n \cos\alpha}{\rho_n c_n \cos\alpha + \rho_{n-1} c_{n-1} \cos\beta} \quad (\text{B.2})$$

and

$$\frac{\cos\alpha}{c_{n-1}} = \sqrt{\frac{1 - \sin^2\alpha}{c_{n-1}}} = q_1 \quad (\text{B.3})$$

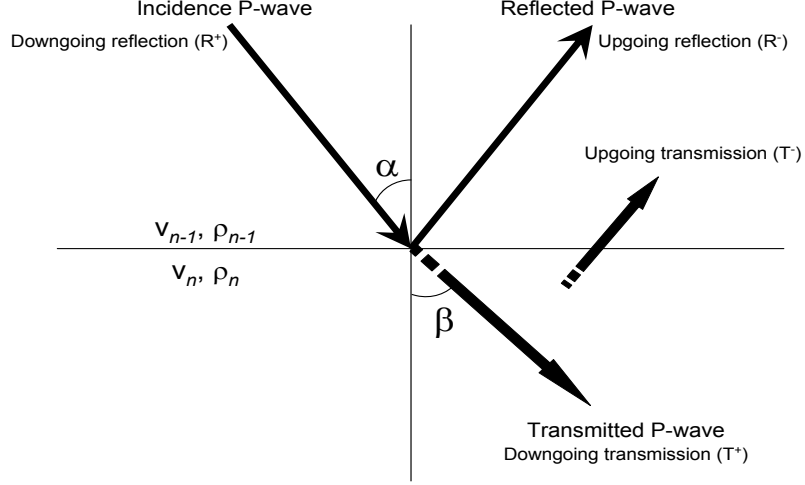


Figure B.1 Schematic of reflected and transmitted P-waves incidence at a boundary between two isotropic media

$$\frac{\cos\beta}{c_n} = \sqrt{\frac{1 - \sin^2\beta}{c_n}} = q_2. \quad (\text{B.4})$$

Usually, we calculate the forward modeling in the ray-parameter domain. For the ray parameter p_x at $|p_x| < \frac{1}{c}$ we have the following relations:

$$p_x = \frac{\sin\alpha}{c_{n-1}} = \frac{\sin\beta}{c_n} \quad (\text{B.5})$$

$$q_{n-1} = \sqrt{\frac{1}{c_{n-1}^2} - p_x^2} \quad (\text{B.6})$$

$$q_n = \sqrt{\frac{1}{c_n^2} - p_x^2} \quad (\text{B.7})$$

and for $|p_x| > \frac{1}{c}$

$$q_{n-1} = -j\sqrt{p_x^2 - \frac{1}{c_{n-1}^2}} \quad (\text{B.8})$$

$$q_n = j\sqrt{p_x^2 - \frac{1}{c_n^2}}. \quad (\text{B.9})$$

Thus, the reflection and transmission coefficients can be expressed in terms of ray parameters (p):

$$R^+(p_x) = \frac{\frac{\rho_n \cos \alpha}{c_{n-1}} - \frac{\rho_{n-1} \cos \beta}{c_n}}{\frac{\rho_n \cos \alpha}{c_{n-1}} + \frac{\rho_{n-1} \cos \beta}{c_n}} = \frac{\rho_n q_{n-1} - \rho_{n-1} q_n}{\rho_n q_{n-1} + \rho_{n-1} q_n} \quad (\text{B.10})$$

$$T^+(p_x) = \frac{2\rho_n q_{n-1}}{\rho_n q_{n-1} + \rho_{n-1} q_n}, \quad (\text{B.11})$$

with

$$R^-(p_x) = -R^+(p_x), \quad (\text{B.12})$$

and in which the phase shift operator for propagation across each layer n is given by:

$$E(p_x, \omega) = e^{-j(\omega + j\sigma)q_n \Delta z}, \quad (\text{B.13})$$

where σ is a stabilization operator in the frequency domain which can be removed after inverse transform to the time domain.

Recursively the transfer function at each layer n starting from the deepest layer until it reaches the upper most layer (acquisition surface) of $z_d = z_0$. Time domain synthetic full waveform seismograms can be obtained by inverse Fourier transform the overall transfer function at the surface for each p_x -values multiplied by the source wavelet in the frequency domain:

$$\widehat{R}_n^+ = R_n + \frac{T_{n-1}^- E_{n-1}^+ \widehat{R}_n^+ E_{n-1}^+}{1 - R_{n-1}^- E_{n-1}^+ \widehat{R}_n^+ E_{n-1}^+} T_{n-1}^- \quad (\text{B.14})$$

$$\widehat{T}_n^+ = \frac{\widehat{T}_n^+ E_{n-1}^+}{1 - R_{n-1}^- E_{n-1}^+ \widehat{R}_n^+ E_{n-1}^+} T_{n-1}^- \quad (\text{B.15})$$

At the deepest layer the recursion is initiated with \widehat{R}^+ and \widehat{T}^+ as follows:

$$\widehat{R}^+ = 0 \quad (\text{B.16})$$

$$\widehat{T}^+ = 1. \quad (\text{B.17})$$

References

- Abbad, B., Ursin, B., and Rappin, D., 2009, Automatic non-hyperbolic velocity analysis: *Geophysics*, **74**, no. 2, U1–U12.
- Abubakar, A., Habashy, T. M., van den Berg, P. M., and Gisolf, A., 2005, The diagonalized contrast source approach: an inversion method beyond the born approximation: *Inverse Problems*, **21**, 685–702.
- Aki, K., and Richards, P. G., 1980, *Quantitative seismology - second edition*: University Science Book.
- Akima, H., 1970, A new method for interpolation and smooth curve fitting based on local procedures: *Journal of the ACM*, **17**, no. 4, 589–602.
- Al-Ali, M. N., and Verschuur, D. J., 2006, An integrated method for resolving the seismic complex near surface problem: *Geophys. Prosp.*, **54**, no. 6, 739–750.
- Al-Chalabi, M., 1976, Velocity determination from seismic reflection data: In: *Development in Geophysical Exploration Methods*, Applied Science Publishers, **1** (ed. A. A. Fitch), 1–68.
- Armstrong, T., McAteer, J., and Connolly, P., 2001, Removal of overburden velocity anomaly effects for depth conversion: *Geophysical Prospecting*, **49**, 79–99.
- Arntsen, B., Wensaas, L., Loseth, H., and Hermanrud, C., 2007, Seismic modeling of gas chimneys: *Geophysics*, **72**, no. 5, SM251–SM259.
- Batzle, M., Hofmann, R., Duranti, G. K. L., and Han, D., 2005, Seismic frequency loss mechanisms: Direct observation: 63rd Ann. Internat. Mtg., Eur. Ass. of Geosc. and Eng., Expanded abstracts, P160.
- Baysal, E., Kosloff, D. D., and Sherwood, J. W. C., 1983, Reverse time migration: *GEOPHYSICS*, **48**, no. 11, 1514–1524.
- Baysal, E., Kosloff, D. D., and Sherwood, J. W. C., 1984, A two-way nonreflecting wave equation: *GEOPHYSICS*, **49**, 132–141.

References

- Bear, L., Liu, J., and Traynin, P., 2008, Efficient compensation for attenuation effects using pseudo Q migration: 78th Ann. Internat. Mtg., Soc. Expl. Geophys., Expanded abstracts, 2206–2210.
- Berkhout, A. J., 1982, Seismic migration, imaging of acoustic energy by wave field extrapolation: Elsevier.
- Berkhout, A. J., 1997a, Pushing the limits for seismic imaging, part 1: Integration of prestack migration, velocity estimation and AVO analysis: *Geophysics*, **62**, no. 3, 954–969.
- 1997b, Pushing the limits for seismic imaging, part 2: Prestack migration in terms of double dynamic focusing: *Geophysics*, **62**, no. 3, 937–953.
- Berkhout, A. J., and Verschuur, D. J., 2001, Seismic imaging beyond depth migration: *Geophysics*, **66**, no. 6, 1895–1912.
- Berkhout, A. J., and Verschuur, D. J., 2005, Removal of internal multiples with the common-focus-point (CFP) approach: Part 1 - Explanation of the theory: *Geophysics*, **70**, no. 3, V45–V60.
- Berkhout, A. J., 2008, Changing the mindset in seismic data acquisition: *The Leading Edge*, **27**, 924.
- Berkhout, A. J., Blacquièrè, G., and Verschuur, D. J., 2008, From simultaneous shooting to blended acquisition: SEG International Exposition and Annual meeting, , no. Las Vegas, 2831–2838.
- Berryhill, J. R., 1979, Wave equation datuming: *Geophysics*, **44**, no. 8, 1329–1344.
- Biondi, B., and Shan, G., 2002, Prestack imaging of overturned reflections by reverse time migration: 72nd Ann. Internat. Mtg., Soc. Expl. Geophys., Expanded abstracts, 1284–1287.
- Blacquièrè, G., Berkhout, A. J., and Verschuur, D. J., 2009, Survey design for blended acquisition: 79th Ann. Internat. Mtg., Soc. Expl. Geophys., Expanded abstracts, 56–60.
- Bolte, J. F. B., and Verschuur, D. J., 1998, Aspects of focusing operator updating: 68th Ann. Internat. Mtg., Soc. Expl. Geophys., Expanded abstracts, 1604–1607.
- Bolte, J. F. B., 2003, Estimation of focusing operators using the common focal point method: Ph.D. thesis, Delft University of Technology.
- Brandsberg-Dahl, S., de Hoop, M. V., and Ursin, B., 2003, Focusing in dip and AVA compensation on scattering-angle/azimuth common image gathers: *Geophysics*, **68**, no. 1, 232–254.
- Campman, X. H., van Wijk, K., Scales, J. A., and Herman, G. C., 2005, Imaging and suppressing near-receiver scattered surface waves: *Geophysics*, **70**, no. 2, 21–29.

- Cavalca, M., and Fletcher, R. P., 2008, Deriving 3D Q models from surface seismic data using attenuated traveltimes tomography: 70th EAGE Conf. and Exhibition, Eur. Assoc. Geosc. Eng., Expanded abstracts, H003.
- Cox, B. E., and Verschuur, D. J., 2001, Data-driven tomographic inversion of focusing operators: 71st Ann. Internat. Mtg., Soc. Expl. Geophys., Expanded abstracts, 722–725.
- Dasgupta, R., and Clark, R. A., 1998, Estimation of Q from surface seismic reflection: *Geophysics*, **63**, no. 6, 2120–2128.
- Dvorkin, J. P., and Mavko, G., 2006, Modeling attenuation in reservoir and nonreservoir rock: *The Leading Edge*, pages 194–197.
- Fokkema, J. T. ., and van den Berg, P. M., 1993, *Seismic applications of acoustic reciprocity*: Elsevier Science Publishers B.V.
- Frijlink, M., 2007, *Seismic redatuming with transmission loss correction in complex media*: Ph.D. thesis, Delft University of Technology.
- Gallagher, K., Sambridge, M., and Drijkoningen, G., Mar 1991, Genetic algorithms: An evolution from Monte Carlo methods for strongly nonlinear geophysical optimization problems: *Geophysical Research Letters*, **18**, no. 12, 2177–2180.
- Gallagher, K., and Sambridge, M., 1994, Genetic algorithms: a powerful tool for large-scale nonlinear optimization problems: *Computers & Geosciences*, **20**, no. 7-8, 1229–1236.
- Ghazali, A. R., Verschuur, D. J., and Gisolf, A., 2008, Seismic imaging through gas clouds: A data-driven imaging strategy: 78th SEG Las Vegas. Ann. Internat. Mtg., SEG Technical Program Expanded Abstracts, **27**, no. 1, 2302–2306.
- Ghosh, D., Halim, M. F. A., Brewer, M., Viratno, B., and Darman, N., 2010, Geophysical issues and challenges in Malay and adjacent basins from an E and P perspective: *The Leading Edge*, **April**, 436–447.
- Gisolf, A., and Verschuur, D. J., 2010, *The principles of quantitative acoustical imaging*: EAGE Publications bv.
- Granli, J. R., Arntsen, B., Sollid, A., and Hilde, E., 1999, Imaging through gas-filled sediments using marine shear-wave data: *Geophysics*, **64**, no. 3, 668–677.
- Hanssen, P., Ziolkowski, A., and Li, X.-Y., 2003, A quantitative study on the use of converted waves for sub-basalt imaging: *Geophys. Prosp.*, **51**, 183–193.
- Heggland, R., 1997, Detection of gas migration from a deep source by the use of exploration 3D seismic data: *Marine Geology*, **137**, 41–47.
- Hindriks, C. O. H., and Verschuur, D. J., 2001, CFP approach to the complex near surface: 71st Ann. Internat. Mtg., Soc. Expl. Geophys., Expanded abstracts, 1863 – 1866.

References

- Hornman, K., 2004, Data acquisition over the Lunskeye gas cloud: The Leading Edge, **October**, 1066–1069.
- Johnston, D. H., Toksoz, M. N., and Timur, A., 1979, Attenuation of seismic waves in dry and saturated rocks: II. mechanisms: *Geophysics*, **44**, no. 4, 691–711.
- Johnston, D. H., Sun, M., Gouveia, W. P., Lu, C. P., Walley, D. S., and Lye, Y. C., 2002, Time-lapse seismic analysis at Irong Barat: Malay basin: 72nd Ann. Internat. Mtg., Soc. Expl. Geophys., Expanded abstracts.
- Jones, I. F., 2008, A modeling study of preprocessing considerations for reverse-time migration: *GEOPHYSICS*, **73**, T99.
- Judd, A. G., and Hovland, M., 1992, The evidence of shallow gas in marine sediments: *Continental Shelf Research*, **12**, no. 10, 1081–1097.
- Kabir, M. M. N., and Verschuur, D. J., 1995, Restoration of missing offsets by parabolic radon transform: *Geophys. Prosp.*, **43**, no. 3, 347–368.
- Kabir, N., Albertin, U., Zhou, M., Nagassar, V., Kjos, E., Whitaker, P., and Ford, A., 2008, Use of refraction, reflection, and wave-equation-based tomography for imaging beneath shallow gas: A Trinidad field data example: *Geophysics*, **73**, no. 5, VE281–VE289.
- Kelamis, P. G., Erickson, K. E., Verschuur, D. J., and Berkhout, A. J., 2002, Velocity-independent redatuming: a new approach to the near-surface problem in land seismic data processing: *The Leading Edge*, **21**, no. 8, 730–735.
- Kennett, B. L. N., 1983, *Seismic wave propagation in stratified media*: Cambridge University Press, Cambridge.
- Khan, O., and Klein-Helmkamp, U., 2005, Deepwater imaging beneath gas anomalies a case study: 67th Conference and Exhibition, Eur. Assoc. Geos. Eng, Expanded abstracts.
- Krebs, J. R., Anderson, J. E., Hinkley, D., Neelamani, R., Lee, S., Baumstein, A., and Lacasse, M. D., 2009, Fast full-wavefield seismic inversion using encoded sources: *GEOPHYSICS*, **74**, no. 6, WCC177–WCC188.
- Lam, C. H., van den Berg, P. M., and Gisolf, A., 2007, Nonlinear inversion of focused data: *SEG Technical Program Expanded Abstracts*, **26**, no. 1, 1750–1754.
- Levin, S. A., 1984, Principle of reverse time migration: *GEOPHYSICS*, **49**, 581.
- Li, X.-Y., MacBeth, C., Hitchen, K., and Hanssen, P., 1998, Using converted waves for imaging beneath basalt in deep water plays: 68th Ann. Internat. Mtg., Soc. Expl. Geophys., Expanded abstracts, 1369–1372.
- Li, X.-Y., Dai, H., Mueller, M. C., and Barkved, O. I., 2001, Compensating for the effects of gas clouds on C-wave imaging: A case study from Valhall: *The Leading Edge*, **20**, no. 12, 1351–1360.

- MacLeod, M. K., Hanson, R. A., Bell, C. R., and McHugo, S., 1999, The Alba field ocean bottom cable seismic survey: Impact on development: *The Leading Edge*, **18**, no. 1, 1306–1312.
- Mallick, S., 1995, Model-based inversion of amplitude variations-with-offset data using a genetic algorithm: *Geophysics*, **60**, no. 4, 939–954.
- Malme, T. N., Landro, M., and Mittet, R., 2003, Effects of overburden distortions on 3D seismic data - a sensitivity study: 65th Ann. Internat. Mtg., Eur. Assoc. of Geos. and Engs, Expanded abstracts, C42.
- Mavko, G., Mukerji, T., and Dvorkin, J., 2003, *The rock physics handbook: Tools for seismic analysis in porous media*: Cambridge University Press, Cambridge.
- McCormack, M. D., Stoitsits, R. F., MacAllister, D. J., and Crawford, K. D., 1999, Applications of genetic algorithms in exploration and production: *The Leading Edge*, **18**, no. 6, 716–718.
- Mulder, W. A., and Hak, B., 2009, Velocity and attenuation perturbations can hardly be determined simultaneously in acoustic attenuation scattering: 79th SEG Houston. Ann. Internat. Mtg., Soc. Expl. Geophys., Expanded abstracts, 3078–3082.
- Muller, T. M., and Shapiro, S. A., 2004, Scattering attenuation in randomly layered structures with finite lateral extent: A hybrid Q model: *GEOPHYSICS*, **69**, no. 6, 1530–1534.
- O'Brien, M. J., Whitmore, D., Brandsberg-Dahl, S., Etgen, J., and Murphy, G., 1999, Multi-component modeling of the Valhall field: 61th Ann. Internat. Mtg., European Association of Geoscientists and Engineers, Expanded abstracts.
- O'Doherty, R. F., and Anstey, N. A., 1971, Reflections on amplitudes: *Geophysical Prospecting*, **19**, 430–458.
- Oezsen, R., Crawley, M., Yusoff, W. I. W., and Arshad, A. R. M., 1999, A 3D pre-stack depth migration case history from the South China Sea: *Warta Geologi*, Geological Society of Malaysia, **25**, no. 6, 303–304.
- Plessix, R. E., Baeten, G., de Maag, J. W., Klaassen, M., Rujie, Z., and Zhifei, T., 2010, Application of acoustic full waveform inversion to a low-frequency large-offset land data set: 80th Ann. Internat. Mtg., Soc. Expl. Geophys., Expanded abstracts, 903–934.
- Pratt, R. G., 1999, Seismic waveform inversion in the frequency domain, part 1: Theory and verification in a physical scale model: *GEOPHYSICS*, **64**, no. 3, 888–901.
- Prieux, V., Operto, S., Brossier, R., and Virieux, J., 2009, Application of acoustical full waveform inversion to the synthetic Vallhall velocity model.: 79th SEG Houston. Ann. Internat. Mtg., Soc. Expl. Geophys., Expanded abstracts.

References

- Robein, E., 2003, Velocity, time-imaging and depth-imaging in reflection seismics: Principles and methods: EAGE Publication.
- Romero, L., Ghiglia, D., Ober, C., and Morton, S., 2000, Phase encoding of shot records in prestack migration: *GEOPHYSICS*, **65**, no. 2, 426–436.
- Sambridge, M., and Drijkoningen, G., 1992, Genetic algorithms in seismic waveform inversion: *Geophysical Journal International*, **109**, no. 2, 323–342.
- Schroot, B. M., and Schuttenhelm, R. T. E., 2003, Expressions of shallow gas in the Netherlands North Sea: *Netherlands Journal of Geosciences*, **82**, no. 1, 91–105.
- Sears, T. J., Singh, S. C., and Barton, P. J., 2008, Elastic full waveform inversion of multi-component obc seismic data: *Geophysical Prospecting*, **56**, no. 6, 843–862.
- Sen, M. K., and Stoffa, P. L., 1991a, Nonlinear one-dimensional seismic waveform inversion using simulated annealing: *Geophysics*, **56**, no. 10, 1624–1638.
- 1991b, Simulated annealing, genetic algorithms and seismic waveform inversion: *SEG Technical Program Expanded Abstracts*, **10**, no. 1, 945–947.
- Sengupta, R. B. M., and Dutta, N., 2005, Attenuation estimation in high frequency surface seismic data with application for seismic reservoir characterization: 67th Ann. Internat. Mtg., Eur. Assoc. Geosc Eng, Expanded abstracts, Z99.
- Sheriff, R. E., 2001, *Encyclopedic dictionary of applied geophysics*: Society of Exploration Geophysicists, 4th edition.
- Shipp, R. M., and Singh, S. C., 2002, Two-dimensional full wavefield inversion of wide-aperture marine seismic streamer data: *Geophysical Journal International*, **151**, no. 2, 325–344.
- Shtivelman, V., and Canning, A., 1988, Datum correction by wave equation extrapolation: *Geophysics*, **53**, no. 10, 1311–1322.
- Sirgue, L., and Pratt, R. G., Jan 2004, Efficient waveform inversion and imaging- A strategy for selecting temporal frequencies: *GEOPHYSICS*, **69**, no. 1, 231–248.
- Sirgue, L., Barkved, O. I., Dellinger, J., Etgen, J., Albertin, U., and Kommedal, J. H., 2010, Full waveform inversion- the next leap forward in imaging at Valhall: *First break*, **28**, no. April, 65–70.
- Stork, C., 1992, Reflection tomography in the postmigrated domain: *Geophysics*, **57**, no. 5, 680–692.
- Stovas, A., and Arntsen, B., 2006, Vertical propagation of low-frequency waves in finely layered media: *Geophysics*, **71**, no. N3, T87–T94.

- Stovas, A., and Ursin, B., 2007, Equivalent time-average and effective medium for periodic layers: *Geophysical Prospecting*, **55**, no. N6, 871–882.
- Swan, H. W., 1991, Amplitude-versus-offset measurement errors in a finely layered medium: *Geophysics*, **56**, no. 1, 41–49.
- Tanis, M. C., Askim, O. J., Lancaster, S., Ward, G., Gainski, M., Nagassar, V., Shih, C., and Canales, L., 2006a, An integrated workflow for imaging below shallow gas: A Trinidad case study: 76th Ann. Internat. Mtg., Soc. Expl. Geophys., Expanded abstracts, 3051–3055.
- 2006b, Diving-wave refraction tomography and reflection tomography for velocity model building: 76th Ann. Internat. Mtg., Soc. Expl. Geophys., Expanded abstracts, 3340–3344.
- Tegtmeier, S., Gisolf, A., and Verschuur, D. J., 2004, 3D sparse-data kirchoff redatuming: *Geophys. Prosp.*, **52**, 509–521.
- Thomsen, L., Barkved, O., Haggard, B., Kommedal, J., and Rosland, B., 1997, Converted-wave imaging of Valhall reservoir: 59th Ann. Internat. Mtg., European Association of Geoscientists and Engineers, Expanded Abstracts, B048.
- Thorbecke, J. W., 1997, Common focus point technology: Ph.D. thesis, Delft University of Technology.
- Thorbecke, J. W., and Wapenaar, C. P. A., 2006, From reflection to transmission data: Ann. Internat. Mtg., Eur. Assoc. of Expl. Geophys., Expanded abstracts, A41.
- Traynin, P., Liu, J., and Reilly, J. M., 2008, Amplitude and bandwidth recovery beneath gas zones using Kirchhoff prestack depth Q-migration: 78th Ann. Internat. Mtg., Soc. Expl. Geophys., Expanded abstracts, 2412–2416.
- Van der Baan, M., Wookey, J., and Smit, D., 2007, Stratigraphic filtering and source penetration depth: *Geophysical Prospecting*, **55**, 679–684.
- van Groenestijn, G., and Verschuur, D., 2009a, Estimating primaries by sparse inversion and application to near-offset data reconstruction: *GEOPHYSICS*, **74**, A23.
- 2009b, Estimation of primaries and near-offset reconstruction by sparse inversion: Marine data applications: *GEOPHYSICS*, **74**, R119.
- Verschuur, D. J., Berkhout, A. J., and Wapenaar, C. P. A., 1992, Adaptive surface-related multiple elimination: *Geophysics*, **57**, no. 9, 1166–1177.
- Verschuur, D. J., and Berkhout, A. J., 1997, Estimation of multiple scattering by iterative inversion, part II: practical aspects and examples: *Geophysics*, **62**, no. 5, 1596–1611.

References

- Verschuur, D. J., and Marhfoul, B. E., 2005, Estimation of complex near surface focusing operators by global optimization: 67th Ann. Internat. Mtg., Eur. Assoc. of Geosc. and Eng., Expanded abstracts, A035.
- Verschuur, D. J., 2006, Seismic multiple removal techniques: Past, present and future: EAGE Publications BV.
- Virieux, J., and Operto, S., 2009, An overview of full waveform inversion in exploration geophysics: *Geophysics*, **74**, no. 6, WCC1–WCC26.
- Vogelaar, B., and Smeulders, D., 2007, Extension of White's layered model to the full frequency range: *Geophysical Prospecting*, **55**, 685–695.
- Wagner, D., Sen, V., Foster, P., Albertin, D., Read, R., and Burch, T., 2001, Imaging through shallow gas seeps: 3D pre-stack depth migration and velocity analysis: Ann. Internat. Mtg., Soc. Expl. Geophys., Expanded abstracts, 961–964.
- Wang, Y., 2004, Q analysis on reflection seismic data: *Geophysical Research Letters*, **31**, no. L17606, 1–4.
- Wapenaar, C. P. A., and Berkhout, A. J., 1989, Elastic wave field extrapolation: redatuming of single- and multi-component seismic data: Elsevier Science Publ. Co., Inc.
- Wapenaar, C. P. A., Thorbecke, J. W., and Draganov, D., 2004, Relations between reflection and transmission responses of three-dimensional inhomogeneous media: *Geoph. J. Int.*, **156**, 179–194.
- Wapenaar, C. P. A., Jul 1992, The infinite aperture paradox: *Journal of Seismic Exploration*, **1**, no. 1, 325–336.
- White, J. E., 1975, Computed seismic speeds and attenuation in rocks with partial gas saturation: *Geophysics*, **40**, no. 2, 224–232.
- Xie, Y., Xin, K., Sun, J., Notfors, C., Biswal, A. K., and Balasubramaniam, M. K., 2009, 3D prestack depth migration with compensation for frequency dependent absorption and dispersion: 79th Ann. Internat. Mtg., Soc. Expl. Geophys., Expanded abstracts, 2919–2923.
- Youn, O. K., Soponpongpipat, P., and Pinpipat, N., 2001, A modeling study of fault-shadow, shallow-gas, and low-velocity chimney effects on seismic data: Ann. Internat. Mtg., SEG Technical Program Expanded Abstracts, 1245–1248.
- Zhang, R., and Ulrych, T., 2002, Estimation of quality factors from CMP records: *Geophysics*, **67**, no. 5, 1542–1547.

Index

- P*-waves, 17, 18
- S*-waves, 5, 17, 18
- v_p/v_s ratio, 17, 18
- WRW** matrix notation, 33
- CFP* implementation, 115
- 4C* acquisition, 17
- 4C* multicomponent limitations, 18
- CFP*, 114
- CFP* image, 123
- 1.5D and 2D model description, 63
- 1.5D transmission deconvolution, 69
- 3D effective model, 102
- 3D full-waveform redatuming, 102
- 4C* acquisition, 17
- 4C* advantages, 17

- absorption, 5, 6, 13, 14, 16, 21, 103, 110, 126
- acoustic, 8, 16, 25, 87
- acoustic blanking, 8
- acoustic impedance, 9, 14
- acoustic turbidity, 8
- acoustic-impedance, 8, 43, 44
- adjoint operator, 45
- Amplitude Variations Offset (AVO), 10, 17
- anelastic, 18, 103
- anelastic attenuation, 6
- anelastic losses, 5, 6, 9, 12, 39, 103, 110, 111, 126
- anisotropic media, 116
- anisotropy, 6
- anticausal, 26, 27, 29–32
- attenuation, 12, 21, 64, 103, 123

- back-scattered wavefield, 8

- backward extrapolation, 26, 28, 30–32
- basalt layers, 9
- beam-steering ray tracing, 58
- biogenic, 8, 9
- blended acquisition, 54, 59
- blended shot record, 59, 60, 93
- blending operator, 59–61
- blockiness constraint, 53
- Born approximation, 105, 110
- boundary condition, 106

- Cartesian coordinate, 25
- cascaded deconvolution, 90
- Cauchy penalty function, 52
- causal, 26–28, 30–32
- causality, 26, 30, 31, 108
- chromosomes, 47
- coda, 7, 16, 19, 20, 36, 43, 47, 80, 100, 123
- Common Conversion Point (CCP), 17, 18
- Common Focus Point, 114
- Common Mid Point (CMP), 11
- complex conjugate, 26, 30, 32
- complex scattering, 16, 21
- complex wave propagation, 9, 10, 12, 37, 64, 110, 126
- complex-valued velocity, 6, 103, 110
- compressibility, 17, 105
- compressional waves, 17
- conjugate transpose, 99
- conventional redatuming, 66
- converted waves, 17
- crosscorrelation, 52, 54, 56, 99, 106
- crosscorrelation operator, 100
- crossover, 51
- crosstalk, 60

- data matrix, 59, 89
- deconvolution, 99
- deconvolution artifacts, 99
- deconvolution noise, 109
- deconvolution operator, 100
- deconvolution residuals, 73, 76
- density model, 64, 66, 80, 81, 92, 93
- Depth conversion, 14
- Differential Time Shift (DTS), 115
- dipole source, 66
- directivity effects, 33, 39, 90
- dispersion, 6, 9, 14, 81
- diving waves, 106
- dynamics, 9, 14, 42, 109

- effective medium, 22, 43, 47, 54, 74, 83, 110
- effective model, 41, 97
- eikonal solver, 30, 100, 106, 115
- elastic, 10, 13, 25, 103, 126
- energy-flux approach, 45
- energy-flux conservation, 45
- EPSI, 90
- equivalent medium, 41
- Estimated Primaries Sparse Inversion (EPSI), 90

- far-field energy, 30
- feasibility, 43, 63, 77
- Feasibility experiment - 1.5D example, 64
- Feasibility experiment - 2D example, 77
- Fermat's modeling, 119, 121
- Field data application, 87
- fine layering, 8, 10, 39, 103
- finely-layered media, 7, 8
- finite-difference, 10, 20, 48, 54, 59, 66, 77, 80, 81, 105, 106, 121
- fluid-replacement method, 18
- focusing operator, 113–116, 121–123, 125
- forward extrapolation, 26, 28, 31
- forward model, 31, 37
- Fourier transform, 33, 52, 131
- frequency marching, 47, 53, 54, 71
- frequency-marching strategy, 54
- full-wavefield operators, 100
- full-waveform redatuming, 22, 42, 63, 72, 73, 77, 84, 93, 96, 98, 100, 101, 107, 108
- full-waveform transmission operator, 21, 22, 32, 37, 39, 41, 43, 54, 66, 97, 102

- GA 1.5D objective function, 52
- GA 2D adaptive objective function, 55
- GA 2D objective function, 56
- GA definitions, 49
- Gabor transform, 13
- Gardner-Gardner-Gregory empirical relation, 92
- gas chimneys, 5, 8, 10, 12, 113
- gas clouds, 5, 8–10, 113
- gas migration, 9
- gas saturations, 9
- gas-cloud inversion strategy, 37
- Gassmann's fluid substitution, 18
- Gauss's Theorem, 25
- General Genetic Algorithm workflow, 55
- Genetic Algorithm, 47
- Genetic Algorithm 1.5D, 52
- Genetic Algorithm 2D, 54
- Genetic Algorithm advantage, 104
- Genetic Algorithm overview, 47
- Genetic Algorithm workflow, 49
- geochemical signatures, 9
- geological complex faulting, 9, 10
- geometrical spreading, 22, 29, 107, 114
- Green's function, 12, 14, 22, 26, 27, 29–32, 100, 106, 114, 115
- Green's Theorem, 25

- Hermitian, 42, 45, 99–101
- heterogeneous medium, 9, 25, 30–32, 47, 63, 99, 100, 106, 114, 116
- heuristic approach, 104
- hydrocarbon fields, 9
- hyperbolic, 116, 121, 123

-
- imaging condition, 106
 - inhomogeneous medium, 29, 30, 63, 64, 100
 - initial 2D GA parameters distribution, 56
 - initial GA distribution, 50, 55
 - initial model, 48
 - internal multiples, 20, 22, 40, 63, 73, 89, 90
 - internal scattering, 103
 - intrinsic attenuation, 6
 - invariant embedding method, 129
 - invariant medium, 64
 - inverse propagation operator, 99
 - inverse Q-factor, 13
 - inverse Q-filtering, 14
 - inverse-Q, 13
 - isotropic media, 129

 - Kennett's method, 64, 129
 - kinematics, 9, 10, 12, 14, 16, 20, 42, 80, 109, 113
 - Kirchhoff integral, 22, 25, 27, 29
 - Kirchhoff migration, 106
 - Kirchhoff PreSDM, 16, 106

 - land near-surface, 102, 110, 116
 - layer stripping, 22
 - layer-stripping redatuming, 101
 - layered media, 129
 - least squares inversion, 43
 - linear imaging, 19
 - long offset, 12
 - loss free, 87
 - low-velocity anomaly, 20

 - mating, 50
 - matrix inversion, 41, 77, 89
 - matrix notation, 33, 36, 45
 - migration operator, 114
 - migration velocity analysis, 41
 - missing near offsets, 89
 - mode conversion, 9
 - multicomponent seismics, 17
 - multipathing, 103, 106, 126
 - multiple scattering, 7–9, 19, 20, 32, 36, 64, 89, 106, 110
 - mutation, 51

 - near-surface problem, 102
 - near-surface velocity, 16
 - non-symmetric, 113
 - nonhyperbolic, 5, 9, 14, 92, 113, 116, 118, 124–126
 - nonlinear inversion, 22, 41, 47, 66, 80, 92, 104, 109
 - Numerical data examples, 63
 - numerical modeling, 64

 - objective function, 50, 57, 60
 - Ocean Bottom Cable (OBC), 17, 105
 - one-way focusing operators, 41, 116
 - one-way travel time, 114–116, 118, 119
 - Other 2D GA enhancements, 61

 - P-P data, 17
 - P-S data, 17
 - parameters, 48, 49, 55, 61
 - physical causality, 7
 - physical geological interpretations, 8
 - plane-wave domain, 43
 - populations, 48, 49, 52, 61
 - poroelastic media, 9
 - PreSDM, 9, 10, 12, 16, 19, 20
 - PreSTM, 9, 12
 - propagation operator, 106
 - propagators, 106
 - pull-up effect, 14, 15
 - push-down effect, 8, 14, 15

 - Q-attenuation, 8, 13
 - Q-compensation, 12, 13
 - Q-estimation, 12
 - Q-factor, 13
 - Q-migration, 12, 14
 - Q-model, 12, 14

 - Radon demultiple, 123
-

Index

- Radon interpolation, 89
- ray parameter, 43, 130
- ray tracing, 30, 100, 106, 115
- ray-parameter domain, 52, 64
- ray-parameter-frequency, 129
- ray-tracing, 14
- Rayleigh integral, 22, 25, 27, 28, 30, 32, 114
- realizations, 48, 49, 52, 61
- reciprocity theorem, 33, 89, 90, 114
- recursive, 92, 129
- redatuming, 87, 110, 116
- reflectivity model, 100
- Reverse Time Migration (RTM), 102, 106
- rock matrix, 17

- sagging, 9, 14, 15
- scale factor, 55, 56, 69
- scattering attenuation, 7
- scattering integral, 105
- scattering theory, 105
- seepages/gas bubbles, 9
- shallow diffractions, 10
- shear-waves, 17
- short-offset, 16
- Snell's law, 43
- source signal, 64
- source signature, 66
- source wavelet, 8, 39, 40, 59, 64, 65, 92, 131
- spatial convolution, 34, 38
- spline, 118
- spline interpolation, 116, 118
- squirt flow, 6, 103
- statistical analysis, 63, 74, 75, 104
- stratigraphic filtering, 7, 43
- Surface-Related Multiple Elimination (SRME),
90, 123
- systematic errors, 14

- tertiary basin, 92
- thermogenic, 8, 9
- time delays, 9, 14, 59
- time shift, 52, 56

- Toeplitz, 43
- tomography, 10, 12, 16, 121
- transmission, 37
- transmission compensation, 106, 107
- transmission effects, 10, 17, 19, 22, 31, 39,
73
- transmission imprint, 98, 110
- transmission operator estimation, 41
- transmission operators, 22, 37, 41, 42, 45,
74, 77
- true-amplitude migration, 9
- true-amplitude redatuming, 41, 100, 103
- turning waves, 106
- two-way travel time, 115, 119

- velocity model, 5, 9, 10, 14, 16, 19, 20, 22,
64, 80, 81, 92, 93, 115
- visco-acoustic, 103
- visco-elastic, 19, 110, 113

- walk-away VSP, 115
- wave-equation migration, 20, 48, 106, 108
- wavefield extrapolation, 25, 27
- wavefield replacement operators, 108
- weight function, 58

- zero lag, 106

Summary

A gas cloud is a region of gas accumulation in the subsurface, which can severely deteriorate the seismic data quality from deeper reflectors. Due to complex wave propagation through the anomaly and the resulting transmission imprint on the reflections from below this area, the image below the gas cloud is usually not properly recovered. The reflected events in this region appear with lower amplitude and lower frequency content, which is often refers to as Q-attenuation, Q-absorption, or anelastic or intrinsic loss.

This thesis describes a new approach to imaging below such anomalies for seismic exploration purposes. The new full-waveform inversion-based approach can contribute to this largely unsolved problem. The approach differs from traditional solutions, which aim at effective amplitude and phase corrections of the seismic reflections (removing the absorption effect), whereas the new developed approach treats the problem as a complex-scattering phenomenon.

The basic principle of the proposed method is that the reflection response of the complex gas-cloud area, including its coda, carries detailed information on the gas-cloud properties, which can be translated into transmission-correction operators. We aim at constructing full-waveform transmission operators (including the codas) from the gas-cloud reflection response via an effective-medium representation, obtained through nonlinear full-waveform inversion. In our case we have used a Genetic Algorithm for this purpose. From the property model of the gas cloud, the transmission operators are determined by forward modeling. It has been shown that true-amplitude imaging of reflections below the gas cloud is achieved via multidimensional deconvolution of the seismic data for these full waveform transmission operators.

For a 2D synthetic dataset, a suitable property model of the gas cloud region is obtained. Redatuming the seismic data using the full-waveform transmission operators from this effective medium model show that primary reflections underneath the gas cloud are very well recovered and the transmission codas are reduced.

The method was also applied to a 2D real marine dataset, where we aim at inverting for the heterogeneous overburden above the gas-cloud region. The results after the true-amplitude redatuming show that the amplitudes of the target horizons are better recovered. These results are very promising, considering the fact that there are many effects that could limit the quality of the final result, such as the 3D geometry effects of the gas-cloud body itself, mode conversions that are neglected, limitation in the source estimation and restrictions

in the acoustic forward-modeling algorithm. The stack after the full-waveform redatuming displays better and more continuous reflections.

The results of this research has confirmed our belief that, what is often referred to as absorption, probably to a large extent is caused by complex wave-propagation effects. Although some energy really may disappear into heat (anelastic loss), we believe that a large part of the energy is scattered in elastic mechanisms (internal scattering, multipathing etc.) and, therefore, is recoverable by full-waveform deconvolution.

Samenvatting

Een gas cloud (gaswolk) is een regio van gasophoping in de ondergrond die in ernstige mate de kwaliteit van seismische data negatief kan beïnvloeden. Vanwege de complexe golfvoortplanting door de anomalie en de daaruit voortvloeiende transmissieeffecten op de reflecties van onder dit gebied, kan een goede afbeelding van het gebied onder de gaswolk meestal niet goed worden verkregen. De reflecties van dit gebied worden met een lagere amplitude en frequentieinhoud waargenomen, hetgeen vaak wordt beschreven als Q-verzwakking, Q-absorptie, of anelastische of intrinsieke demping.

Dit proefschrift beschrijft een nieuwe aanpak voor seismische afbeelding van het gebied onder zulke complexe gebieden. De nieuwe, op volledige golfvorminversie gebaseerde aanpak zal bijdragen tot dit grotendeels onopgeloste probleem. Terwijl traditionele oplossingen zich richten op effectieve amplitude- en fasecorrecties van de seismische reflecties (het verwijderen van het absorptie effect), wordt in de nieuw ontwikkelde aanpak het probleem beschreven als een complex verstrooiingsverschijnsel.

Het basisprincipe van de methode is dat de reflectieresponsie van het complexe gaswolk gebied, met inbegrip van de coda, gedetailleerde informatie bevat over de mediuimeigenschappen in de gaswolk, die kunnen worden vertaald in transmissie-correctie operatoren. Het doel van de methode is volledige golfvorm transmissieoperatoren (inclusief de codas) te bepalen via een effectieve mediumrepresentatie, verkregen door volledige golfvorminversie van de gaswolk reflectieresponsie. In dit geval hebben we een genetisch algoritme gebruikt om een effectief model van de gaswolk te krijgen en met behulp van voorwaartse modellering kunnen de hieruit transmissieoperatoren berekend worden. Er is aangetoond dat een waarheidsgetrouwe afbeelding van de reflecties van het gebied onder de gaswolk bereikt kan worden via multi-dimensionale deconvolutie voor deze volledige golfvorm transmissieoperatoren.

Voor een 2D synthetische dataset in een model met een realistische gaswolk kon een goed inversieresultaat verkregen worden. Het vervolgens redatumen van de seismische data met behulp van de volledige golfvorm-transmissieoperatoren, verkregen uit dit effectieve mediummodel, toonde aan dat de primaire reflecties onder de gaswolk zeer goed hersteld werden en dat de transmissiecoda werd gereduceerd.

De methode is ook toegepast op een echte 2D marine dataset, waarbij we ons gericht hebben op het inverteren van de heterogene deklaag boven een gaswolk, omdat dit beter voldeed aan het 2D karakter dat vereist is in het huidige algoritme. Uit de resultaten na de reda-

tuning blijkt dat de amplitudes van de reflecties onder gaswolk goed zijn gereconstrueerd. Hoewel in dit proces met de gaswolk zelf nog geen rekening is gehouden, zijn deze resultaten veelbelovend, gezien het feit dat er veel beperkingen in de huidige aanpak zitten, zoals het feit dat de gaswolk een 3D geometrie heeft, dat er golfconversies kunnen optreden, dat het schatten van het bronsignaal niet perfect was en dat de voorwaartse modellering slechts akoestisch is. Desondanks geeft de stack na de volledige golfvorm redatuming betere en meer continue reflecties.

De resultaten van dit onderzoek heeft onze overtuiging bevestigd dat wat vaak absorptie wordt genoemd waarschijnlijk voor een groot deel een complex golfvoortplantingsfenomeen is. Hoewel energie gedeeltelijk in warmte kan worden omgezet (anelastisch verlies) zijn wij van mening dat een groot deel van de energie wordt verspreid in elastische mechanismen (interne verstrooiing, meervoudige looppaden enz.) en daarom kan worden gereconstrueerd via volledige golfvormdeconvolutie.

Acknowledgments

Alhamdulillah – All praise is to Allah;
The Lord Of The Creation. The Compassionate, the Merciful.

First of all, I would like expressed my gratitude to Petroliam Nasional Berhad (PETRONAS), PETRONAS Petroleum Management Unit and PETRONAS Research, Malaysia, for providing the seismic data and for giving me the permission to publish this work. Also, I would like to thank the sponsors of the DELPHI consortium for their support.

I would like to convey my sincere appreciation again to PETRONAS for giving me the scholarship as well as to the Delphi consortium for providing me the opportunity to come to Delft, doing my PhD and started this amazing adventure; both letting me to work in the most reputable and prestigious geophysics group in the world. I hope the collaboration with PETRONAS will be further strengthened and will be fruitful to both parties in the future and beyond.

I also would like to extend my gratitude to Dr. Mahboub Al-Chalabi, Dr. Deva P. Ghosh, Dr. Juergen Pruessmann, Dimyati Mohamed, M. Khalid Embong, M. Hafizal Mad Zahir, M. Faizal Abdul Rahim and my father, Ghazali Muhammad Nur, whom persuaded, encouraged and convinced me to continue my further study at Delft University of Technology, The Netherlands.

I am deeply indebted and grateful to Dr. Hamzah Abdul Hamid, M. Hasni M. Hashim, M. Yazid Mansor, M. Azhar Yusof, M. Kamal Embong, Dr. Mazlan Madon, Ms. Halipah Mat Ali and M. Yazid M. Saad from the management of PETRONAS and PETRONAS Research for their seamless and continuous support.

I am indebted and would like to express my eternally appreciation for the truthful dedications and untiring commitments of my wife and love: Cik Junidza Mat Nayan together with my beautiful and wonderful family: Ahmad Irfan, Aqilah Sofiyah, Aliyahnur Sarah, Asmaa Amelia and Amaanee Husna, for everything. Heartiest appreciation to my loving and caring parents and parents-in-law as well as my families for their support: Ayahanda Ghazali Muhammad Nur and Nur Azian Mahmood, in-memory Zakiah Hj Rajihan, Ayahanda Mat Nayan Abdullah and Ramlah Saad.

I remembered the first time when my family and I moved to Delft, I was not only facing the geophysical challenges in highly-advanced physics and math, such dealing with complex

wave propagation theory, but the reality of starting back my life as a student and being a full researcher at a 170 years-old cum amongst the best technology universities in the world is a huge challenge. But these challenges make me more persevere and enjoy life to bits. Embarking this fantastic journey. A great journey ahead.

I am grateful to being able to work with and have as my PhD promotor and my mentor Prof.dr.ir. Dries Gisolf. I valued the great in-depth discussions, suggestions, critical mindset and ideas you have especially on the technicality of this research. Once, there is only a sketch of philosophical ideas and then became a concept, later being implemented, tested and finally applied to the real data. Albeit the seriousness of the research discussions, you always have been a nice person, taking care of the Delphi team and always treat us in a very good restaurant during conferences.

My wholehearted appreciation, gratefulness and humble respect go to my supervisor, Dr.ir. Eric Verschuur for being a great teacher, guru and a great mentor. William A Wardi used to say, "The mediocre teacher tells. The good teacher explains. The superior teacher demonstrates. The great teacher inspires." To me, you inspired. You are the living wikipedia for seismic. It is an honour for me to be accepted as your apprentice. You made the toughest geophysics sounds simple, suggesting always workable solutions; of which sometimes I really doubt that it will work ... Apparently, it works! Thank you for always being optimistic, having trust and accepting me. I will safeguard the technical logs that we made during our long-hours discussions and of course the notes on many new ideas. Thank you.

Special dedication to my close-friends, officemates and fellow research comrades: Gert-Jan van Groenestijn, Muhammad Al-Bannagi, Hannes Kutscha, Khalid Chougrani; and my Delphi colleagues: Peter, Araz, Panos, Marwan, Xander Staal, Dana, Justyna, Maurice, Ayon, Alex, Bouchaib and Rolf for all the heavy scientific and less-scientific related discussions, especially on life, opposite gender, faith, international trips and those happy moments. Thank you and may our friendship last forever.

Special thanks to Rolf Baardman and Gert-Jan van Groenestijn for helping me on *SRME* and *EPSI* implementations; Muhammad Al-Bannagi and Dr. Jan Thorbecke for debugging and parallel-computing codes optimizations; Margaret van Fessem, Edo Bergsma and Henry den Bok for their help and efficiency on the office-related matters.

This thesis could not make it to the publisher without the meticulous editing, suggestions and critics from the direct and indirect external reviewers (of course other than my supervisor and promotor): Prof.dr.ir. A.J. Berkhout, Prof.dr. Helmut Jakubowicz, Dr.ir. Walter Rietveld, Prof.dr.ir. Kees Wapenaar, Dr. Deva Ghosh, Dr. Mehmet Ferruh, Nik Shahman Nik Ahmad Ariff, Cempaka Seri Abdul Malek, Mas Elizawati Mohammad-Ali and my wife.

To Hafizuddin Ibn Jarir and Fadrisam Asmar, I always treasured your accompany in the United States, until we meet again insyAllah. Kepada rakan-rakan Melayu yang lain, "Kekuatan tidak datang dari kemampuan fizikal tetapi ianya datang dari semangat yg tidak pernah mengalah..." Teruskan perjuangan. May our friendship be blessed forever.

Prof. A.J. Berkhout always reminds me with his words that I would like to pass on to others,

“Simple! Simple! Simple! The details are important but remember that people will not grab the details but only the essence. If you understand the physics, you will remember it forever in your life.” Many fools can make things complicated but it takes a genius to make things simple.

“Thesis ini didedikasikan pada arwah ibunda yang tersayang, Zakiah Hj Rajihan, walaupun anakanda tidak dapat menjadi doktor pakar perubatan, tapi harapannya insyAllah anakanda akan menjadi antara doktor pakar geofizik yang terbaik di dunia.”

On a final note: God creates, we mankind, only discover (Ghazali Muhammad Nur, 1998).

Thank you.

Ahmad Riza Ghazali

Arthur van Schendelplein 77, Delft;

13th December 2010 (7 Muharram 1432).

List of papers presented and published

1. Ghazali, A. R., Verschuur, D. J., Gisolf, A., 2010, Multi-dimensional non-linear full waveform inversion of gas cloud reflection data using a Genetic Algorithm and a blended acquisition approach, Society of Exploration Geophysicists (SEG) Intl Exposition and 80th Annual Meeting, Denver, Expanded Abstracts.
2. Ghazali, A. R., Verschuur, D. J., Gisolf, A., 2010, Imaging below gas clouds through nonlinear full waveform inversion of the reflection response The 2D case: 72nd European Association of Geoscientists and Engineers Annual Conference & Exhibition, Barcelona, Expanded abstracts.
3. Ghazali, A. R., Verschuur, D. J., Gisolf, A., 2010, Imaging below gas clouds through non-linear inversion of reflection data: A 1.5D feasibility study, Geophysical Journal International (submitted).
4. Ghazali, A. R., Verschuur, D. J., 2010, True amplitude seismic imaging beneath gas cloud using full waveform transmission deconvolution; Petroleum Geoscience Conference and Exhibition 2010, 29th-30th March, 2010 Kuala Lumpur Convention Center, Kuala Lumpur, Malaysia.
5. Ghazali A.R., Verschuur D.J., Gisolf A., 2010, Non-linear full waveform inversion of reflection data: The 2D case, Delphi C and M, Vol. VIII, Ch 8, 125-143, ISBN: 978-90-73817-46-3.
6. Ghazali A.R., Verschuur D.J., Gisolf A., 2010, Non-linear inversion of reflection data: a 1.5D feasibility study, Delphi C and M, Vol. VIII, Ch 7, 101-122, ISBN: 978-90-73817-46-3.
7. Ghazali, A. R., Verschuur, D. J., 2009, Data driven imaging via automated non-hyperbolic focusing operator estimation for heterogeneous media, PETRONAS Technology Journal, 2.
8. Ghazali, A. R., Verschuur, D. J., Gisolf, A., 2009, True amplitude seismic imaging beneath gas cloud using full waveform transmission deconvolution, PETRONAS Technology Journal, 2.

9. Ghazali, A. R., Verschuur, D. J., Gisolf, A., 2009, 2D full waveform transmission deconvolution for true amplitude imaging below gas-clouds, Society of Exploration Geophysicists (SEG) Intl Exposition and 79th Annual Meeting, Houston, Expanded Abstracts.
10. Ghazali, A. R., Verschuur, D. J., Gisolf, A., 2009, Imaging below gas clouds through true amplitude redatuming: Barcelona, EAGE/SEG Research Workshop - Frequency Attenuation and Resolution of Seismic Data, Expanded abstracts, B08.
11. Ghazali, A. R., Verschuur, D. J., Gisolf, A., 2009, Non-linear inversion for true amplitude imaging below gas clouds A 1.5D feasibility study: 71st EAGE Conference and Exhibition, Amsterdam, Expanded abstracts.
12. Ghazali A.R., Verschuur D.J., Gisolf A., 2008, Seismic imaging through gas clouds: A data-driven imaging strategy, Society of Exploration Geophysicists (SEG) Intl Exposition and 78th Annual Meeting, Las Vegas, Expanded Abstracts, 27, 2302-2306.
13. Ghazali A.R., Verschuur D.J., Gisolf A., 2008, True amplitude imaging below gas clouds through non-linear inversion of reflection data, Delphi C and M, Vol. VII, Ch 7, 69-88, ISBN: 978-90-73817-43-2
14. Ghazali A.R., Verschuur D.J., Gisolf A., 2008, Non-linear inversion for true amplitude imaging below gas clouds: a 1.5D feasibility study, Delphi C and M, Vol. VII, Ch 8, 89-110., ISBN: 978-90-73817-43-2
15. Ghazali A.R., Verschuur D.J., Gisolf A., 2008, Recursive seismic modeling in the ray parameter-frequency domain, Delphi C and M, Vol. VII, Ch 8A, 110-114., ISBN: 978-90-73817-43-2
16. Ghazali A.R., Verschuur D.J., Gisolf A., 2008, Seismic imaging through gas clouds: A data-driven imaging strategy, Society of Exploration Geophysicists (SEG) Applied Research Workshop Kuala Lumpur, Geophysical Challenges in Southeast Asia Exploration, Expanded Abstracts.
17. Halim M. F. A., Yusoff W. I. W., Sengupta M.K., Arshad S., Ghazali A.R., 2008, 3D AVO Volume Visualization in Identifying HC Leads in Offshore Sarawak, Society of Exploration Geophysicists (SEG) Applied Research Workshop Kuala Lumpur, Expanded Abstracts.
18. Ghazali, A. R., Verschuur, D. J., Gisolf, A., 2007, Seismic imaging through gas clouds An evaluation, PETRONAS Technology Journal, 1, 18-35.
19. Ghazali A.R., Verschuur D.J., 2007, Estimation of focusing operators for heterogeneous media by global optimization, Delphi M and I, Vol. XIX, Ch 9, 243-258, ISBN: 978-90-73817-39-5

20. Ghazali A.R., Verschuur D.J., Gisolf A., 2007, Seismic imaging through gas clouds An evaluation, Delphi M and I, Vol. XIX, Ch 10, 217-242., ISBN: 978-90-73817-39-5

Curriculum vitae

Ahmad Riza Ghazali was born and raised in Penang, Malaysia. He was educated at the University of Leicester, United Kingdom, where he graduated with honours in Geophysics. He is a staff geophysicist in the seismic imaging group at PETRONAS Research, a research division of PETRONAS, Malaysia's multi-national oil and gas company. He joined the DELPHI Consortium in December 2006 to pursue a PhD in seismic imaging at Delft University of Technology, The Netherlands. Together with Prof.dr.ir. A. Gisolf and Dr.ir. D.J. (Eric) Verschuur, he concentrates on true-amplitude imaging below gas clouds. His research interests are true-amplitude imaging, complex wave-propagation, full-waveform inversion and reservoir characterization. To date, he has been involved and leads many operational and research projects in specialized seismic processing/imaging and seismic quantitative interpretation around the world. He is also an active member of Society of Exploration Geophysicists (US), co-representative of SEG Global Affairs Committee for Malaysia, member of European Association of Geoscientists and Engineers (EU) and Malaysian Society of Exploration Geophysicists.